An implementation of soil particle transportation concept for internal erosion simulation and its application to vertical shaft construction

2021

Tangjarusritaratorn Tanawat

Acknowledgements

Firstly, I would like to express my sincere gratitude to Professor Kiyoshi Kishida and Professor Makoto Kimura for giving me a good chance of being student in here. This research has been studying through master courses of the Human Security program in the department of civil and earth resources in Geomechanics laboratory at Kyoto University. Since, I became a student in Kishida lab, many people surrounding me always give a good support for both research work and personal life.

Professor Kiyoshi Kishida is my supervisor, he gave me a huge support since I was master student. He has contributed so much facility and his knowledge and experience to my research work. He also provided a flexible schedule for seminars, therefore, we can spend time for study on a new thing. Since, I decided to start on this research work, he always encourages me and try to work with a new idea for research novelty. Also, he is very open-minded professor. Since, when I was thinking about starting this research, I had very less knowledge about this research topic but he still accepted my decision.

Professor Makoto Kimura is also my previous advisor during master course which constantly gave a suggestion on my research since master course. Needless to say, I have been educated by him since then which is very valuable for my further study in doctor course.

I would like to appreciate Associate Professor Yasuo Sawamura. He has been giving a specific suggestion for my numerical analysis as well. Moreover, he has kindly taught me about knowledge and shared his experience.

I would like to appreciate Assistant Professor Yusuke Miyazaki, who is assistance professor in Kishida lab. He normally gives me an idea and a lot of suggestions on research. Moreover, research fund for this study was contributed by him as well. He also is the person who educated me since I was master student. Most of experience and knowledge I had obtained from him. One of his visibility that he always encourages student to think about is the research novelty, therefore, it was a foundation of my research work.

I also need to appreciate Associate Professor Kikumoto Mamoru from Yokohama university. He recently joins my research meeting with Professor Kiyoshi Kishida and

Assistant Professor Yusuke Miyazaki. Mainly, he provided a suggestion for examination in the validity of erosion model.

In addition, I would like to appreciate Associate Professor Shinichiro Onda who had examined on this research and gave a further suggestion for improvement.

I would like to appreciate Yuko Matsuoka, she in charge of my every important document. In addition, she always helps me in the personal document as well.

I am very thankful to Takanori Shibata, who is my senior student. He has been helping and teaching me in both of academic field and personal issue since master course.

Lastly, I would like to appreciate family and friends in Kishida lab. They have been giving me a moral support.

August 2021

Tanawat Tangjarusritaratorn

Abstract

This research aims to get more understanding about vertical shaft structure which is mainly needed in tunnelling construction project. The mechanical behavior of soil in both surrounding area and at excavation area could be well simulated by using commercial software (FLAC3D). The soil-water coupling analysis shows that the maximum inner displacement is always located at 5-10 m above excavation surface while the earth pressure acting on shaft wall is much lower than active earth pressure in corresponding with Rankine theory. According to the simulation of vertical shaft in high groundwater level, the fluid flow at the bottom of shaft is basically high due to the difference pressure head from dewatering process which might cause a suffusion or internal erosion. Subsequently, this research pay attention to the development of erosion scheme for an examination of vertical shaft undergoing with high seepage flow. The erosion model was established based on the concept of particle transported and governed by convection equation together with momentum balance equation. In addition, the consideration of several component of force acting on particle has been done and seem to be drag force is dominating in this simulation. The comparison of cumulative fine loss between previous experiment data from Ke & Takahashi (2014) and numerical simulation of soil column test and shows that the tendency of result in both experiment and calculation are similar, however, at the beginning, the fine loss from the simulation is slightly higher than the experiment. Finally, by simulation of the soil surrounding vertical shaft was conducted in two-dimensional model, the result is obviously showing that the erosion starts to occur at the bottom of shaft wall. Similarly, the small scales simulation in accordance with the experimental model of seepage flow beneath sheet pile wall shows the highly eroded at the bottom of sheet pile wall.

Table of contents

Abstract III
Chapter 1 Introduction 1
1.1 Background 1
Chapter 2 Literature review 11
2.1 The underground construction undergoing with erosion 11
2.1.1 Dewatering of shaft 11
2.2 Erosion mechanism 13
2.2.1 The erosion failure in earth structure 15
2.2.2 The internal erosion in earth structure 15
2.2.3 The experiment of internal erosion (Soil sample test) 17
2.3 Particle flow in porous media 20
2.4 Soil model (Composition of soils) for an erosion model 21
2.5 Erosion simulation model 23
2.5.1 Erosion rate and initiation of erosion 24
2.5.2 The erosion transportation 25
2.6 Lifting force 27
2.7 Buoyancy force 30
2.8 Aerodynamic drag force 31
2.8.1 Drag force coefficient (Singular particle flow) 33
2.8.2 Secondary coefficient on drags force (multi-particle flow) 39
2.9 Tortuosity 40
Chapter 3 The soil-water coupling analysis of vertical shaft in shallow groundwater area 41
3.1 Introduction 41
3.2 Background 41
3.3 Numerical method 42
3.3.1 The numerical formation in FLAC3D and constitutive model 42
3.4 The simulation procedure 52
3.4.1 Mesh generation and boundary condition 52
3.4.2 Excavation with dewatering simulation 52
3.5 The fundamental behavior of circular vertical shaft in high groundwater level (soft and rigid shaft) 53
3.5.1 Results of fundamental behavior of excavation process in high groundwater level 55

3.5.2 Discussion of fundamental behavior of excavation process in high groundwater level 56
3.6 Excavation stability in circular vertical shaft during excavation process in high groundwater level 59
3.6.1 Results of excavation stability 60
3.6.2 Discussion of excavation stability 65
3.7 The pore pressure and fluid flow during the shaft construction 65
3.7.1 Result of pore pressure and fluid flow 66
3.7.2 Results of fluid flow velocity at each specific location 67
3.7.3 Discussion of pore pressure and fluid flow 68
3.8 Conclusion 69
Chapter 4 Numerical simulation scheme for an erosion 71
4.1 Introduction 71
4.2 Internal erosion (Suffusion) mechanism 71
4.3 Numerical method 72
4.3.1 Advection equation 72
4.3.2 Finite Difference method 74
4.4 Background of erosion simulation 77
4.5 Calculation scheme 80
4.6 Numerical simulation 85
4.6.1. The simulation with three components of force 89
4.6.2. The simulation with a theory of buoyancy-gravitational force ratio 92
4.6.3. The simulation of erosion induced by drag force 99
4.6.4. The simulation of erosion with difference tortuosity concept 102
4.7 Conclusion 110
Chapter 5 Particle-fluid flow coupling simulation for an erosion for one-directional flow 113
5.1 Introduction 113
5.2 The simulation of fluid flow 113
4.3 The staggered grid formation 115
5.4 Permeability calculation 116
5.5 Calculation scheme 118
5.6 Finite Different method for fluid flow 121
5.7 Numerical simulation 122
5.7.1 The coupling simulation of particle-fluid flow with difference pressure head 122

5.8 Conclusion 125
Chapter 6 Particle-fluid flow coupling simulation for an erosion for two-dimensional flow in gravitational field 127
6.1 Introduction 127
6.2 The simulation procedure 127
6.2.1 The modification of simulation scheme for two-directional flow in gravitational field 127
6.2.1 The fluid flow in gravitational field 127
6.2.2 The erosion scheme for two-directional flow 128
6.3 Numerical simulation 129
6.3.1 The simulation of erosion in two-dimensional analysis 130
6.3.2 The simulation of experimental model 142
6.3.3 The simulation of experimental model considering the dewatering characteristic 146
6.4 Conclusion 153
Chapter 7 Conclusions and future studies 155
Reference 159

Chapter 1 Introduction

1.1 Background

Erosion is the behavior whereby there is a reduction in the soil particles in a soil mass mainly induced by the motion of fluid. The erosion mechanism can be divided into three main groups, 1. Internal erosion or suffusion, 2. Contact erosion, and 3. Concentration leak erosion. This research aims to clarify the mechanism of suffusion type which is the most famous among the several erosion mechanisms and generally occurs in gap-graded soil. The suffusion is the mechanism that the fine particles of soil move through the porous media while the larger particles stay still as soil skeleton as shown in **Figure 1.1**. Furthermore, the observation reported by previous research confirmed that the piping and suffusion play major roles in the failure of earth dams **(Richards & Reddy; 2007)**. The seepage flow basically generates an excessive force on the fine particles in porous media which eventually causes internal erosion or suffusion. Therefore, many researchers have focused on elucidating suffusion behavior with numerical and experimental methods. In addition, Telkar and Pote (2018) concluded that the erosion mechanism comprises three main processes: 1. Detachment, 2. Movement, and 3. Deposition **(Telkar & Pote; 2018)**.

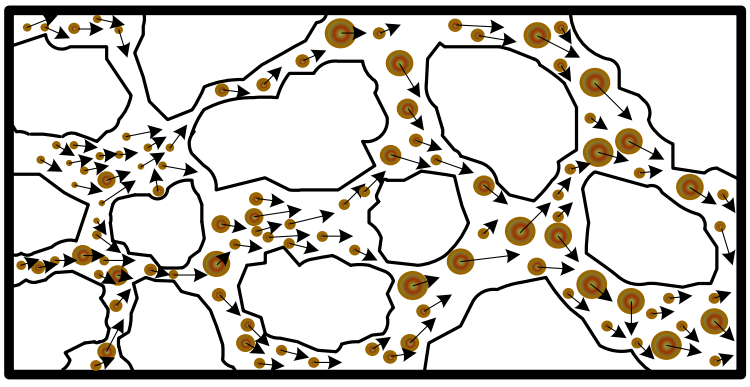

Figure 1.1. Suffusion mechanism

However, the erosion modelling for suffusion mechanism suggested by most of the previous research could be applied on specific soil, since, the erosion rate is obtained from the experiment which is a function of hydraulic shear stress as shown in **Equation 1.1 (Arulanandan K., Krone R.B. & Loganathan P.; 1975, Chaney R., Demars K.,**

Reddi L., Lee I-M. & Bonala M.; 2000). Therefore, the different material would be governed by a difference value of coefficient and required an experiment.

$$\dot{\varepsilon} = \alpha(\tau_a - \tau_c) \tag{1.1}$$

Where, $\dot{\varepsilon}$ is erosion rate, α is a coefficient of soil erosion (constant value), τ_a is a hydraulic shear stress, and τ_c is critical hydraulic shear stress.

According to the previous erosion model, the numerical modelling is basically relied on the experiment, hence, the aim of this research is trying to suggest a general model for internal erosion. The initiation of the new concept came from the group of particle flow in fluid substance in which Newton's second law is applied to generate an acceleration of the particle. Therefore, three main forces might be associating with the particle flow in porous media which are centrifugal force, buoyant force, and drag force as shown in **Figure 1.2**. Furthermore, while, the of particle flow in granular media is considered, lifting force is also exerting on each particle. According to the concept, the particle flow is governed by the force acting on them, hence, the several force combinations has been tried to apply in the simulation. This research tried to consider an effect from grain size distribution on the erosion behavior in accordance with the presumption that the difference particle sizes would be flowing with different velocity.

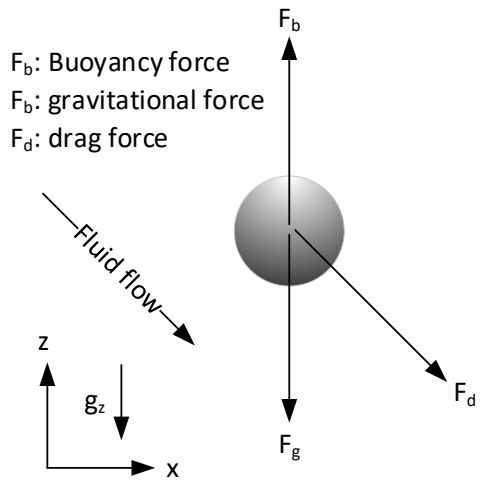

Figure 1.2. The force diagram of force acting on erodible particle

The simulation developed by this research is calculated under two-dimensional Finite Difference method (FDM). The particle flow inside porous media is governed by

advection equation as shown in **Equation 1.2** which normally could show a substance transported with the bulk motion in the term of density of each particle, φ_i. The advection equation is basically requiring particle flow velocity, $\mathbf{u_e^i}$, and source term, S_φ, to complete the calculation. Furthermore, the difference grain size of soil particles is individually discretized or it is considered as multi-phase flow as shown in **Figure 1.3**. Therefore, the simulation based on this method could cover some of the drawbacks from previous research work which are particle transportation and require less specific experimental work. According to the advantageous of considering particle transport, this numerical framework is likely to show more realistic behavior while it is applied to the simulation of erosion nearby underground structure such levee, retaining wall, or vertical shaft structure.

$$\dot{\varphi}_i + \mathbf{u_e^i} \cdot \boldsymbol{\nabla}\varphi_i = S_\varphi \tag{1.2}$$

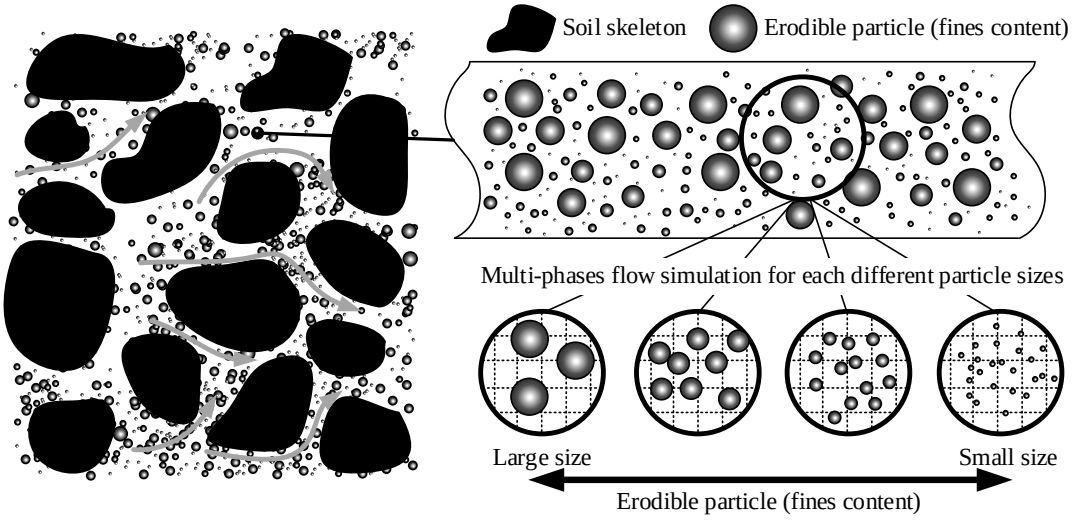

Figure 1.3. The consideration of flowing particle as multi-phases flow

In addition, the structure in which this research aims for applying erosion calculation scheme to show an erosion characteristic due to seepage flow is a vertical shaft structure. Recently, the expansion of metropolis become increasing which basically requires more infrastructure for transportation. Nevertheless, the density of structure on the ground surface is normally high, therefore, road or railway are likely to move into the ground which could save more space. Furthermore, almost every tunnelling construction

requires a shaft structure to be an entrance even or ventilation structure as shown in **Figure 1.4**.

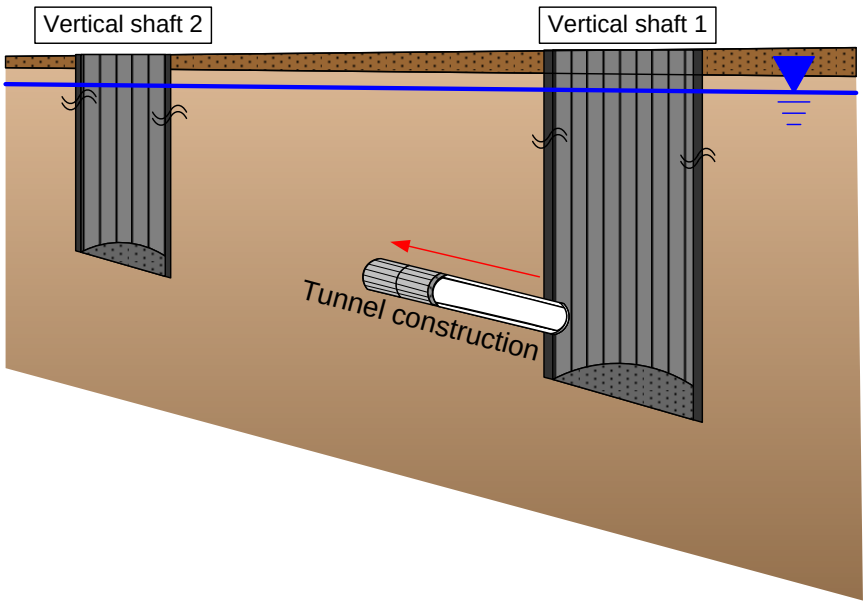

Figure 1.4. The vertical shaft structure in tunnelling construction

According to the urban area, there are a plenty of underground structure already exist, therefore, the new underground structure is mostly forced to be located at the deeper position in accordance with their surrounding. In general, the deep underground structure faces with high earth pressure as well as the deep shaft structure. Nevertheless, geometry of structure is much considered, especially in tremendous structure, since the difference geometry could be leading to undergoes with different earth pressure distribution. Recently, the cylindrical structure or the structure which has the circular cross-section is widely utilized in accordance with the superbness of their characteristic. Most of the shaft structure design also took the benefit from cylindrical structure, if there is no limitation of surrounding space. In addition, the previous research was showing that the number of cylindrical shafts is significantly greater than other geometries **(Muramatsu & Abe, 1996, Aye & Arunasoruban, 2014)**. Moreover, the excavation inside vertical shaft is one of the issues that should be taken into consideration, since the uneven earth pressure distributing along the shaft wall might be related with the excavation ratio or excavation depth.

In general, the soil stratum has a difference characteristic depending on the crucial point. In this research, the aim for underground water flow is interested, henceforth, the

soil layer is basically divided by their hydraulic property as four main types; 1. Aquifer, 2. Aquiclude, 3. Aquitard, and 4. Aquifuge as shown in **Table 1.1**. The construction of deep underground structure normally has high possibility to encounter with groundwater which is unaviodable due to the deep construction might reach to an aqifer layer. According to the vertical shaft construction, the bottom of shaft structure might be located at the aquiiclude or aquifuge which is impermeable layer, however, during the construction processes, it might pass through aquifer layer in which water flow is much influencing on the excavation sequence and its stability. Underground water is one of the common topics for underground construction which basically influence on both lateral earth pressure distribution and stability of excavation. Therefore, the pioneer investigation of this research work is the mechanical behavior of the surrounding soil behavior during an excavation process which will be conducted by commercial software (FLAC3D). The basic information will be clarified such lateral earth pressure, heaving soil and relative mean effective stress.

Table 1.1. Hydraulic properties of each geological groundwater formations

Properties	Aquifer	Aquitard	Aquiclude	Aquifuge
Water storage	✓	✓	✓	×
Permeability	Permeable	Partly permeable	Impermeable	Impermeable
Yield of water	✓	✓ (slow yielding)	×	×
Example	Sandy, gravel	Sandy clay	Clay	Compact rocks

Furthermore, the calculation of two-directional flow is conducted to simulate an experimental model of flow beneath sheet pile which is the same mechanism with dewatering in vertical shaft construction. In the experiment model, fluid flow is generated in accordance with applying different hydraulic head between both side of sheet pile,

therefore, the fluid starts to flow from upstream through the bottom of sheet pile as shown in **Figure 1.5**.

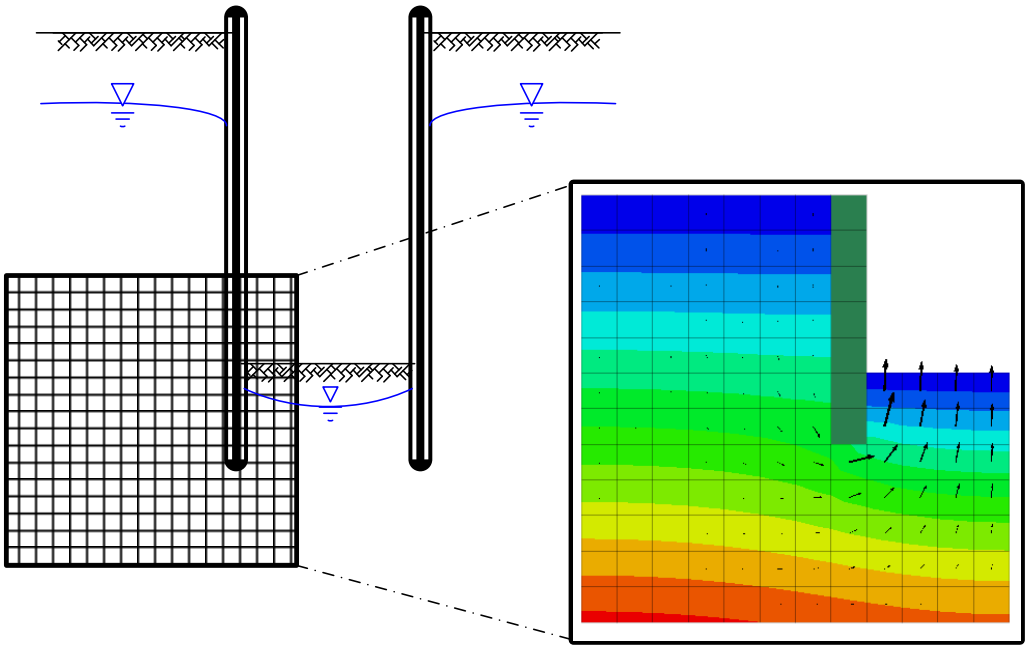

Figure 1.5. The fluid flow beneath the bottom of shaft

The elucidation of mechanical behavior of soil and its stability could be showing by the utilization of commercial software (FLAC3D). The lateral earth pressure acting on deep cylindrical shaft shows a difference tendency from the classical estimation from Rankine's earth pressure. According to the stability of excavation process, heaving soil is likely depending on the excavation depth. Eventually, the investigation on the erosion model, consideration in only drag force exerting on particle could show a better result than other force formation. Since, this is a particle flow in porous media, therefore, the buoyant force and gravitational force might not be dominant in the particle flow.

Nevertheless, the commercial software which was used could not shed light on the erosion which is a crucial topic subjected to groundwater flow. According to **Figure 1.6**, the construction process of vertical shaft in high groundwater area is always associated by dewatering method which directly causes a differential pressure head in the soil between inside shaft and outside shaft. According to this behavior, the fluid starts to flow from surrounding area through the soil beneath the bottom of shaft and flowing upward to the excavation surface. Moreover, the deep vertical shaft construction is

compelling more depth of dewatering location, consequently, the fluid flow become higher in accordance with greater hydraulic gradient. The erosion is mainly caused by the high seepage flow in which small particle tends to flow together with fluid flow. Therefore, the large settlement is probably occurred at the bottom of shaft which could cause a structure failure and safety of construction.

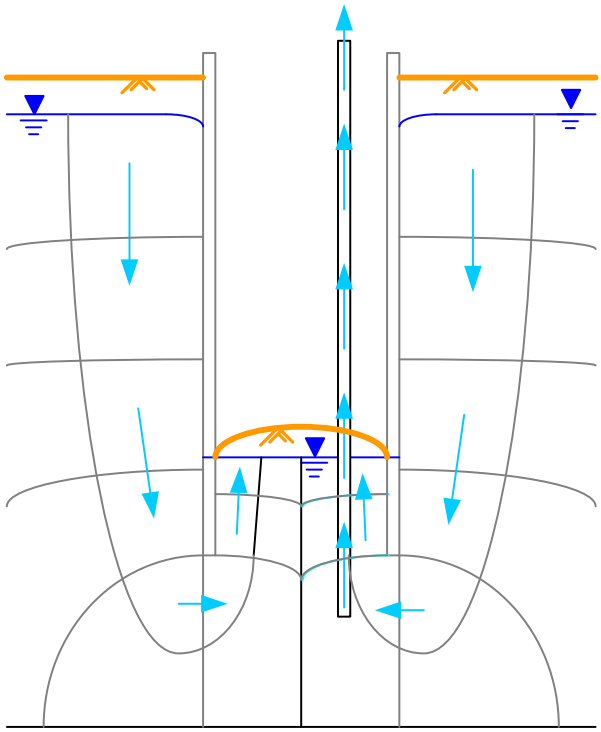

Figure 1.6. The ground water flow after dewatering process

According to the limitation of commercial software and previous numerical scheme for suffusion, the new method of numerical modelling for suffusion is developed in this research. However, the new calculation scheme still could not assure the result without validation, therefore, the validity of the erosion model is also examined by the comparison with previous experiment from Ke and Takahashi (2014). They had investigated the internal erosion by using the small sample under the constant Darcy's flow.

After examination on erosion model validity with previous experiment, further analysis aims to simulate a coupling simulation of particle-fluid flow. According to the previous simulation, the fluid flow velocity was controlled as a constant number as

following the experiment, even if there is a change in porosity and permeability. In this section, the additional scheme of fluid flow simulation is required in which Finite Difference method has been used to discretize the partial differential equation of diffusion. The difference between particle-fluid flow coupling simulation and the particle flow simulation is mainly associated by the changes in fluid flow velocity caused by changes in hydraulic gradient as follow the calculation scheme in **Figure 1.7**.

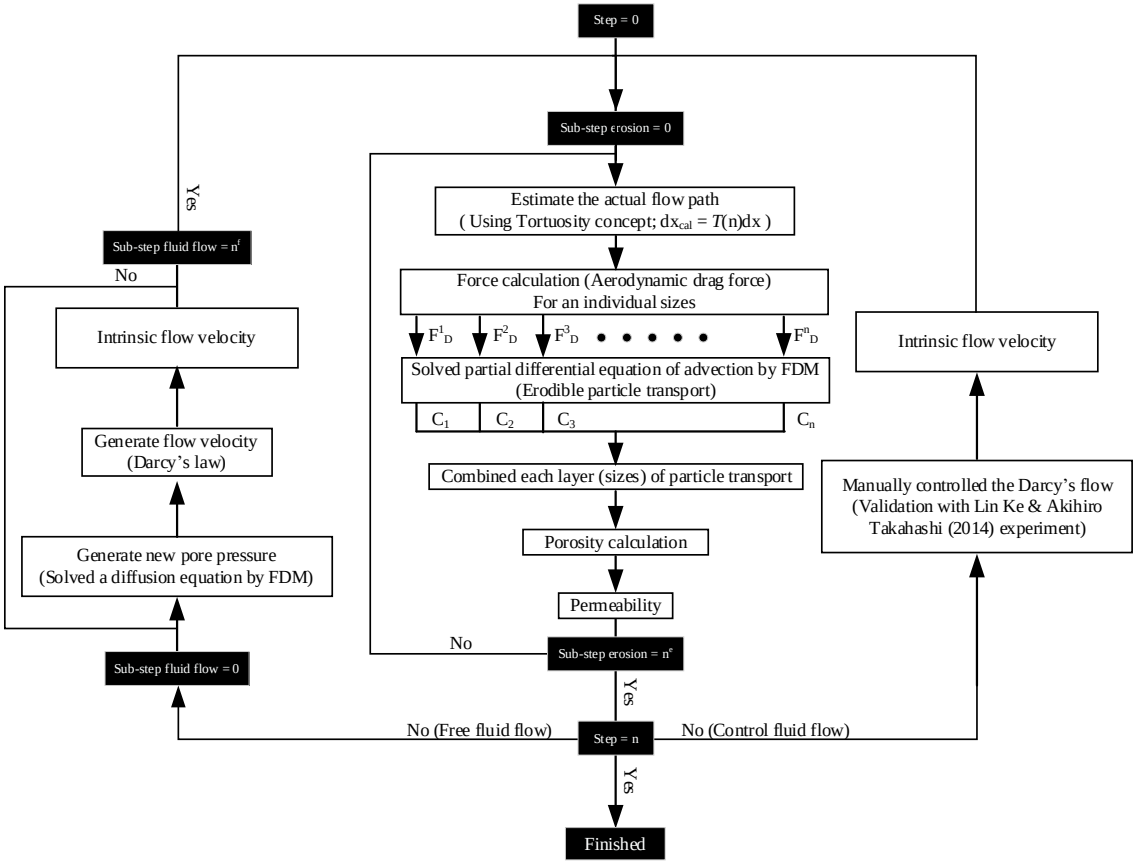

Figure 1.7. Calculation scheme of erosion model

In the last section, the simulation of suffusion nearby vertical shaft structure by numerical scheme developed in this research. As it discussed earlier, the dewatering process is the main cause of seepage flow along vertical shaft. Therefore, the simulation of two-dimensional analysis is eventually conducted to show the different erosion behavior undergoing with different hydraulic head which is controlled by dewatering depth.

Eventually, this thesis will process the study with several chapter since the

literature review as shown in **Figure 1.8**. Subsequently, the basic calculation of vertical shaft by commercial software is performed to show the fundamental behavior of vertical shaft construction in high groundwater area. The erosion calculation is explained in chapter 4 with some conceptual idea of simulation and modification. Furthermore, the chapter 5 is about the particle-fluid flow coupling simulation which was prepared for numerical simulation with two-dimensional analysis in gravitational field as in chapter 6.

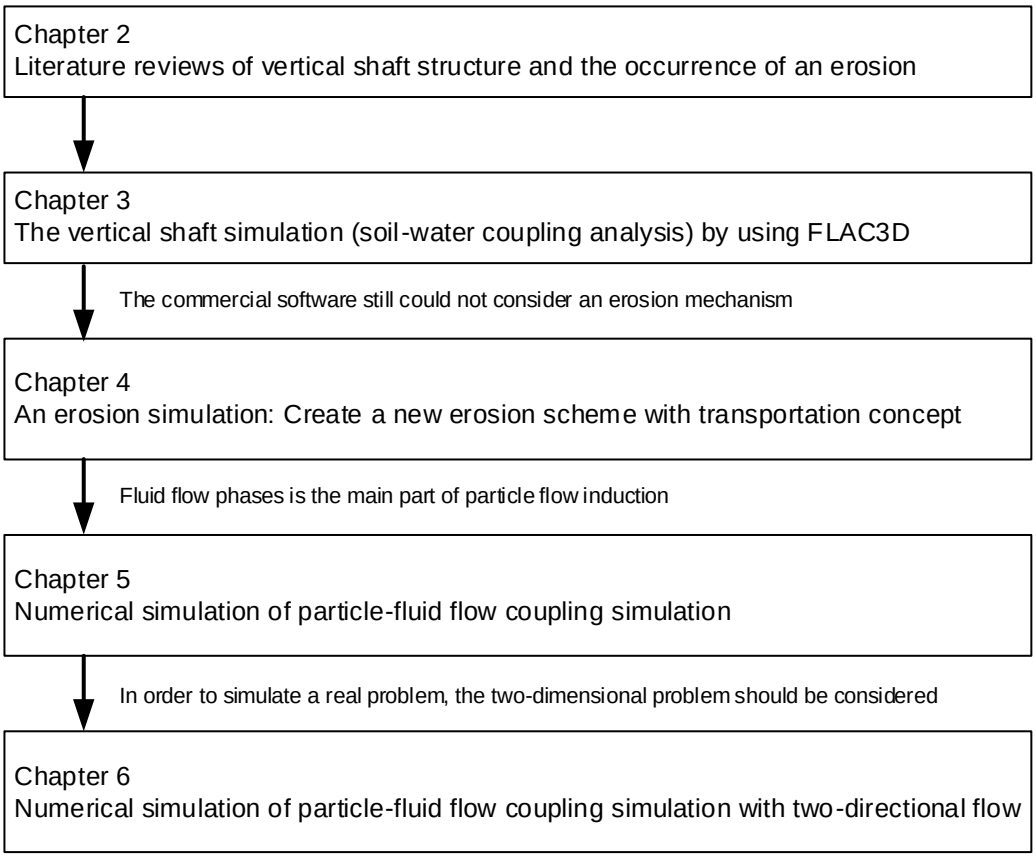

Figure 1.8. Thesis structure

Chapter 2 Literature review

2.1 The underground construction undergoing with erosion

The underground construction is sometimes encountered with high groundwater level in accordance with deep excavation or shallow water table. The shaft structure is standing for accessing underground space. However, the issue of underground water is generally mitigated by the utilization of temporary dewatering system.

2.1.1 Dewatering of shaft

The dewatering inside vertical shaft is basically reducing the groundwater, then, the shaft wall or grouting process can be continued. Furthermore, mine construction normally require a deep vertical shaft, in example, the construction of copper mine with the deep shaft (deeper than 400 m), while the groundwater table was located at 100~135m **(Gabora M. et al.; 2015)**. Nevertheless, not only the mine construction is always facing with groundwater, but the shaft construction in urban area as well. According to the geological condition, the ventilation shaft of metro line in Fuzhou, China, which was constructed in urban area, encountered with very shallow groundwater level (close to ground surface) as shown in **Figure 2.1 (Cao C. et al.; 2019)**.

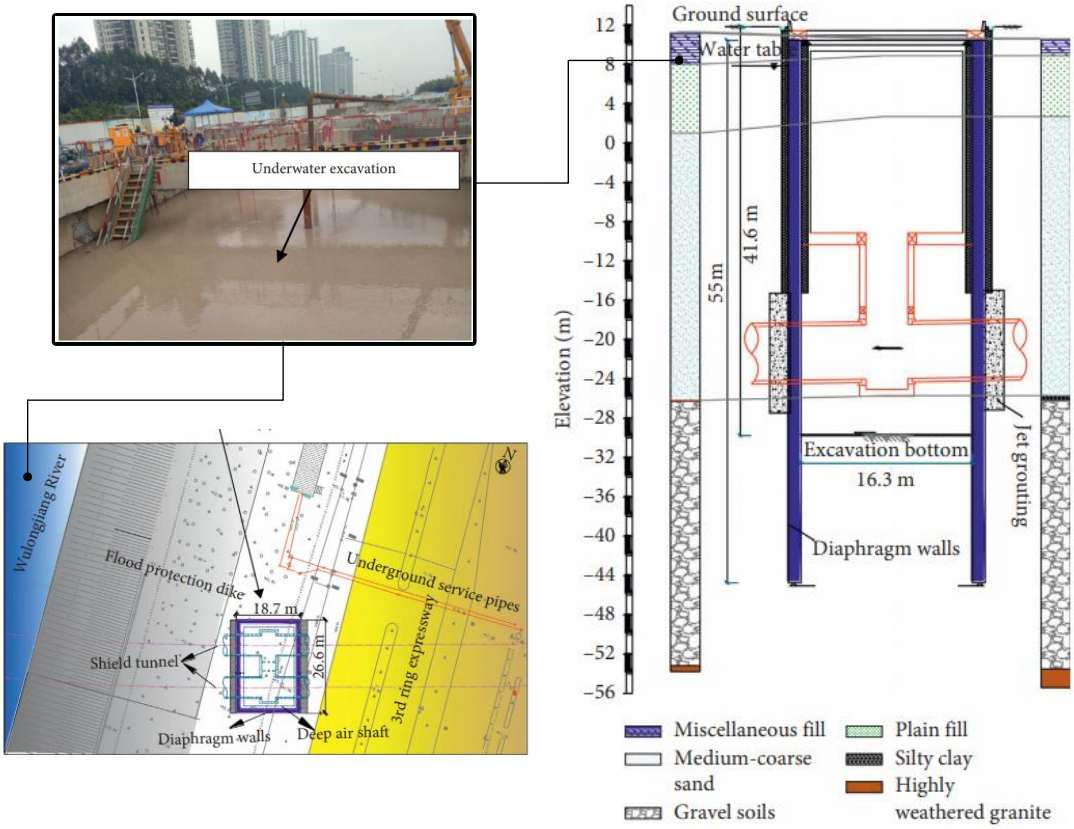

Figure 2.1. The construction of ventilation shaft in Fuzhou, China (Cao C. et al.; 2019)

Furthermore, this research also reported the water level inside vertical shaft as well as the groundwater surrounding vertical shaft as shown in **Figure 2.2**. The observation was obviously showing that the ground difference of water level between inside and outside shaft is about 4~22 meter depending on dewatering stage.

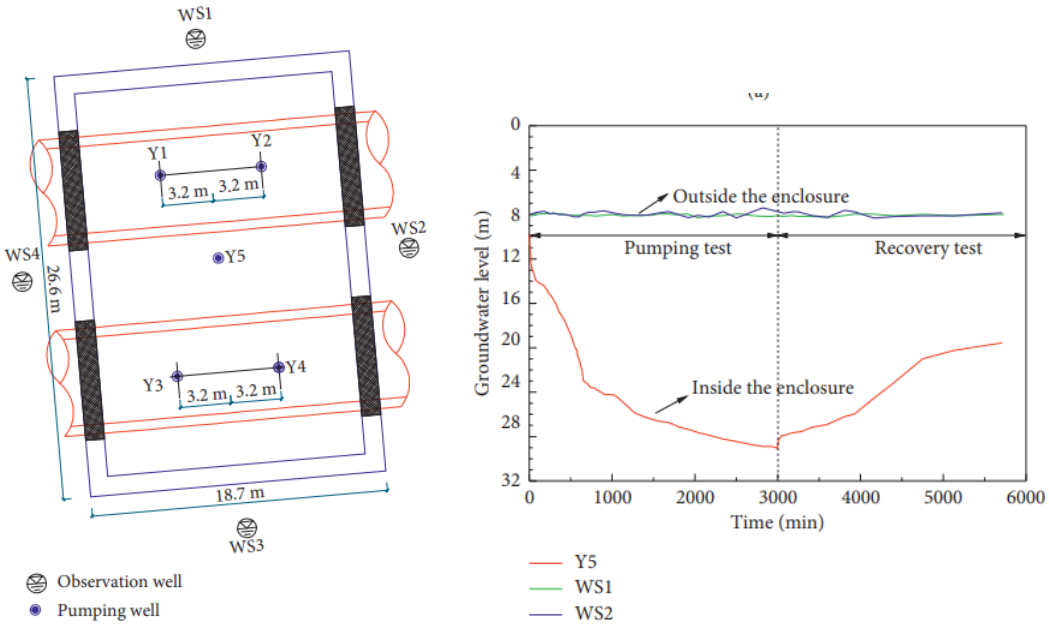

Figure 2.2. The observation of groundwater level and water level inside vertical shaft

In actual field of shaft construction, the erosion is rarely observed in according with the difficulty and limitation of measurement equipment. Nevertheless, the difference of water head (inside and surround shaft) is basically inducing the seepage flow which could cause a seepage failure. One of the seepage failures is an erosion, the erosion is normally occurred when the seepage flow become higher, hence, the soil particle is likely detached by the fluid flow.

2.2 Erosion mechanism

Erosion is the mechanism that the soil is detached from the soil mass which is mainly induced by the motion of fluid. Mostly, the mechanism begins from the irregular seepage flow pass through the media, then, the soil particle tends to move together with the fluid movement in accordance with the external force acting on the moveable particle. The erosion basically occurred in the permeable material where the seepage flow is passing through and the soil structure become unstable. **Gabriella M. (2016)** concluded that there are three main type of erosion mechanism; 1. Internal erosion, 2. Contact erosion, and 3. Concentration leak erosion, as shown in **Figure 2.3 (Gabriella M.; 2016, Bonelli S.; 2013, Robbins B.A. & Griffiths D.V.; 2018)**.

Internal erosion or suffusion, is the most famous mechanism among several erosion types, in addition, many researchers are targeting to solve this erosion behavior with both numerical modelling and experimental process. Generally, the soil that always encounters with internal erosion is a gap grade soil, the seepage flow generates the excessive force on a fine particle, then, the fine fraction become loosened and moving out from the soil mass.

Contact erosion is normally occurred along the boundary between two soil layer which is different in gradation (fine grain and coarse grain layer). According to the difference in grain sizes, the permeability in both soil stratum would be difference as well, therefore, the flow inside the coarse grain stratum is basically greater than the flow velocity in fine grain stratum. Then, the fine particle along this boundary would be moved due to the excessive seepage flow.

Concentration leak is a local failure, the seepage flow is significantly greater than the surrounding seepage flow in which the separation between the soil mass is generated. Therefore, the seepage flow along an open channel would carry the surrounding soil out from the soil mass.

In addition, there is another erosion type that behavior is similar with the suffusion or internal erosion, but there is no filter at the downstream. Hence, the soil starts to be flowing from the downstream or backside, therefore, this behavior is generally called as backward erosion.

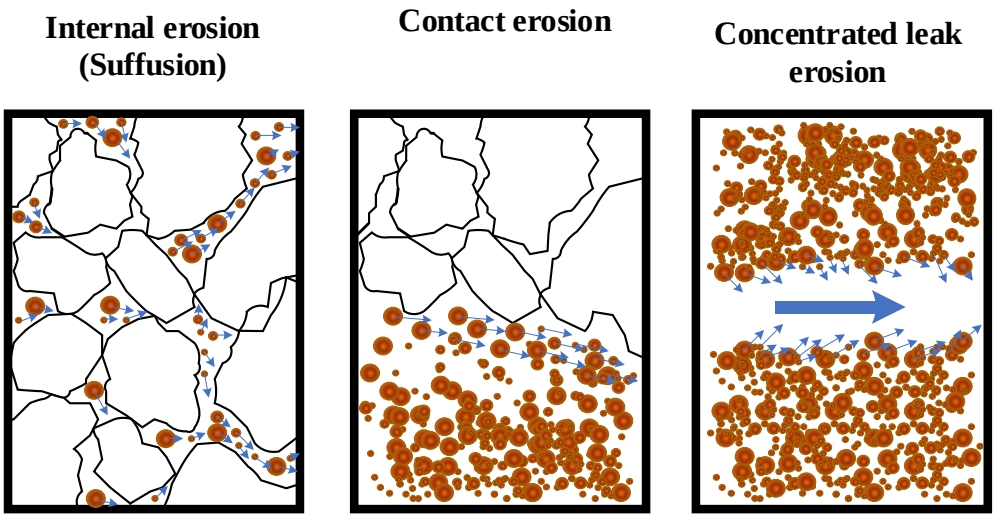

Figure 2.3. The erosion mechanism

Moreover, **Telkar and Pote (2018)** have concluded that the erosion mechanism is made up from three main processes; 1. Detachment, 2. Movement, and 3. Deposition **(Telkar SG. & Pote N.S.; 2018)**.

2.2.1 The erosion failure in earth structure

There are many reports that showing the erosion is a main cause of earth structure failure, especially in embankment or levees. Statistical study is one the common method to observe the major problem in earth structure failure. According to the recorded data from previous research, there is a significant number of erosion failure through the soil foundation, especially in the foundation of dam, abutment, and reservoir **(Foster M., Fell R. & Spannagle M.; 2000)**.

The erosion or piping in the embankment or dam structure is generally divided into four categories as below;

1. Foundation related piping failures
2. Conduit and internal erosion piping failures
3. Possible backwards erosion and suffusion piping failures
4. Piping failure induced by biological activity

Similarly, the investigation on the main reason of earth dam failure in accordance with the above categories through recorded data showed that the erosion or piping caused by conduit and suffusion are playing a big role in earth dam failure **(Richards K.S. & Reffy K.R.; 2007)**.

2.2.2 The internal erosion in earth structure

Erosion is one of the issues in earth structure construction, in general, the underground structure constructed in the place that groundwater level is shallow, as well as the structure which is used for regulating the water level (levee, dike, embankment) is likely encountering with erosion problem. In designing period, especially for embankment, the empirical approach is always used to mitigate an erosion which might cause a structure failure, somehow, the design was not extremely ensuring the safety of structure **(Lane E.W.; 1935)**. According to the difficulties in prediction, there are some studies about erosion in the earth structure by conducting an experiment. **Van Beek V.M.**

et al. (2010) conducted a full-scale test on piping in the levee structure, it was shown that the process begins from large increase of mud flow (fluid-sand mixture) which cause a large area of crack **(Van Beek V.M. et al.; 2010).** Moreover, the investigation on suffusion or internal erosion due to the seepage flow in the embankment was experimentally conducted to show both erosion rate at the downstream side and spatial distribution of fine loss as shown in **Figure 2.4-2.5** (**Horikoshi K, Ke L, Takahashi A.; 2016**). According to the **Figure 2.4**, the fine particle would be travelling to the downstream side (on the left), then, they had checked the cumulative fine loss as in **Figure 2.5** by using small load cell (**Kyowa Electronic Instruments Co., Ltd., LVS-2KA, measurable range: 0–20 N**).

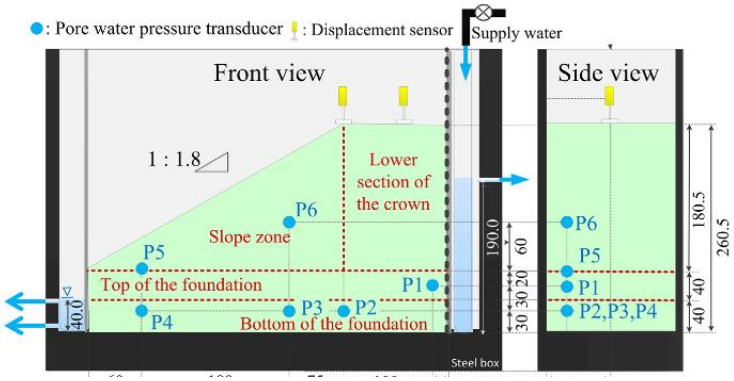

Figure 2.4. Suffusion in embankment experiment from Horikoshi K, Ke L, Takahashi A. (2016)

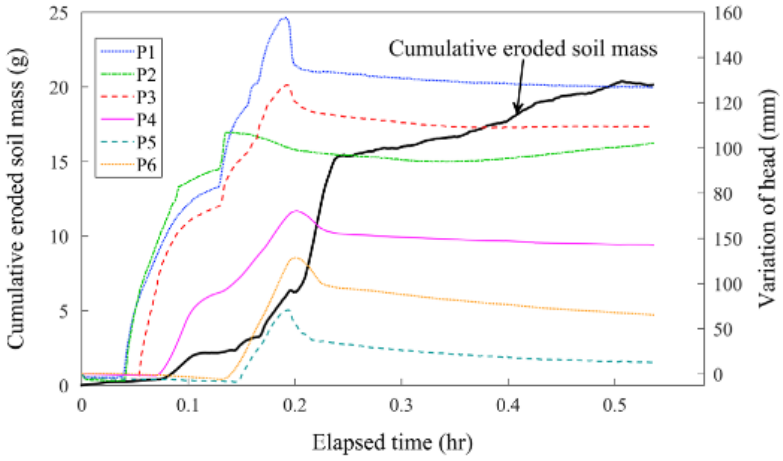

Figure 2.5. Experiment result Horikoshi K, Ke L, Takahashi A. (2016)

2.2.3 The experiment of internal erosion (Soil sample test)

In order to create a numerical model of erosion, the understanding from small test is very essential. Therefore, there are several attempts trying to investigate on erosion by using soil column test in laboratory. In general, an erosion experiment was extensively done for several purpose which might be investigation an initiation of erosion criteria, erosion rate, even or the influence of confining stress on erosion rate.

Tomlinson S.S. and Vaid Y.P. (2000) conducted on erosion test under the confining pressure controlled as shown in **Figure 2.6**, and tried to avoid inconsistencies from using natural sand (material). They were using a glass beads instead of natural material with the nearly uniform distribution in size, as shown in **Figure 2.7**, with the uniform filter which is a combination of glass beads as well **(Tomlinson S.S. and Vaid Y.P.; 2000)**. Furthermore, the advantageous of the glass beads is the specific gravity is about 2.5 which is very close to specific gravity of quartz sand, and the sphericity of glass beads is close to unity.

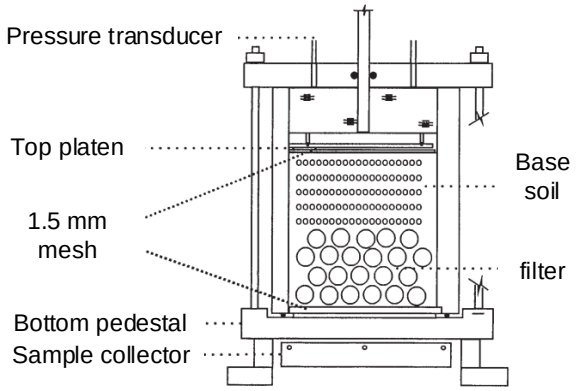

Figure 2.6. The erosion experiment with the utilization of glass bead from **Tomlinson S.S. and Vaid Y.P. (2000).**

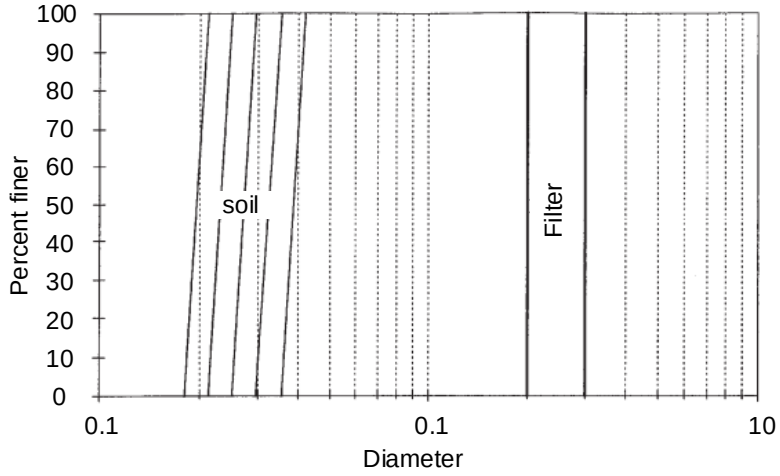

Figure 2.7. The distribution of base soil and filter in cumulative curve from Tomlinson **S.S. and Vaid Y.P. (2000).**

Similar experiment on suffusion with the difference gradation of soil was conducted by Liang Y. et al. (2019), they did a soil column experiment with a gap grad soil as shown in **Figure 2.8** undergoing with isotropic and anisotropic stress **(Liang Y. et al.; 2019)**. This study from Liang Y et al. (2019) tried to use an upward flow through the soil specimen which is an opposite side from the most of erosion experiment. In addition, they mentioned that the erodibility of the fine particle from both anisotropic test and isotropic test are similar except the specimen was collapsed in the anisotropic test.

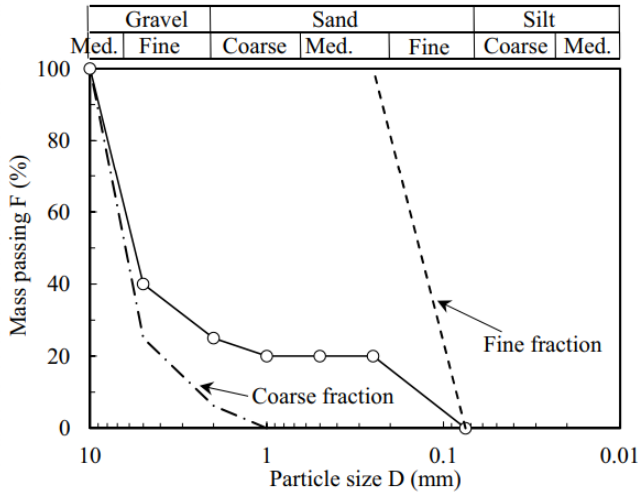

Figure 2.8. the distribution curve of erodible soil and soil skeleton (Liang Y. et al.; 2019)

The experiment that aims to understand in both particle size distribution and the changes in mechanical and hydraulic behavior was done by Bendahmane F., Marot D. & Alxis A. (2008), and they had concluded that low hydraulic gradient is normally inducing a suffusion. Conversely, higher hydraulic gradient is causing a backward erosion. This experiment was done by using cohesionless and cohesive material which is Loire sand and Kaolinite, respectively, as shown in **Figure 2.9**. According to this experiment, the suffusion is subjected to clay material or Kaolinite which combined with very small size of particle, therefore, the content of Kaolinite in this experiment was measured specifically by optical sensor **(Bendahmane F., Marot D. & Alxis A.; 2008)**.

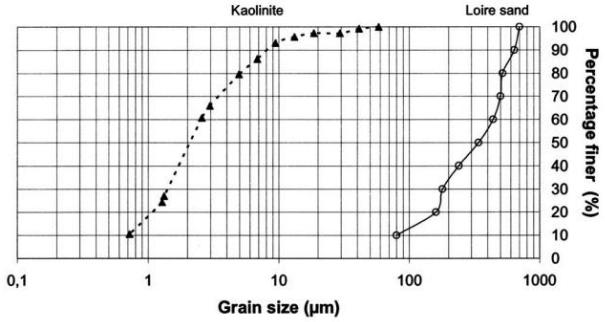

Figure 2.9. the distribution of soil specimen in the backward erosion and suffusion (Bendahmane F., Marot D. & Alxis A.; 2008)

According to the earth structure, the soil mass would not be undergoing only isotropic, therefore, some researchers tried to conduct an erosion experiment under the different stress path. **Changs D.S. & Zhang L.M. (2013)** had done the internal erosion experiment with the gap grade soil as shown in **Figure 2.10** under various stress path; 1. Isotropic, 2. Drain triaxial compression, and 3. Triaxial extension stress paths. This research kept focusing on the initiation of erosion and the erosion rate as well as the other research objective by using the gap grade soil as shown in **Figure 8 (Changs D.S. & Zhang L.M.; 2013)**.

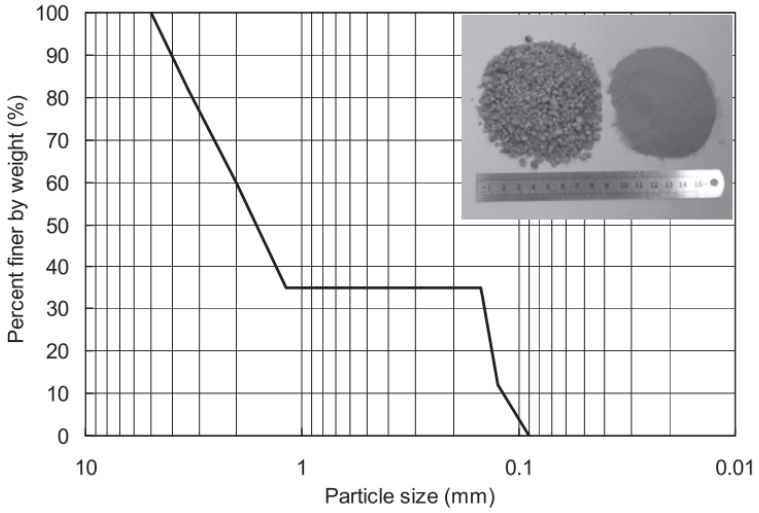

Figure 2.10. The grain size distribution for internal erosion experiment from **Changs D.S. & Zhang L.M. (2013)**

In addition, the soil column test is modified for testing in special issue, especially in embankment dams or levee. **Wan C.F. & Fell R. (2004)** aimed to understand the erosion rate of concentration leak in the embankment by simplifying the problem into hole erosion test (HET) and slot erosion test (SET) which is resulting in initiation of erosion criteria and erosion rate **(Wan C.F. & Fell R.; 2004)**.

2.3 Particle flow in porous media

Internal erosion or suffusion is one of the famous mechanisms of erosion, the fine particle or erodible soil is carried by the motion of solvent, which normally is water. According to the particle transportation including physics or engineering field, the advection is one of the equations that can be properly simulating a particle transportation inside porous media. Previously, many researchers had conducted a simulation from advection equation to show a behavior of flowing substance in several field. The advection equation is sometime called as partial balance of mass, as in the research from Yang et al. (2020), the internal erosion is analyzed by using advection as governing equation **(Yang et al.; 2020)**. **Russell EM (1992)** investigated on both experiment model and analytical model of solid particle flow through porous media, the calculation which

was used in particle flow simulation is the advective form **(Russel Em.; 1992)**. **Koenders and Williams (1992)** also suggested the use of advection equation for solving the mechanism of the particle motion with non-shearing flow in particle fluid-mixture as shown in **Equation 2.1**, furthermore, the microscopic constitutive law was included to consider the fluidization as well **(Koenders MA and Williams; 1992)**.

$$\frac{\partial \emptyset_p}{\partial t} + \frac{\partial}{\partial x}(\emptyset_p v_i) = 0 \tag{2.1}$$

Where, $\emptyset_p$ is the solid fraction, and v_i is a particle velocity.

Some of the previous research investigating on the erosion mechanism have used the advection equation to show a behavior of erodible particle or fine particle flow as well as the simulation of particle flow in others field. The progression of backward erosion piping (BEP) is also one of the erosion mechanisms and, one of the simulation models to predict the piping failure in the heterogeneous soil behind levee, as shown in **Figure 2.11**, had done by using advection equation as mathematical model to solve eroded particle transport **(Liang Y. et al.; 2017)**.

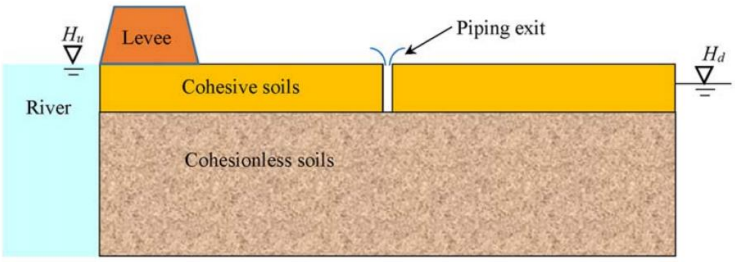

Figure 2.11. the schematic section of the backward piping erosion model from **Liang Y. et al. (2017)**

2.4 Soil model (Composition of soils) for an erosion model

According to the internal erosion or suffusion behavior, part of the soil mass would be detached from the soil mass due to the influence of fluid motion. Therefore, the conventional soil model could not represent the soil composition in which the erodible soil fraction is stored. The common method to modify the conventional soil model to be used in erosion calculation is adding an extra section for being as an erodible soil fraction

(Fujisawa K., Murakami A. & Nishimura S-I.; 2010). The soil model that Fujisawa et al. had used is composed of air phase, fluid phase, and solid phase in which divided as erodible and soil skeleton as shown in **Figure 2.12**. Moreover, **Liang Y. et al. (2017)** modified the soil composition for piping simulation by suggesting movable particle fraction and moving particle fraction as in **Figure 2.13**, where the movable particle is standing for the erodible particle, while the moving particle is the mass that can be transferred to movable fraction with enough hydraulic gradient **(Liang Y. et al.; 2017)**.

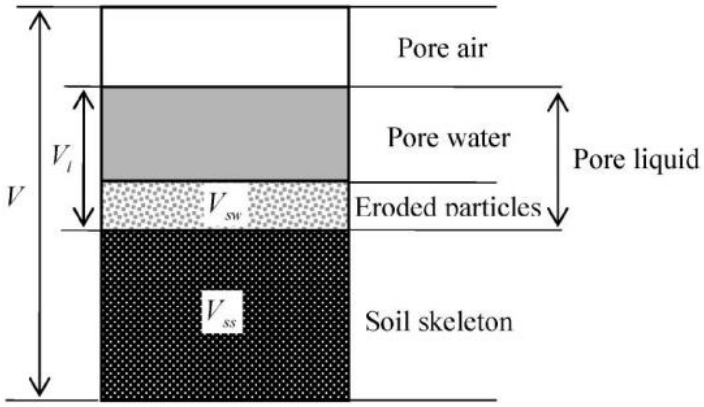

Figure 2.12. Soil model for erosion model **(Fujisawa K., Murakami A. & Nishimura S-I.; 2010)**

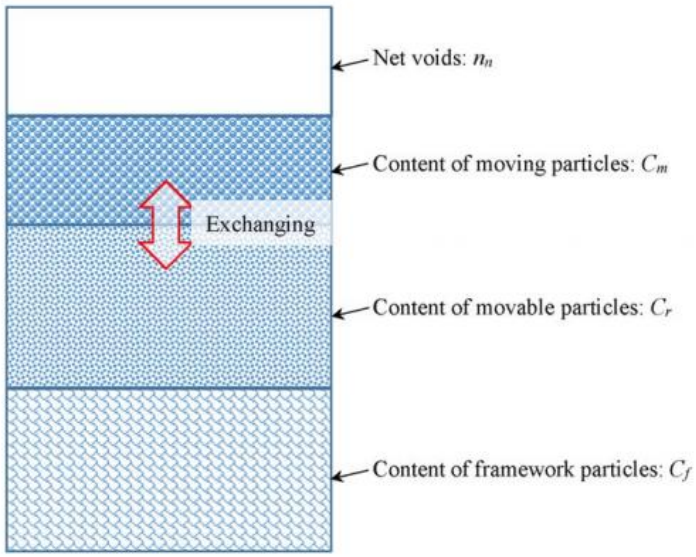

Figure 2.13. The composition of soil for erosion issue **(Liang Y. et al.; 2017)**

2.5 Erosion simulation model

The prediction in erosion behavior have been extensively studied, but there are plenty factors affecting on the erosion mechanism. Moreover, previous researchers tried to implement several concepts to describe the erosion characteristic depending on their focal point. Therefore, most of the erosion model is based on the empirical equation which is generally obtained from the experiment. Generally, in order to simulate an erosion, two components are mainly considered which is initiation of erosion and erosion rate.

The pioneer research work in developing an erosion model was done by **Khilar K.C. and Fogler H.S. (1958)** which is the modelling of piping-plugging in earthen structures. They mentioned that the relative size between pore constrictions and the fine particle is very important to justify a piping or plugging. Moreover, the particle is tended to detach out from the soil mass while the particle is should be much smaller than pore constriction (<0.01), which could be refer to gap grade soil. The calculation modelling was simplified to a one-dimensional calculation with continuous longitudinal segment as shown in the **Figure 2.14**. **Khilar K.C. and Fogler H.S. (1958)** considered the mixture of solid and liquid as a well mixture, therefore, the fluid velocity, as obtained from **Equation 2.2**, is used to replace in the mass balance equation as shown in **Equation 2.3 (Khilar K.C. and Fogler H.S.;1958)**.

$$q_0 = \frac{K_0}{\mu} A \left(\frac{\Delta p}{\Delta L}\right) \tag{2.2}$$

Where, q_0 is initial flow rate, A is a cross-sectional area, K_0 is initial absolute permeability, $\frac{\Delta p}{\Delta L}$ is a pressure gradient, and μ is viscosity of liquid.

$$[qC_{i-1} - qC_i] + A_{si} r_{ri} - n_i V_i r_{ci} = \frac{d}{dt}(n_i V_i C_i) \tag{2.3}$$

Where, C_i is the concentration of particles in the segments i, r_{ri} is rate of surface erosion in the i segment, r_{ci} is a volume rate capture in segment i, A_{si} is the surface area of segment i, n_i is the porosity of segment i, and V_i is the volume of segment i.

In this erosion model, the rate of erosion was obtained from the experiment as shown in **Figure 2.15**, as a relationship between a rate of change in erosion rate, α, and critical shear stress, τ_c. Then, they had summarized that the relation between those variables can be expressed as in the **Equation 2.4**. Henceforth, the surface erosion, which is used in the **Equation 2.3**, can be calculated as in the **Equation 2.5**.

$$\alpha = 30 - 17.09\tau_c + 4.02\tau_c^2 - 0.43\tau_c^3 + 0.0175\tau_c^4 \quad (2.4)$$

$$r_r = \alpha(aq - \tau_c) \quad (2.5)$$

Where, a is a constant ratio between surface shear stress and flow rate.

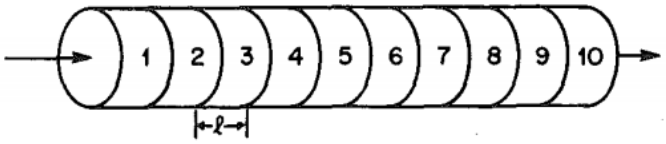

Figure 2.14. Cylindrical model for earthen structure from **Khilar K.C. and Fogler H.S. (1958)**

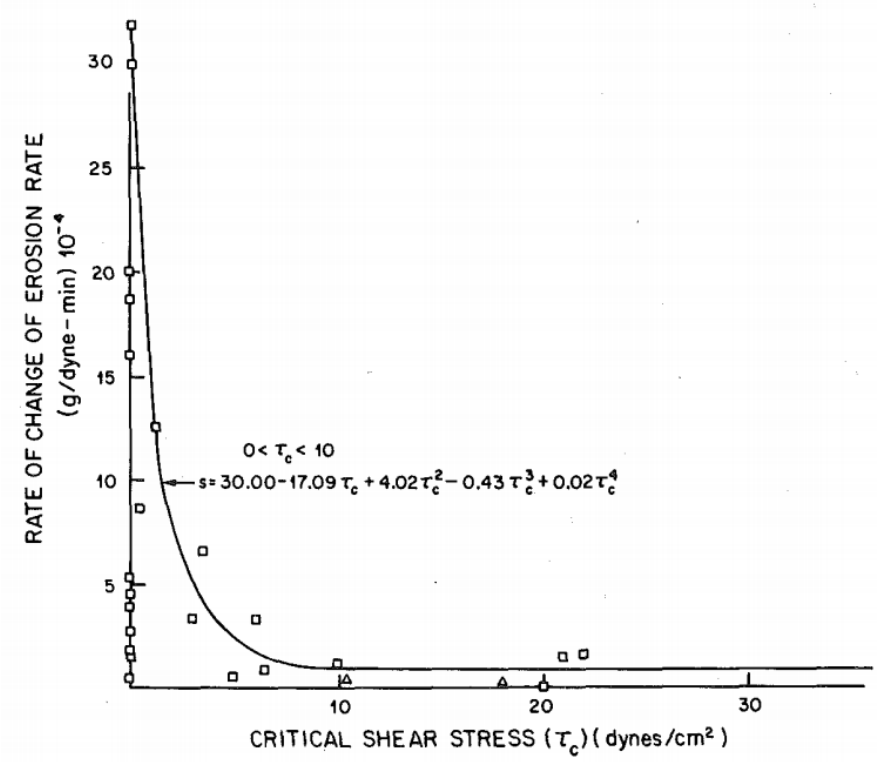

Figure 2.15. The relationship between rate of change or erosion rate and critical shear stress from **Khilar K.C. and Fogler H.S. (1958)**

2.5.1 Erosion rate and initiation of erosion

In general, the equation which is used for representing an erosion rate and initiation of erosion is always expressed in single equation. The rate is normally represented by the α, while the initiation of erosion is basically shown in the term of differences between

hydraulic shear stress, τ_a, and critical hydraulic shear stress, τ_c, which means if the hydraulic shear stress is greater than critical hydraulic shear stress, the erosion starts to occur. The erosion rate is one of the major issues in erosion modelling. According to the erosion rate, there are various suggestions about the equation, which generally comes from an early equation as shown in **Equation 2.6 (Arulanandan K., Krone R.B. & Loganathan P.; 1975, Chaney R., Demars K., Reddi L., Lee I-M. & Bonala M.; 2000).**

$$\dot{\varepsilon} = \alpha(\tau_a - \tau_c) \tag{2.6}$$

Where, $\dot{\varepsilon}$ is erosion rate, α is a coefficient of soil erosion (constant value), τ_a is a hydraulic shear stress, and τ_c is critical hydraulic shear stress.

In the aspect of energy dissipation, the particle might be moving in accordance with the exerting energy from fluid flow **(Indraratna B., Muttuvel T. & Khabbaz H.; 2009)**. Hence, the adjustment in the original equation has been applied by suggesting a new α as shown in the **Equation 2.7**.

$$\alpha = \frac{\omega v \rho_d}{\left(\frac{3E_T}{Ad} + \rho_d \frac{v^2}{2}\right)} \tag{2.7}$$

Where, ω is efficiency index, v is mean flow velocity through a pipe, ρ_d is dry density of the soil, E_T is the energy required to break number of interparticle bonds in the fracture plane, A is area of fracture plane, and d is mean particle diameter.

2.5.2 The erosion transportation

Erosion transportation is one of the topics that is importance for modelling an erosion in earth structure. In general, the particle flow velocity is replaced by the fluid flow velocity under the assumption of the well-mixture **(Fujisawa K., Murakami A. & Nishimura S-I.; 2010, Liang Y. et al.; 2017)**. But previous research was not focusing on this topic as much. Nevertheless, the experiment test on sand boiling was shown that the particle velocity is different from the fluid flow velocity **(Fujisawa K., Murakami A., Nishimura S. &Shuku. T.; 2013)**. The experiment of sand boiling was conducted with uniform gradation of silica sand in both vertical and horizontal direction as shown in **Figure 2.16** and **Figure 2.17**, respectively. The particle flow velocity and fluid flow velocity has been obtained from the monitoring volume change in each fraction as shown in **Equation 2.8** and **Equation 2.9** as fluid velocity and particle velocity, respectively.

According to those velocity, it can be concluded that the particle flow velocity is generally slower than the fluid flow velocity. Furthermore, the upward seepage flow and particle flow velocity are likely predicable, while, those flow velocities in the horizontal flow are still uncertain.

$$\tilde{v}_{w,z} = \frac{\Delta V_w}{nA\Delta t} \tag{2.8}$$

$$\tilde{v}_{s,z} = \frac{\Delta V_s}{(1-n)A\Delta t} \tag{2.9}$$

Where, V_w is volume of fluid, V_s is the volume of sand, n is porosity, A is the cross-sectional area, and t is time.

Furthermore, they tried to clarify the particle flow velocity by considering the relation between microscopic scale and macroscopic scale. The pressure was considered as microscopic function as shown in **Equation 2.10**. The seepage force which is generally a force in macroscopic scale, $f(X)$, is described alternatively in microscopic scale as in **Equation 2.11**. Eventually, the analytical solution based on microscopic assumption shows that the particle flow velocity could be calculated as in the **Equation 2.12 (Fujisawa K., Murakami A., Nishimura S. &Shuku. T.; 2013, Vardoulakis I., Stavropoulou M. & Papanatasiou P.; 1996)**.

$$p(X,y) = \bar{p}(X) + \frac{\partial \bar{p}(X)}{\partial X} y + p^*(X,y) \tag{2.10}$$

Where, X is the location on macroscopic domain, y is the location on microscopic domain, $\bar{p}(X)$ is an average pressure, $\frac{\partial \bar{p}(X)}{\partial X}$ is the gradient of pore pressure, and $p^*(X,y)$ is the local variation of pressure in microscopic domain.

$$f(X) = \frac{1}{V_y}\int_{\Gamma_s} p(X,y) v dS_y + \frac{1}{V_y}\int_{\Gamma_s} \tau(X,y) dS_y \tag{2.11}$$

Where, v is a unit normal vector on the surface of particle, Γ_s is a surface of particle, τ is a friction stress vector, V_y is the volume of the domain in microscopic scale, and S_y is surface area.

$$\tilde{v}_{s,z} = \tilde{v}_{w,z} - \frac{k(1-n)}{n^2}\left(\frac{\rho_s}{\rho_w} + \frac{1}{\rho_w g}\frac{\partial \bar{p}}{\partial z}\right) \tag{2.12}$$

(a) Experiment for vertical sand migration

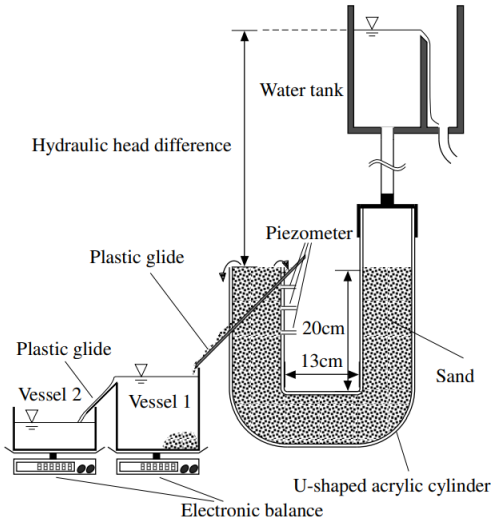

(b) Upward velocity of sand and seepage water

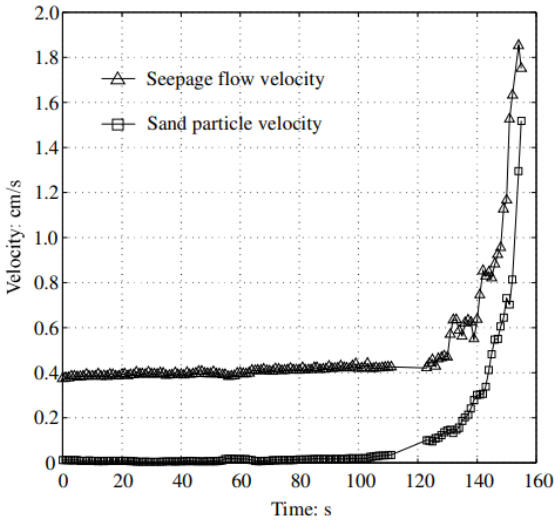

Figure 2.16. The experiment of sand migration in vertical direction by using U-shape acrylic cylinder **(Fujisawa K., Murakami A., Nishimura S. &Shuku. T.; 2013)**

(a) Experiment for horizontal sand migration

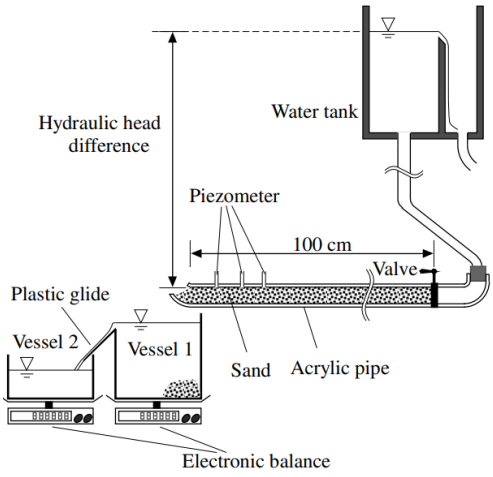

(b) Horizontal velocity of sand and seepage water

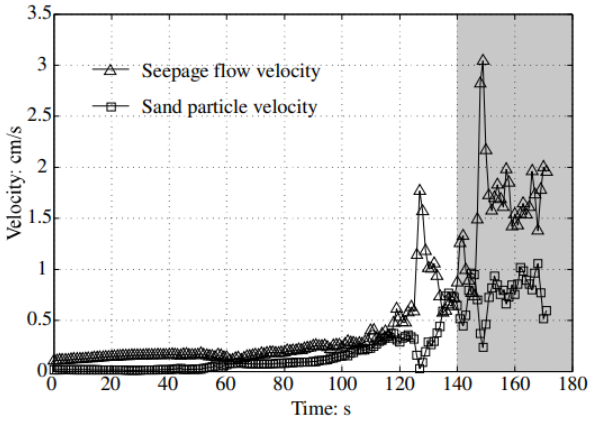

Figure 2.17. The experiment of sand migration in horizontal direction by using acrylic pipe **(Fujisawa K., Murakami A., Nishimura S. & Shuku. T.; 2013)**

2.6 Lifting force

The erosion is the mechanism that the group of particles including different size of particle is detached from the soil mass, therefore, the force exerting on a particle might not be

coming from only surrounding fluid but surrounding particle as well. The consideration of particle intruder is the beginning to understand the lifting force exerting on the particle. The segregation phenomenon in small and large granular flow was firstly studied by **Guillard F, Forterre Y. & Pouliquen O. (2016)**. The two-dimensional discrete element method was used to investigate the single particle segregation as shown in **Figure 2.18**. According to this study, it shows that the particle intruder which the size is relative larger than surrounding particle tends to move upward in accordance with segregation force, F_{seg}. After the conducting a series of simulation as shown in **Figure 2.19**, they concluded that the normalized segregation force with buoyant force could be explained in the term of diameter ratio as in **Equation 2.13 (Guillard F, Forterre Y. & Pouliquen O.; 2016)**.

$$F_{seg} = -\pi \frac{d_c^2}{4}\left(\mathcal{F}\left(\mu, \frac{d_c}{d}\right)\frac{\partial P}{\partial z} + \mathcal{G}\left(\mu, \frac{d_c}{d}\right)\frac{\partial |\tau|}{\partial z}\right) \tag{2.13}$$

Where, $\mathcal{F}\left(\mu, \frac{d_c}{d}\right)$ and $\mathcal{G}\left(\mu, \frac{d_c}{d}\right)$ are the empirical function of friction coefficient, $\mu = \frac{|\tau|}{P}$, and particle size ratio, $\frac{d_c}{d}$, d_c is a particle intruder size, and d is size of surrounding particle, $\frac{\partial P}{\partial z}$ is pressure gradients, and $\frac{\partial |\tau|}{\partial z}$ is shear stress gradient.

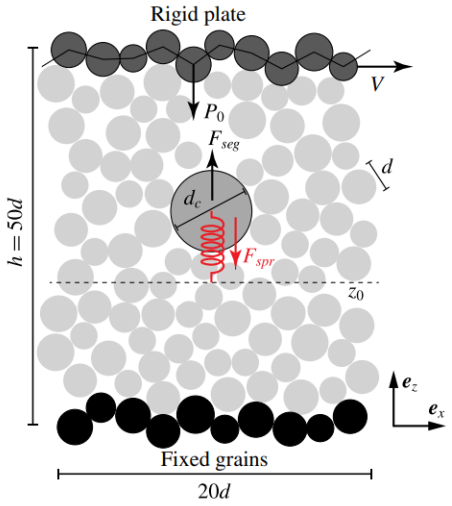

Figure 2.18. The discrete element analysis for particle intruder **(Guillard F, Forterre Y. & Pouliquen O.; 2016)**

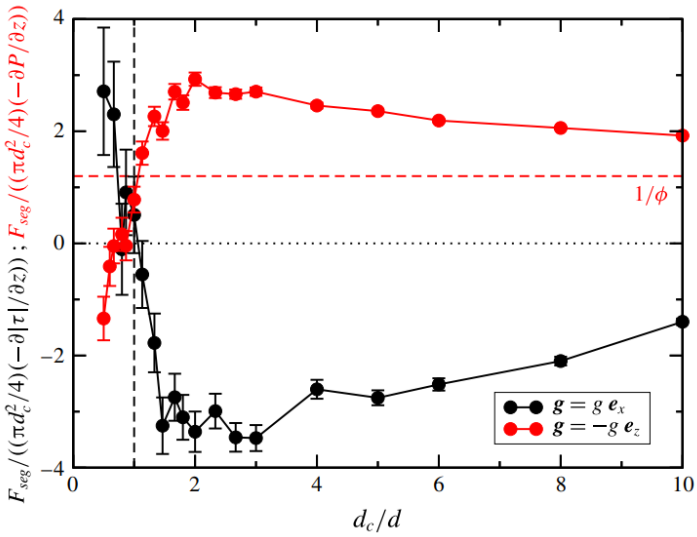

Figure 2.19. the segregation force as a function of particle size ratio **(Guillard F, Forterre Y. & Pouliquen O.; 2016)**

Moreover, some other research tried to approach a particle segregation undergoing agitation was conducted by three-dimensional discrete particle method and firstly shown a pressure field surround particle intruder as in **Figure 2.20 (van der Vaart K., van Schrojenstein Lantman M.P., Weinhart T., Luding S., Ancey C. & Thornton A.R.; 2018)**. In the simulation of particle intruder, they had simulated the intruder particle at several location, but only the middle of domain was picked up to show in accordance with the boundary effect. According to the pressure field result, the cross-section at the center of particle intruder of pressure field was shown in two difference contours, the original pressure field, P as shown in **Figure 2.20(a)**, could be perceived that it is including hydrostatic pressure, P_H, and nonhydrostatic pressure, P_L. Conversely, the nonhydrostatic pressure file was obtained by the relationship of $P_L = P - P_H$, therefore, the pressure file of nonhydrostatic is shown in **Figure 2.20(b)**. The nonhydrostatic pressure shows that when the particle ratio, S, or the size of particle intruder become larger, the nonhydrostatic pressure is much affective. Furthermore, they had investigated on the three main component of force, F_L is lift force, F_b is buoyant force, and F_{gz} is gravitational force, acting on the particle and shown in the **Figure 2.21**.

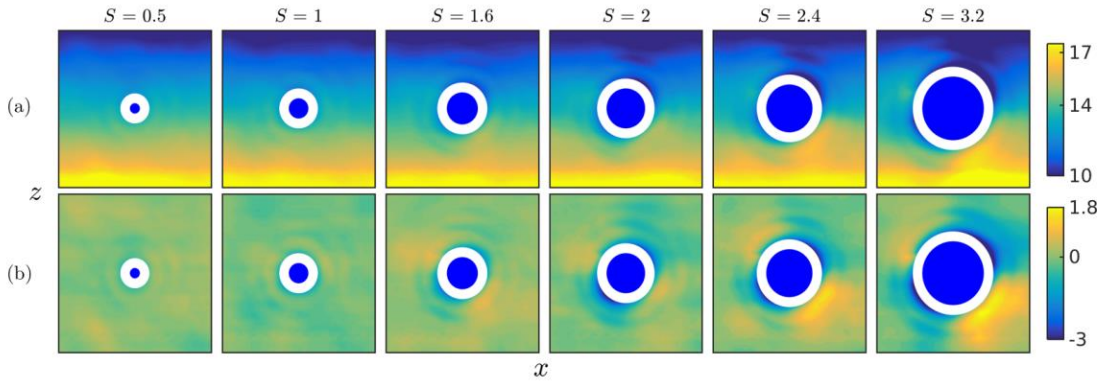

Figure 2.20. (a) The original pressure surrounding particle intruder (b) The pressure field of nonhydrostatic effect **(van der Vaart K., van Schrojenstein Lantman M.P., Weinhart T., Luding S., Ancey C. & Thornton A.R.; 2018)**

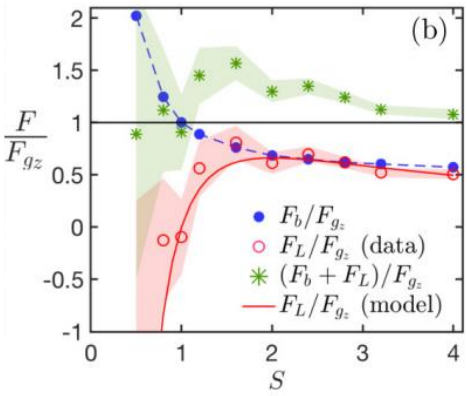

Figure 2.21. The measured force component from the simulation **(van der Vaart K., van Schrojenstein Lantman M.P., Weinhart T., Luding S., Ancey C. & Thornton A.R.; 2018)**

2.7 Buoyancy force

Buoyant force is the force that fluid exert on the object with the opposite direction from its weight. The most classical expression from Archimedes is that "Any object, wholly or partially immersed in a fluid, is buoyed up by a force equal to the weight of the fluid displaced by the object".

The buoyancy force on an object in fluid is already well described by Archimedes, but the buoyancy in the granular mixture flow is obscure and more complicated.

According to the study of particle intruder, it shows that the buoyant force on particle flowing in fluid-granular mixture might not be following a classical theory from Archimedes. Thereafter, **Alok Kumar et al. (2019)** theoretically investigated on the buoyant-gravitational force ratio. They suggested that the buoyancy force of particle intruder, F_{By}, is the function of the partial molar volume, $\tilde{V}_i$, as following the **Equation 2.14-2.15 (Kumar A., Khakhar D.V., Tripathi A.; 2019)**.

$$F_{By} = \emptyset \rho_p \tilde{V}_i g_y \tag{2.14}$$

$$\tilde{V}_i = \left(\frac{\partial V}{\partial N_i}\right)_{P,T,N_j} \tag{2.15}$$

Where, the ρ_p is particle density, g_y is a gravity, $\emptyset$ is a total solid fraction.

Moreover, the comparison between numerical simulation from **van der Vaart K et al. (2018)** and theoretical calculation from **Alok Kumar et al. (2019)** was shown an excellent correlation as shown in **Figure 2.22**.

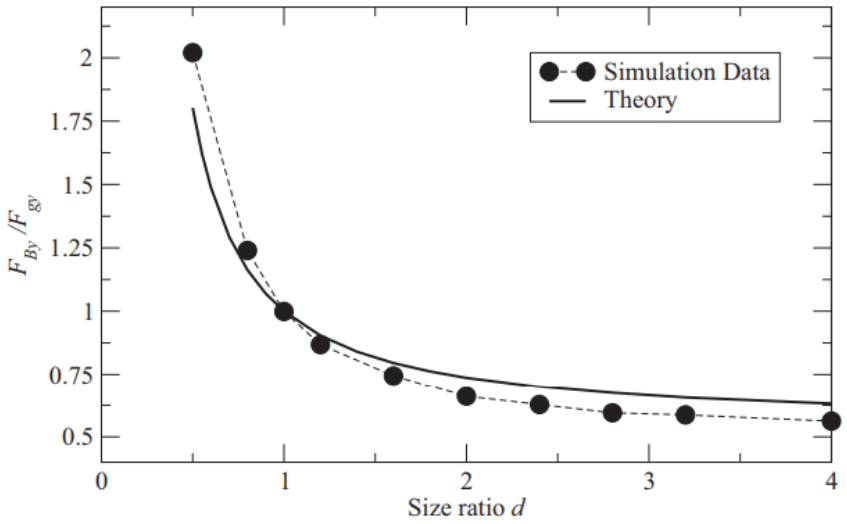

Figure 2.22. The comparison between theoretical calculation from **Alok Kumar et al. (2019)** and simulation by discrete particle method from **van der Vaart K et al. (2018)**

2.8 Aerodynamic drag force

Drag force is a force acting on the object in the opposite direction with the direction of object movement. The drag force is generated when the object is moving through a stationary fluid or the fluid flow pass an object, therefore, this force is a function of

relative velocity between an object and fluid flow. The drag force is caused by two different stress which is shear stress acting in the tangential direction and pressure stress acting in the perpendicular direction on the object surface. Hence, if the distribution of those stress on well-defined objected are known, the drag force would be calculated as in **Equation 2.16.** Similarly**,** the pressure drag means the drag force is resulted by the pressure, while friction drag is the force from skin friction or shear stress on the surface.

$$F_D = \int_A (-Pcos\theta + \tau_w sin\theta) dA \tag{2.16}$$

In general, the pressure drag and skin friction drag force ratio is greatly depended on the object geometry. For the sphere particle, the drag force is mainly coming from the pressure drag force. According to the pressure drag, the difference of pressure at the front region and back region, as shown in **Figure 2.23**, is mainly a cause of pressure drag force **(Snorri Gudmundsson; 2014)**. When the fluid flow passes an object, the pressure at the face against with the flow or front face is normally increased, while the pressure behind an object is relative lower in accordance with the occurring in separation region or turbulent wake.

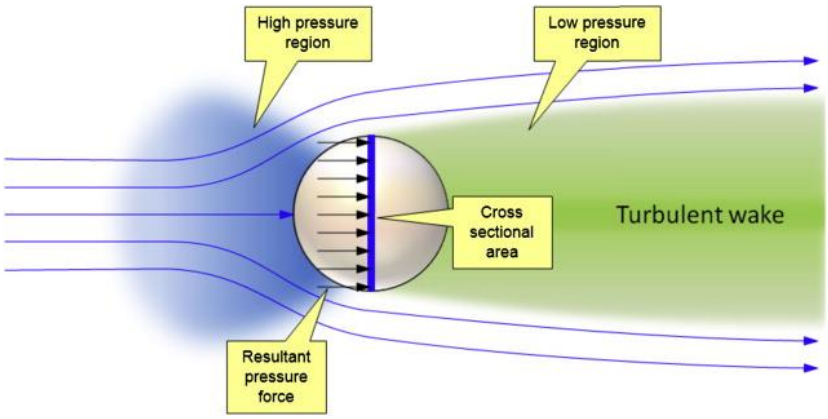

Figure 2.23. The difference in pressure nearby an object **(Snorri Gudmundsson; 2014)**

In general, the integration of an **Equation 2.16** is almost impossible in accordance with the uncertainty in pressure distribution and shear stress on the surface of object. Therefore, the simplification of this issue become an aerodynamic drag force relation as **Equation 2.17**.

$$F_D = \frac{1}{2}\rho v^2 C_D A \quad (2.17)$$

Where, ρ is the density of fluid, v is relative velocity between object and fluid, A is the area of object in the plane perpendicular with flow direction, and C_D is the drag force coefficient.

Nevertheless, the drag force equation of perfect sphere particle sometimes could be reduced to be more simple relation as shown in **Equation 2.18** in accordance with Laminar flow regime. According to the laminar flow, there is no separation region occurring behind the object, and drag force coefficient is predictable as a most basic suggestion of Reynold number, $C_D = \frac{24}{Re}$ **(Boiki V.M., Pivovarov A.A. & Poplavaski S.V.; 2013)**.

$$F_D = 6\pi\eta r v \quad (2.18)$$

Where, η is kinematic viscosity, v is particle velocity, and r is the radius of particle.

2.8.1 Drag force coefficient (Singular particle flow)

The drag force coefficient is the main part of drag force equation and mostly obtained from experiment because it represents for shape of object which is difficult to theoretically explain. As it mentioned earlier, the drag force coefficient is an empirical function obtained from experiment. Normally, the drag force coefficient for perfect sphere is already studied by previous researcher in which drag force coefficient could be predicted well in Laminar flow regime as shown in **Figure 2.24**. However, the drag force coefficient is a non-linear relation when the Reynold number become more than 0.3 **(Perry R.H., Cecil Hamilton Chilton & John Howard Perry; 1973)**.

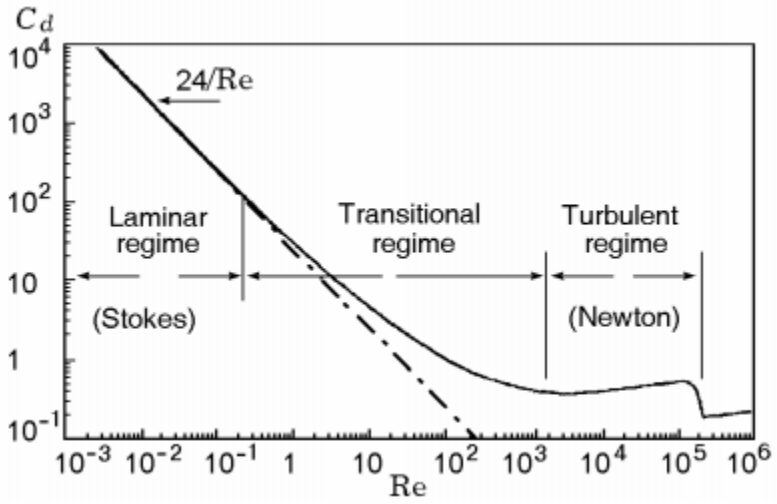

Figure 2.24. The relationship of drag force coefficient and Reynold number for perfect smooth sphere **(Boiki V.M., Pivovarov A.A. & Poplavaski S.V.; 2013)**

In the early days, **Flemmer & Banks (1986)** summarized the prediction function from previous researcher for drag force coefficient as shown in **Table 2.1**. Nevertheless, the prediction function was either not described by single equation or the prediction range is too narrow. Subsequently, **Haider A. & Levenspiel O. (1989)** established the new estimation equation for drag force coefficient for spherical particle. Up to now, their equation had been used for several field and developed for special application as well. **Haider A. & Levenspiel O. (1989)** had referred to the equation from T**urton R. & Levenspiel O. (1986)** and simplified to a simple form as in the **Equation 2.19 (Turton R. & Levenspiel O.; 1986)**. The Gauss-Newton method was used to obtain each coefficient by comparing with experimental data, and the new prediction function was suggested as in the **Equation 2.20**. Furthermore, the comparison between drag force coefficient function and experimental result showed a good correlation as in **Figure 2.25 (Haider A. & Levenspiel O.; 1989)**.

$$C_d = \frac{24}{Re}(1 + ARe^B) + \frac{C}{1+\frac{D}{Re}} \tag{2.19}$$

Table 2.1. The summary of drag force coefficient **(Flemmer R.L.C. & Banks C.L.; 1986)**

Author(s)	Function	Range of applicability
Perry and Chilton (1973)	$C_d = \frac{24}{Re}$	$Re < 0.3$
	$C_d = \frac{18.5}{Re^{0.6}}$	$0.3 < Re < 1000$
	$C_d = 0.44$	$1000 < Re < 200000$
Oseen (1968)	$C_d = \frac{24}{Re}\left(1 + \frac{3}{16}Re\right)$	$Re < 1$
Massey (1968)	$C_d = \frac{24}{Re}\left(1 + \frac{3}{16}Re\right)^{\frac{1}{2}}$	$Re \leq 100$
Schiller and Nauman (1933)	$C_d = \frac{24}{Re} + \frac{3.6}{Re^{0.313}}$	$0.1 < Re < 1000$
Fouda and Capes (1976)	$Y = \sum_{n=0}^{5} a_n X^n$ Where, (1) $Y = log_{10}(Pd), X = log_{10}\left(\frac{u_t}{Q}\right)$ $Pd = \sqrt[3]{C_d Re^2}, \frac{u_t}{Q} = \sqrt{\frac{Re}{C_d}}$ $a_0 = -1.37323$ $a_1 = 2.06962$ $a_2 = -0.453219$ $a_3 = -0.334612 \times 10^{-1}$ $a_4 = -0.745901 \times 10^{-2}$	$1 \times 10^{-2} < Re < 1 \times 10^{-5}$

	$a_5 = -0.249580 \times 10^{-2}$ (2) $Y = log_{10}\left(\frac{u_t}{Q}\right), X = log_{10}(Pd)$ $a_0 = 0.785724$ $a_1 = 0.684342$ $a_2 = 0.168457$ $a_3 = 0.103834$ $a_4 = 0.20901 \times 10^{-1}$ $a_5 = 0.57664 \times 10^{-2}$	
Al-Salim & Geldart (1969)	$\frac{579}{Re^2} = \frac{3.318 \times 10^5}{(C_d Re^2)^2} + \frac{2.954 \times 10^4}{(C_d Re^2)^{1.5928}} + \left[\frac{9.479 \times 10^{11}}{(C_d Re^2)^{4.1949}} + \frac{8.440 \times 10^{10}}{(C_d Re^2)^{3.7877}}\right]^{0.313}$	$0.1 < Re < 1000$
Flemmer and Banks (1986)	$C_d = \frac{24}{Re} 10^E$ Where, $E = 0.261 Re^{0.369} - 0.105 Re^{0.431} - \frac{0.124}{1 + (log_{10} Re)^2}$	$Re < 3 \times 10^5$

$$C_d = \frac{24}{Re}(1 + 0.1806 Re^{0.6459}) + \frac{0.4251}{1 + \frac{6880.95}{Re}} \quad (2.20)$$

Where, Re is Reynold number. In general, the Reynold number could be described for

two main topics; 1. The fluid flow pass an object, and 2. The fluid flow in the pipe. According to erosion issue, the mechanism is considered as the flow passing through the particle, therefore, the Reynold number is calculated as follow **Equation 2.21**.

$$Re = \frac{\rho_f |w| d}{\mu_f} \tag{2.21}$$

Where, ρ_f is the fluid density, w is relative velocity between fluid and particle, d is the particle diameter, and μ_f is dynamic viscosity of fluid

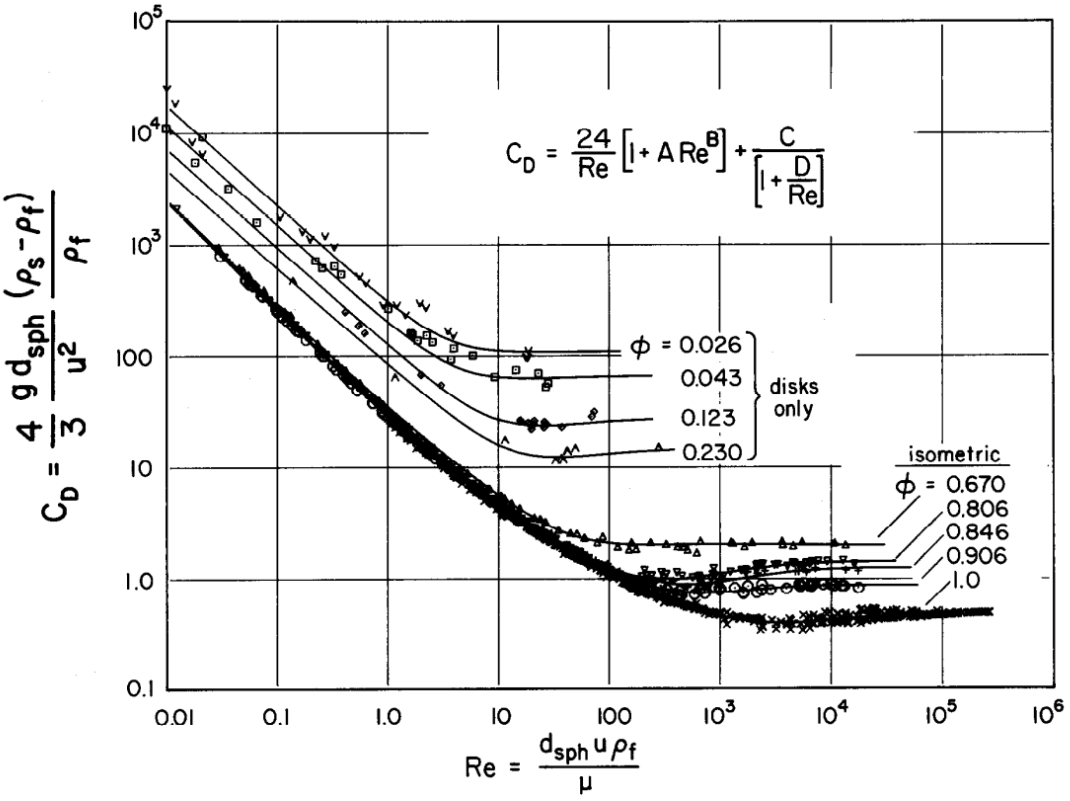

Figure 2.25. The comparison of drag force coefficient between empirical solution and experimental data **(Haider A. & Levenspiel O.; 1989)**

In order to investigate on an erosion, the study on drag force coefficient on particle with irregular shape or non-spherical shape is necessary. At the beginning, the concept to define the sphericity, ψ, of particle was suggested as **Equation 2.22 (Wadell H.; 1934)**. **Haider A. & Levenspiel O. (1989)** suggested the solution to estimate drag force coefficient for non-spherical particle as well by with the sphericity concept **from Wadell H. (1943)**.

$$\frac{s}{\mathcal{S}} = \psi \tag{2.22}$$

Where, s is the surface area of perfect sphere in which the volume is same as the target particle, and $\mathcal{S}$ is the actual surface area of particle.

Similarly, **Haider A. & Levenspiel O. (1989)** tried to fit the empirical equation with the experimental data which was composed of four types of non-spherical particle; 1. Cube octahedrons ($\psi = 0.906$), 2. Octahedrons ($\psi = 0.846$), 3. Cubes ($\psi = 0.806$) and, 4. Tetrahedrons ($\psi = 0.670$). The equation of drag force coefficient for non-spherical particle was suggested as a function of sphericity and Reynold number as in **Equation 2.23**. The comparison of analytical solution and experimental data was compared as well as the spherical particle in **Figure 2.25**.

$$C_D = \frac{24}{Re}\left[1 + e^{\left(2.3288 - 6.4581\Phi + 2.4486\Phi^2\right)}\right] Re^{\left(0.0964 + 0.5565\Phi\right)} + \frac{Re \times e^{\left(4.905 - 13.8944\Phi + 18.4222\Phi^2 - 10.2599\Phi^3\right)}}{Re + e^{\left(1.4681 + 12.2584\Phi - 20.7322\Phi^2 + 15.8855\Phi^3\right)}} \tag{2.23}$$

Recently, several developments in drag force coefficient for non-spherical particle was showing a better correlation with the experimental result. For an example, the shape factor, Ψ, was used in the calculation of drag coefficient instead of sphericity, Φ **(Dellino P., Mele D., Bonasia R., Braia G., La Vollpe L. & Sulpizio R.; 2005)**. Consequently, the solution of drag force coefficient prediction from Haider A. & Levenspiel O. (1989) was improved by paying more attention on the natural material or irregular shape **(Dioguardi F. Mele D. & Dellino P.; 2018)**. The prediction equation is shown as **Equation 2.24**, which is the function of Reynold number and three shape factor function.

$$C_D = \frac{24}{Re} f_1(\Psi) + \frac{24}{Re} f_2(\Psi)\left(0.1806 Re^{0.6459}\right) + \frac{0.4251}{1 + \frac{6880.95}{Re} f_3(\Psi)} \tag{2.24}$$

Where, Ψ is shape factor, and X is ratio between maximum projection perimeter, P_{mp}, and the perimeter of circle which has the same area with maximum projection area, P_c.

$\Psi = \frac{\Phi}{X}$, and $X = \frac{P_{mp}}{P_c}$

$$f_1(\Psi) = \left(\frac{1 - \Psi}{Re} + 1\right)^{0.25}$$

$f_2(\Psi) = \Psi^{-Re^{0.08}}$

$f_3(\Psi) = \Psi^{5.05}$

2.8.2 Secondary coefficient on drags force (multi-particle flow)

The drag force coefficient which was mentioned earlier represent for a single particle flow in the system, while the erosion is normally combined with a plenty of particles. Therefore, the understanding in relation between particle fraction and drag force coefficient is necessary.

Considering a particle flow in the solid multiparticle system, the drag force coefficient from single particle must be modified for considering the multiparticle system. Previous research had found that there is influence on increment of drag force coefficient at high volume fraction **(Barnea E. & Mizrahi J.; 1973)**. The general form widely used in several purpose of multiparticle flow is shown as **Equation 2.25**.

$$C_d = f(\alpha)C_{d0} \tag{2.25}$$

Where, C_d is the drag force for multiparticle flow, C_{d0} is the drag force for single particle flow, and $f(\alpha)$ is the function of adjustment which is normally a function of particle fraction, α.

There are many suggestions on particle fraction function, $f(\alpha)$, on difference purposes and it could be expressed in the form as shown in **Equation 2.26 (Rusche H. & Issa R.; 2000)**.

$$f(\alpha) = e^{(K_1\alpha)} + \alpha^{K_2} \tag{2.26}$$

Where, K_1 and K_2 are the constant parameters obtained from experimental test, Rusche H. & Issa R. (2000) recommend the value of these coefficient as shown in **Table 2.2**.

Table 2.2. The coefficient for particle fraction function

	Particles	Droplets	Bubbles
K_1	2.680	2.100	3.640
K_2	0.430	0.249	0.864

2.9 Tortuosity

Tortuosity, T, means the property of curve or twisted path, the simplest way to describe Tortuosity is the ratio between actual path and the shortest distance between two ends as in the **Equation 2.27**.

$$T = \frac{C}{L} \tag{2.27}$$

Where, C is the actual distance between starting point and end point, while L is the shortest length between those two points.

However, the estimation of the tortuosity inside porous media was not simple like **Equation 2.27** but normally is a function of porosity, ϕ. In general, tortuosity relation is an empirical solution which mainly obtained either numerical simulation or experimental test. There are several function forms to estimate a tortuosity from porosity which was summarized and shown in **Equation 2.28-2.31 (Matyka M., Khalili A. & Koza z.; 2008)**.

$$T(\phi) = \phi^{-p} \tag{2.28}$$

$$T(\phi) = 1 - pln(\phi) \tag{2.29}$$

$$T(\phi) = 1 + p(1 - \phi) \tag{2.30}$$

$$T(\phi) = [1 + p(1 - \phi)]^2 \tag{2.31}$$

Chapter 3 The soil-water coupling analysis of vertical shaft in shallow groundwater area

3.1 Introduction

According to the high demand of underground infrastructure, especially in tunneling construction, vertical shaft structure is one of the components of those structure which normally stands for ventilation system even or emergency exist.

In general, the shaft construction in urban area sometimes is facing with shallow groundwater level, therefore, the simulation which could foresee the phenomenon is necessary. Nevertheless, most of the commercial software has a potential to perform a soil-water coupling simulation to show the general mechanical behavior.

In this chapter, the soil-water coupling simulation is conducted with FLAC3D which is a Finite Difference method to elucidate on several issues on shaft construction. According to the soil-water coupling simulation, this chapter can mainly focus on the mechanical behavior of cylindrical shaft and surrounding soil during construction process. Furthermore, the simulation in this chapter also tried to mimic the real construction procedure by adding the dewatering process into the simulation as well.

3.2 Background

In this chapter, the numerical analysis ware conducted to consider as 2 mains objective which are fundamental behavior of circular shaft and excavation stability. In order to construct vertical shaft in high groundwater level, dewatering system must be performed for constructing shaft. After shaft installation, water inside vertical shaft will be dewatered for preparing excavation area. Therefore, the dewatering work and excavation work will be performed, alternatively. First section, analysis would show the basic behavior as lateral earth pressure acting on circular shaft and inner-displacement. Second, the analysis aims for considering excavation stability which is quite important for safety during construction process.

In addition, the size of shaft is decided based on the report from previous study which was showing an average size of shaft construction **(Muramatus & Abe; 1996)**.

3.3 Numerical method

In this chapter, Explicit Finite Different method (FDM) has been used which operated by FLAC3D. The Modified Cam Clay model, elasto-plastic material, and elastic model were chosen for describing the soil and structure behavior respectively. Additionally, the soil-water coupling analysis were performed for including high groundwater level in the model.

3.3.1 The numerical formation in FLAC3D and constitutive model

The simulation program for using in this chapter (FLAC3D) was established based on an Explicit Finite Different method which using a forward different at time and a second-order central difference of the space derivative. This research has been performed by Finite Different Method, which could provide initiation of large deformation in simulation model, for investigating on deep circular vertical shaft behavior.

3.3.1.1 Stress-strain calculation

The discretization of the volume under study is done into hexahedral zone. According to the Explicit Finite Different method, the calculation sequence is shown below.

1) New strain rates are derived from nodal velocities.

New strain rates would be calculated by velocities, therefore, the equation of the first strain rate invariant, ξ^z, is shown as **Equation 3.1**.

$$\xi^z = \frac{\sum_{k=1}^{k_t} \xi^{[k]} V^{[k]}}{\sum_{k=1}^{k_t} V^{[k]}} \tag{3.1}$$

2) The new stress would be calculated through constitutive equation by using previous stress and strain rates.

Hereafter, the constitutive equations are used in their incremental form, H_{ij}^*, to calculate stress increments for each tetrahedron in zone as in **Equation 3.2**.

$$\Delta\sigma_{ij} = H_{ij}^{*}(\sigma_{ij}, \Delta\varepsilon_{ij}) + \Delta\sigma_{ij}^{c} \tag{3.2}$$

and $\Delta\varepsilon_{ij}$ is computed to form as in the **Equation 3.3**.

$$\Delta\varepsilon_{ij} = -\frac{\Delta t}{6V}\Sigma_{l=4}^{4}(v_i^l n_j^{(l)} + v_j^l n_i^{(l)})S^{(l)} \tag{3.3}$$

Then, the new stress values are derived by additional stress increments as in **Equation 3.4**. Also, for the hexahedral mesh, the stress could be calculated by **Equation 3.5**.

$$\sigma_{ij}^{(l)} = s_{ij}^{[l]} + \sigma^{z}\delta_{ij} \tag{3.4}$$

$$\xi^{z} = \frac{\sum_{k=1}^{k_t}\xi^{[k]}V^{[k]}}{\sum_{k=1}^{k_t}V^{[k]}} \tag{3.5}$$

3) The new nodal velocities and displacements are calculated by stresses and forces based on the equation of motion

Finally, the new nodal velocity and displacement would be calculated by using the **Equation 3.6** and **Equation 3.7**, respectively.

$$v_i^{<l>}(t + \frac{\Delta t}{2}) = v_i^{<l>}(t - \frac{\Delta t}{2}) + \frac{\Delta t}{M^{<l>}}(F_i^{<l>} + F_i^{<l>}) \tag{3.6}$$

$$u_i^{<l>}(t + \frac{\Delta t}{2}) = u_i^{<l>}(t) + \Delta t u_i^{<l>}(t + \frac{\Delta t}{2}) \tag{3.7}$$

According to this analysis model (Deep circular vertical shaft) has used 2 constitutive models which are Elastic isotropic model and Modified Cam-Clay model. In case of including groundwater, soil-water coupling analysis has been used.

3.3.1.2 Elastic isotopic model

The elastic isotropic model can represent as simple material behavior which used for vertical shaft structure in the model. For this model, isotropic model, could be used as representative of homogeneous or continuous material.

In elastic isotropic model the strain and stress generation are associated by Hook law as shown in **Equation 3.8**.

$$\Delta\sigma_{ij} = 2G\Delta\varepsilon_{ij} + \alpha_2\Delta\varepsilon_{kk}\delta_{ij} \tag{3.8}$$

where α_2 is a material constant based on the relationship with Bulk modulus, *K*, and shear modulus, *G*, as following in **Equation 3.9**.

$$\alpha_2 = K - \frac{2}{3}G \tag{3.9}$$

Therefore, the new stress value could be calculated by the **Equation 3.10**.

$$\sigma_{ij}^{N} = \sigma_{ij} + \Delta\sigma_{ij} \tag{3.10}$$

3.3.1.3 Modified Cam-Clay model

Modified Cam-Clay theory was developed by Roscoe and Burland (1968) and Wood (1990). Modified Cam-Clay is an incremental hardening/softening elastoplastic model which governed by plastic volumetric strain.

Basically, Modified Cam-clay model is specified by performing the definition of mean effective stress, *p*, and deviatoric stress, *q*, as following in **Equation 3.11** and **Equation 3.12**.

$$p = -\frac{1}{3}\sigma_{ii} \tag{3.11}$$

$$q = \sqrt{3J_2} \tag{3.12}$$

Where J_2 is the second invariant of effective deviatoric stress which calculated by using **Equation 3.12**.

$$J_2 = \frac{1}{2}S_{ij}S_{ij} \tag{3.13}$$

The incremental strain variables associated with *p* and *q* are the volumetric strain increment, $\Delta\varepsilon_p$, and shear strain increment, $\Delta\varepsilon_q$. **Equation 3.14** and **Equation 3.15** shows product of these variables.

$$\Delta\varepsilon_p = -\Delta\varepsilon_{ii} \tag{3.14}$$

$$\Delta\varepsilon_q = \frac{2}{3}\sqrt{3\Delta J_2^{/}} \tag{3.15}$$

where $\Delta J_2^{/}$ is second invariant of incremental deviatoric strain tensor $\Delta[e]$ which could be expressed as **Equation 3.16**.

$$\Delta J_2^{/} = \frac{1}{2}\Delta e_{ij}\Delta e_{ij} \tag{3.16}$$

The generalized strain, for both of volumetric and shear strain, can be divided in the 2 components; elastic and plastic section shown in **Equation 3.17** and **Equation 3.18**.

$$\Delta\varepsilon_p = \Delta\varepsilon_p^e + \Delta\varepsilon_p^p \tag{3.17}$$

$$\Delta\varepsilon_q = \Delta\varepsilon_q^e + \Delta\varepsilon_q^p \tag{3.18}$$

The specific volume is for an evolution parameter defined in **Equation 3.19**.

$$\Delta\varepsilon_p = \frac{V}{V_S} \tag{3.19}$$

where V_S is the volume of solid particles, assumed incompressible, contained in a volume, V, of soil. The incremental relation between volumetric strain, ε_p, and specific volume has the form as in **Equation 3.20**.

$$\Delta\varepsilon_p = -\frac{\Delta v}{v} \tag{3.20}$$

Therefore, the new specific volume, v^N, could be calculated as **Equation 3.21**

$$v^N = v(1-\Delta\varepsilon_p) \tag{3.21}$$

The stress generation, mean effective stress and deviatoric stress, is defined by using Hooke's law as following in **Equation 3.22** and **Equation 3.23**.

$$\Delta p = K\Delta\varepsilon_p^e \tag{3.22}$$

$$\Delta q = 3G\Delta\varepsilon_q^e \tag{3.23}$$

where $\Delta q = \sqrt{3\Delta J_2}$, and ΔJ_2 stands for the second invariant of the incremental deviatoric-stress tensor which shown in **Equation 3.24**.

$$\Delta J_2 = \frac{1}{2}\Delta s_{ij}\Delta s_{ij} \tag{3.24}$$

In Modified Cam-clay model tangential bulk modulus, K, will be recalculated every single step, to reflect a non-linear law derived experimentally from isotropic compression test, which is used in volumetric strain equation. The result of typical isotropic compression test is shown as in **Figure 3.1**.

(Note: K is the tangential bulk modulus which different from elastic bulk modulus, nonlinear function of mean effective stress).

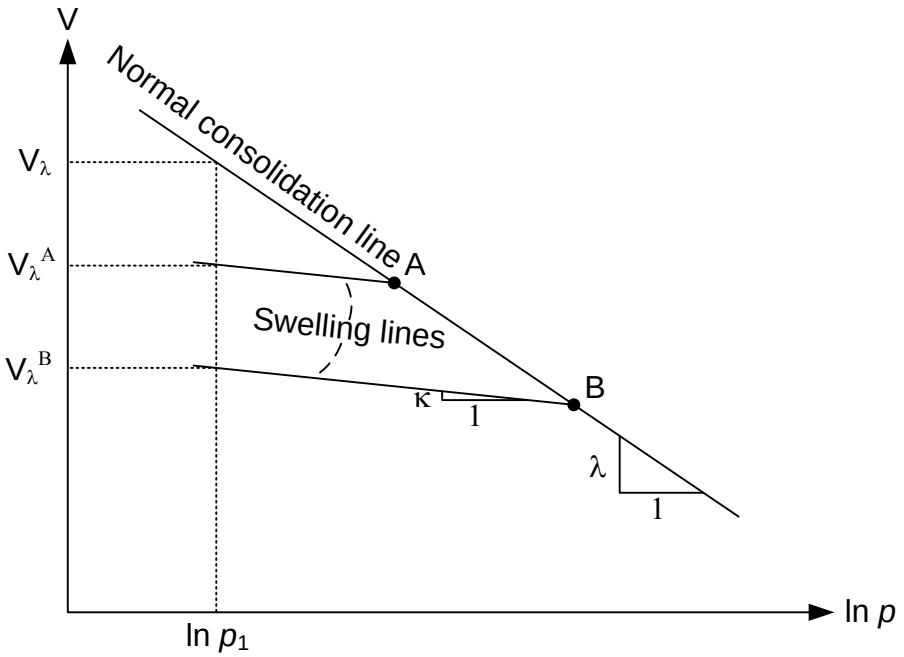

Figure 3.1 Normal consolidation line and unloading-reloading line for isotropic compression test.

The normal consolidation pressure, p, increase, the specific volume, v, will be decreasing. The represent point along normal consolidation line could be expressed as **Equation 3.25**.

$$v = v_\lambda - \lambda \ln \frac{p}{p_1} \tag{3.25}$$

where λ and v_λ, specific volume at reference point. these are material parameters, and p_1 is the pressure at reference point. These parameters and pressure, are used for defining normal consolidation line.

As in **Figure 3.1**, the swelling line, which connected with normal consolidation line, is the path of unloading and reloading. This path could be called as swelling line, controlled by slope κ as following as in **Equation 3.26**.

$$v = v_\kappa - \kappa \ln \frac{p}{p_1} \tag{3.26}$$

where κ is material constant, and the value of v_κ for particular-line depends on the location of the point on the normal consolidation line from which unloading was performed.

After unloading, the recovering specific volume, Δv^e, will be occurred as expressing in **Equation 3.27**.

$$\Delta v^e = -\kappa \frac{\Delta p}{p} \tag{3.27}$$

After division of both members by v, and using **Equation 3.18** that will be obtaining **Equation 3.28**.

$$\Delta p = \frac{vp}{\kappa} \Delta \varepsilon_p^e \tag{3.28}$$

In Modified cam-clay, it is performed with the assumption, that the change of mean effective stress influence on elastic volumetric strain. According to the expansion of soil, the change of bulk modulus with changing in mean effective stress has been suggested as in **Equation 3.29**.

$$K = \frac{vp}{\kappa} \tag{3.29}$$

According to **Figure 3.2**, the increment of mean effective stress could be moving from point A to A', which affected by increase of pre-consolidation pressure, p_c, and consolidation volume, $v_c^{A'}$. The increment of plastic volume change, Δv^p, is measured by using the distance between swelling lines which giving relation as in **Equation 3.30**.

$$\Delta v^p = -(\lambda - \kappa) \frac{\Delta p_c}{p_c} \tag{3.30}$$

After dividing the **Equation 3.30** by v, we will obtain **Equation 3.31**.

$$\Delta \varepsilon_p^p = \frac{\lambda - \kappa}{v} \frac{\Delta p_c}{p_c} \tag{3.31}$$

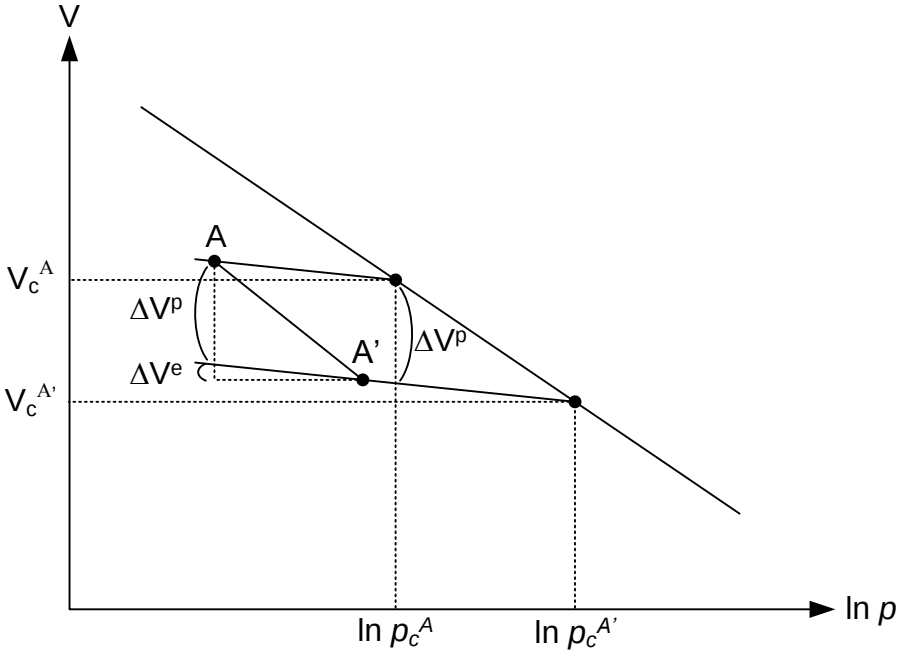

Figure 3.2 Plastic volumetric change due to incremental pre-consolidation pressure

The yield function of modified cam-clay, corresponding to the pre-consolidation pressure, might be expressed as function in **Equation 3.32**.

$$f(q,p) = q^2 + M^2 p(p - p_c) \tag{3.32}$$

where M is slope of critical state line which is material constant. The yield condition is $f(q,p) = 0$, that represented by ellipse with horizontal axis p_c and vertical axis Mp_c in (q,p) plane as in **Figure 3.3**.

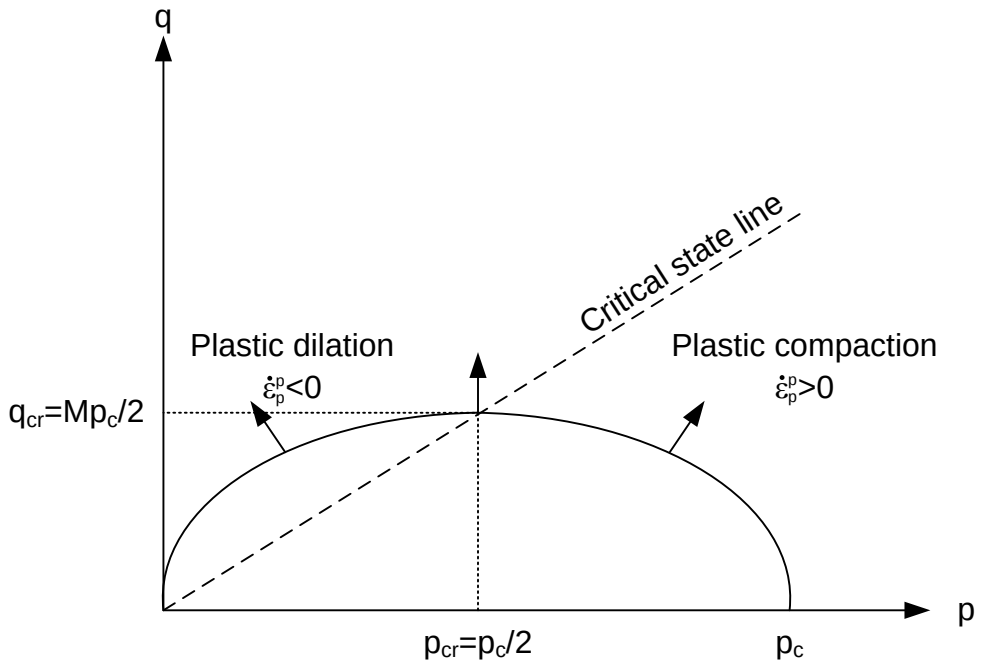

Figure 3.3 Cam-clay failure criteria

The potential function g corresponds to an associated flow rule, and we have **Equation 3.33**.

$$g = q^2 + M^2 p(p - p_c) \tag{3.33}$$

The flow rule is used to express plastic as in **Equation 3.34** and **Equation 3.35**.

$$\Delta\varepsilon_p^p = \lambda^v \frac{\partial g}{\partial p} \tag{3.34}$$

$$\Delta\varepsilon_q^p = \lambda^v \frac{\partial g}{\partial q} \tag{3.35}$$

where λ^v is plastic multiplier whose magnitude remains to be defined. After differentiating the **Equation 3.34** and **Equation 3.35** the product will be **Equation 3.36** and **Equation 3.37**.

$$\Delta\varepsilon_p^p = \lambda^v c_a \tag{3.36}$$

$$\Delta\varepsilon_q^p = \lambda^v c_b \tag{3.37}$$

Where the c_a and c_b could be calculated by using **Equation 3.38** and **Equation 3.39**.

$$c_a = M^2(2p - p_c) \tag{3.38}$$

$$c_b = 2q \tag{3.39}$$

The elastic strain increment, which caused by mean effective and deviatoric stress increment, could be expressed as **Equation 3.40** and **Equation 3.41**.

$$\Delta p = K(\Delta\varepsilon_p - \lambda^v c_a) \tag{3.40}$$

$$\Delta q = 3G(\Delta\varepsilon_q - \lambda^v c_b) \tag{3.41}$$

Therefore, the stress in next step will be updated by using the **Equation 3.42** and **Equation 3.43** for mean effective stress and deviatoric stress respectively (N: new stress and O: old stress).

$$p^N = p^O + \Delta p \tag{3.42}$$

$$q^N = q^O + \Delta q \tag{3.43}$$

Substitution of **Equation 3.40** and **Equation 3.41** we will obtain **Equation 3.44 and Equation 3.45.**

$$p^N = p^I - \lambda^v K c_a \tag{3.44}$$

$$q^N = q^I - \lambda^v 3G c_b \tag{3.45}$$

where the superscript *I* is used to represent the elastic guess, obtained from summation of old stress and elastic increment as in **Equation 3.46** and **Equation 3.47**.

$$p^I = p^O - K\Delta\varepsilon_p \tag{3.46}$$

$$q^I = q^O - 3G\Delta\varepsilon_q \tag{3.47}$$

Therefore, the plastic multiplier, λ^v, might be defined by using the new stress that located on the yield surface. Substitution of p^N and q^N for p and q in the f(q,p)=0. Then, we will get **Equation 3.48**.

$$a(\lambda^v)^2 + b\lambda^v + c = 0 \tag{3.48}$$

where the a, b and c are expressed by **Equation 3.49**, **Equation 3.50**, and **Equation 3.51**, respectively.

$$a = (MKc_a)^2 + (3Gc_b)^2 \tag{3.49}$$

$$b = -[Kc_a c_a^I + 3Gc_b c_b^I] \tag{3.50}$$

$$c = f(q^I, p^I) \tag{3.51}$$

Additionally, the size of yield surface depends on the consolidation pressure, which mean the plastic volumetric strain influence on the change of consolidation pressure as in **Equation 3.52**.

$$p_c^N = p_c(1+\Delta\varepsilon_p^p \frac{\nu}{\lambda-\kappa}) \tag{3.52}$$

3.3.1.4 Fluid-mechanical interaction

The governing differential equation of fluid section is described as following theory:

3.3.1.4.1 Transport law

The fluid transport law is described by Darcy's law as following in **Equation 3.53**.

$$q_i = -k_{il}\hat{k}(s)[p - p_f x_j g_j]_{,l} \tag{3.53}$$

where q_i is the specific discharge vector, p is fluid pore pressure, k is the tensor of absolute mobility coefficients, $\hat{k}(s)$ is the relative mobility coefficient which depending on saturation, s, p_f is fluid density, and g_i, i = 1,2,3 are the three components of gravity vector.

3.3.1.4.2 Balance law

For small deformations, the fluid mass balance may be expressed as **Equation 3.54**.

$$q_{i,i} + q_v = \frac{\partial\zeta}{\partial t} \tag{3.54}$$

where q_v is the volumetric fluid source intensity in [1/sec], and ζ is the variation of fluid content or variation of fluid volume per unit volume of porous material due to diffusive fluid mass transport, as introduced by Biot (1956).

3.3.1.4.3 Constitutive law

The changes in variation of fluid content are related to changes in pore pressure, p, saturation, s, mechanical volumetric strain, ε which could be formulated as in **Equation 3.55**.

$$\frac{1}{M}\frac{\partial p}{\partial t} + \frac{n}{s}\frac{\partial s}{\partial t} = \frac{1}{s}\frac{\partial\zeta}{\partial t} - \alpha\frac{\partial\varepsilon}{\partial t} \tag{3.55}$$

where M is Biot modulus [N/m^2], n is porosity, α is Biot coefficient.

Additionally, the permeability of fluid flow is controlled by the **Equation 3.56** which related to the saturation of soil.

$$\hat{k}(s) = s^2(3-2s) \tag{3.56}$$

3.4 The simulation procedure

3.4.1 Mesh generation and boundary condition

After trying to calculate the circular vertical shaft with excavation process, the effective zone of the soil, which stress has been changed, is about 3 times of diameter. Therefore, we decided to use boundary as 100 m wide. Also, the depth was decided to be 300 m because the influence of changing vertical stress from excavation process would be affecting on soil behavior in vertical direction (at soil foundation).

In this model was combined for 3 main types of mesh which are cylindrical, radial cylindrical and cylindrical shell mesh. The circular shaft is built up by cylindrical shell mesh (2,304 mesh) and the soil is combined from cylindrical mesh and cylindrical mesh (68,544 mesh). The boundary is shown as in **Figure 3.5** which fixing at the 4 sides in normal direction and fix vertical direction at model base.

3.4.2 Excavation with dewatering simulation

According to the analysis of excavation in vertical shaft undergoing high groundwater level, dewatering system should be included in the analysis. Firstly, before performing excavation, dewatered soil inside vertical shaft would be done by setting the soil permeability as zero and initialized pore pressure is zero as well as in **Figure 3.4**. In addition, the depth between excavation base and water level will be restrained as constant length about 20 m. Then, after finishing dewatering process, the excavation process which same process as in the previous analysis section (in dry geo-material), will be performed. Therefore, the dewatering process would be 4 steps (excavation process: 4 steps).

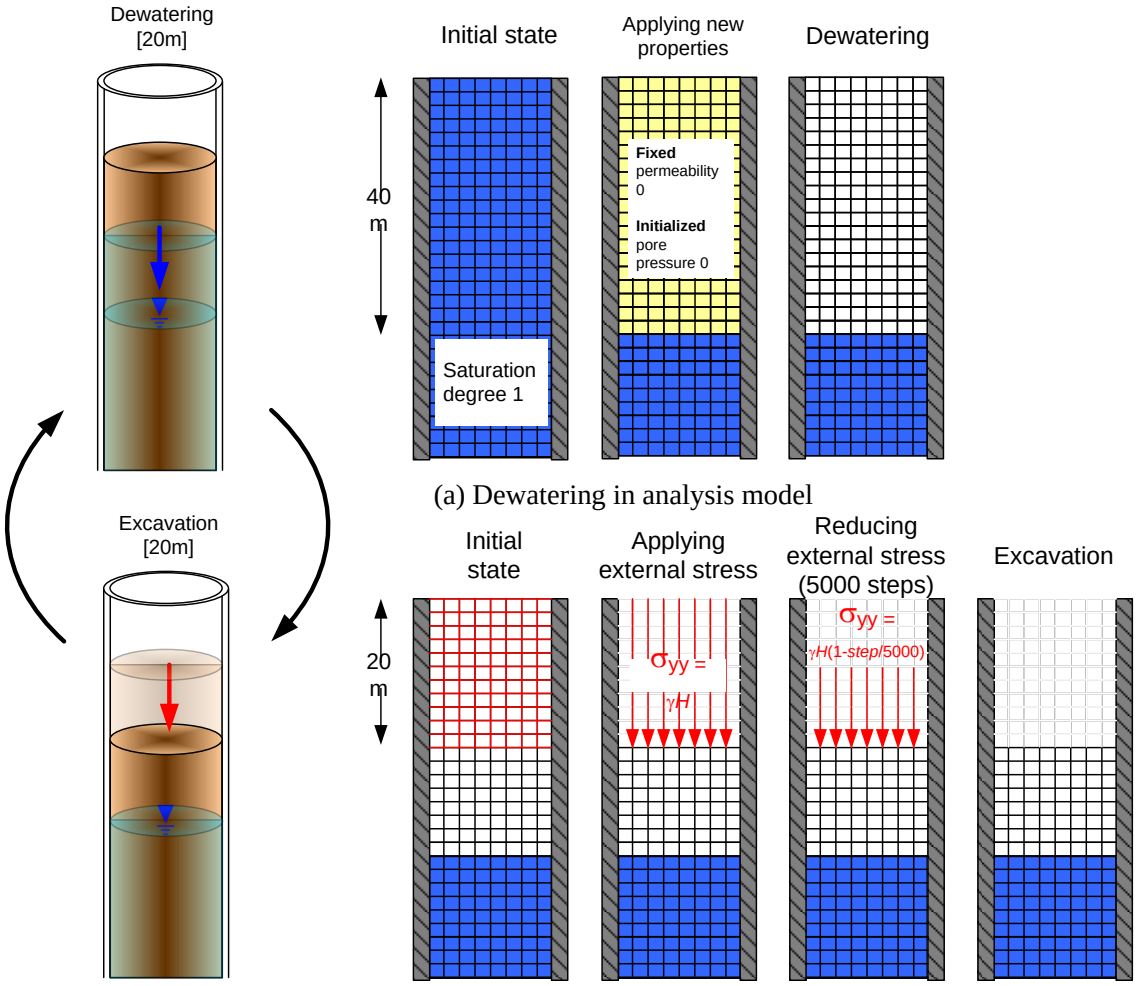

(a) Dewatering in analysis model

(b) Excavation in analysis model

Figure 3.4 Analysis procedure for dewatering and excavation process

3.5 The fundamental behavior of circular vertical shaft in high groundwater level (soft and rigid shaft)

This section would show the fundamental behavior of circular vertical shaft during excavation process in high groundwater level. The analysis model and boundary condition of this analysis has shown in **Figure 3.5**, which pore pressure at base and 4 sides of model was fixed. According to the behavior of soft and rigid circular vertical shaft in dry-geo-material are quite different. Therefore, this section will be the comparison of the behavior between 2 stiffness of circular vertical shaft which are 30 GPa (rigid vertical shaft) and 100 MPa (soft vertical shaft). In addition, parameters were used in this

analysis showing in **Table 2.1** and **Table 2.2** for mechanical parameter and fluid phrase respectively.

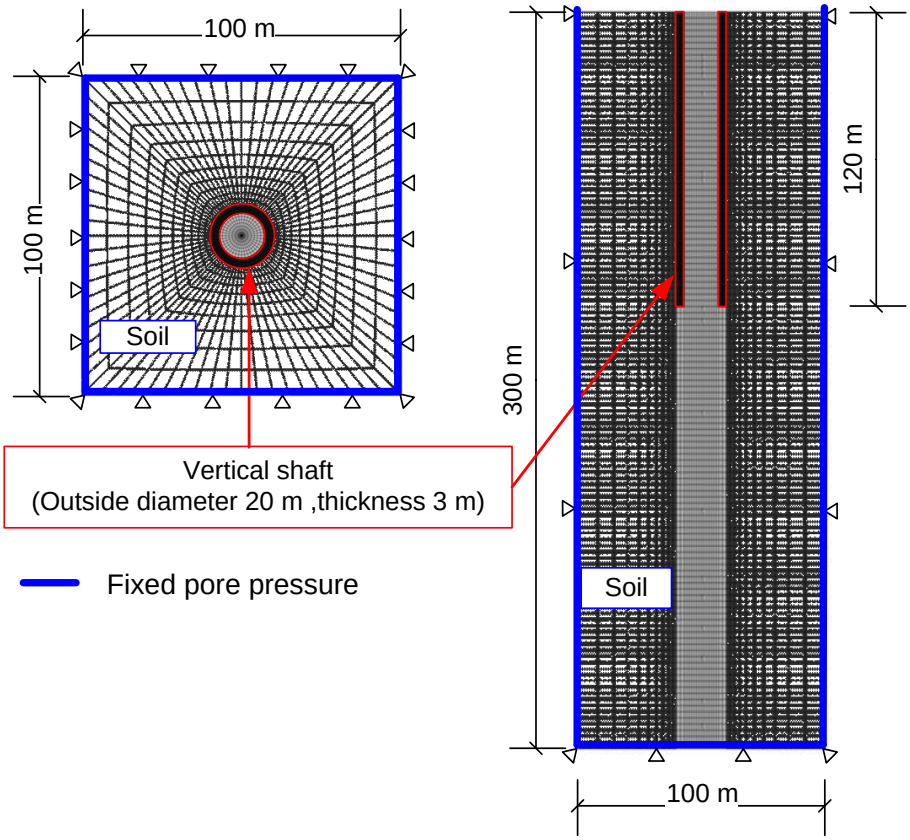

Figure 3.5 Boundary condition of soil-water coupling analysis for circular vertical shaft

Table 3.1. Mechanical parameter for soil and vertical shaft

Material	Model	Parameter	Value
Soil: Toyoura sand	Modified cam clay model	K_{max} (Maximum elastic bulk modulus)	$5.0x10^9$ Pa
		Density	1.6 g/cm^3
		K (Slope of elastic swelling line)	0.0045
		l (Slope of normal consolidation)	0.07
		Poisson's ratio	0.33
		M (Frictional constant)	1.28
		OCR	2.0
		P_1 (Specific pressure at reference point)	$98.0x10^3$ Pa
		V_1 (Specific volume at reference point)	2.10
Vertical shaft: Soil Mixing wall	Elastic model	E (Young's modulus)	~ Pa
		Poisson's ratio	0.33
		Density	2.2 g/cm^3

Table 3.2. Fluid phrase parameters

Model	Parameter	Value
Fluid (soil-water coupling)	Density	1.0 g/cm^3
	Fluid modulus	$2x10^9$ Pa
	Fluid tension limit	$-5x10^5$ Pa
	Permeability (*k*)	$1x10^{-4}$ m/s
	Porosity (*n*)	0.5

3.5.1 Results of fundamental behavior of excavation process in high groundwater level

The results were shown as each step of construction process (8 steps of analysis process). **Figure 3.6(a)** shows after 1st step of dewatering (dewatering: 40 m) the lateral stress are similar but in soft vertical shaft is higher than rigid vertical shaft. When excavation has been performed, the lateral earth pressure above excavation area trend to be decreasing.

Especially in soft vertical shaft, after excavation the lateral earth pressure, above excavation base, is lower than rigid vertical shaft as following in **Figure 3.6(b), 3.6(d), 3.6(f) and 3.6(h)**. Conversely, the dewatering process is not providing huge impact on lateral earth pressure and inner-displacement. Nevertheless, lateral earth pressure below excavation base of soft vertical shaft is still higher than rigid vertical shaft. When focusing on comparison of active earth pressure line with lateral earth pressure, the result would be showing, that the reduction of lateral earth pressure from excavation process is leading to be lower than active earth pressure (both rigid and soft vertical shaft).

3.5.2 Discussion of fundamental behavior of excavation process in high groundwater level

There is some unfamiliar behavior of the lateral earth pressure distribution along circular vertical shaft which is the lateral earth pressure at soft vertical shaft is higher than rigid vertical shaft below excavation surface. As in the result, the lateral earth pressure along both of rigid and soft shaft has been differed since wall installation was done. Therefore, the lower stiffness of vertical shaft could be encountering with some structure expanding caused by density of soil mixing wall (SMW) zone will be changed after wall installation command. Then, the radial stress, which might be occurred during wall installation, will produce additional radial stress. The inner-displacement and lateral earth pressure distribution pattern are slightly different from the consequences of circular shaft in dry geo-material. The large displacement is spontaneously occurring in flexible vertical shaft due to its flexibility, hence, the reduction of earth pressure is naturally greater than rigid vertical shaft. In addition, the earth pressure is always changed due to the different depth of excavation, the reduction of earth pressure is basically found above excavation surface. Similarly, the displacement is gradually increasing from the top of vertical shaft to the surface of excavation area. However, the maximum displacement is mostly located above excavation area about 5 to 10 m.

The earth pressure acting on cylindrical shaft as shown in **Figure 3.6** was slightly below active earth pressure from Rankine's theory. Therefore, the development of earth pressure along cylindrical shaft must be associated by arching effect due to its geometry. The characteristic of arching effect is that the radial stress will decrease when the

tangential stress is increasing. Therefore, the stress history of surrounding soil in both tangential and radial direction were observed during numerical calculation in the case of flexible shaft to confirm that the earth pressure along cylindrical shaft is associated by arching or ring effect. **Figure 3.7** shows the soil stress generation at 8 specific location along cylindrical shaft surface. The excavation inside cylindrical shaft basically induces the inner displacement of cylindrical shaft wall by removing pressure at passive side. According to the results as shown in **Figure 3.7**, the tangential stress tends to increase after each step of excavations while the radial stress is decreasing. Therefore, this kind of behavior can confirm that the arching effect is forming along cylindrical shaft during excavation process.

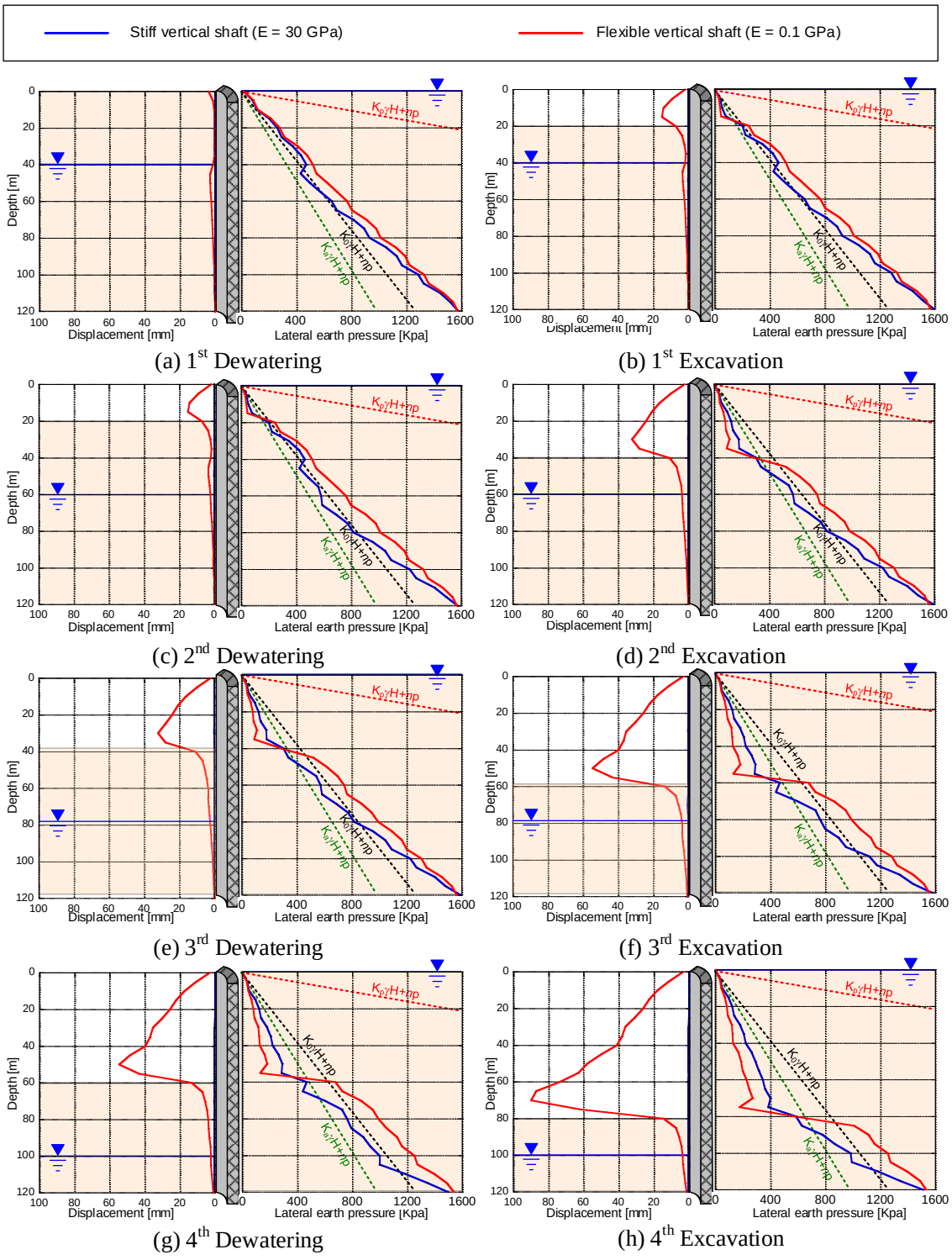

(a) 1st Dewatering (b) 1st Excavation

(c) 2nd Dewatering (d) 2nd Excavation

(e) 3rd Dewatering (f) 3rd Excavation

(g) 4th Dewatering (h) 4th Excavation

Figure 3.6 The result of inner displacement and lateral earth pressure acting on circular shaft

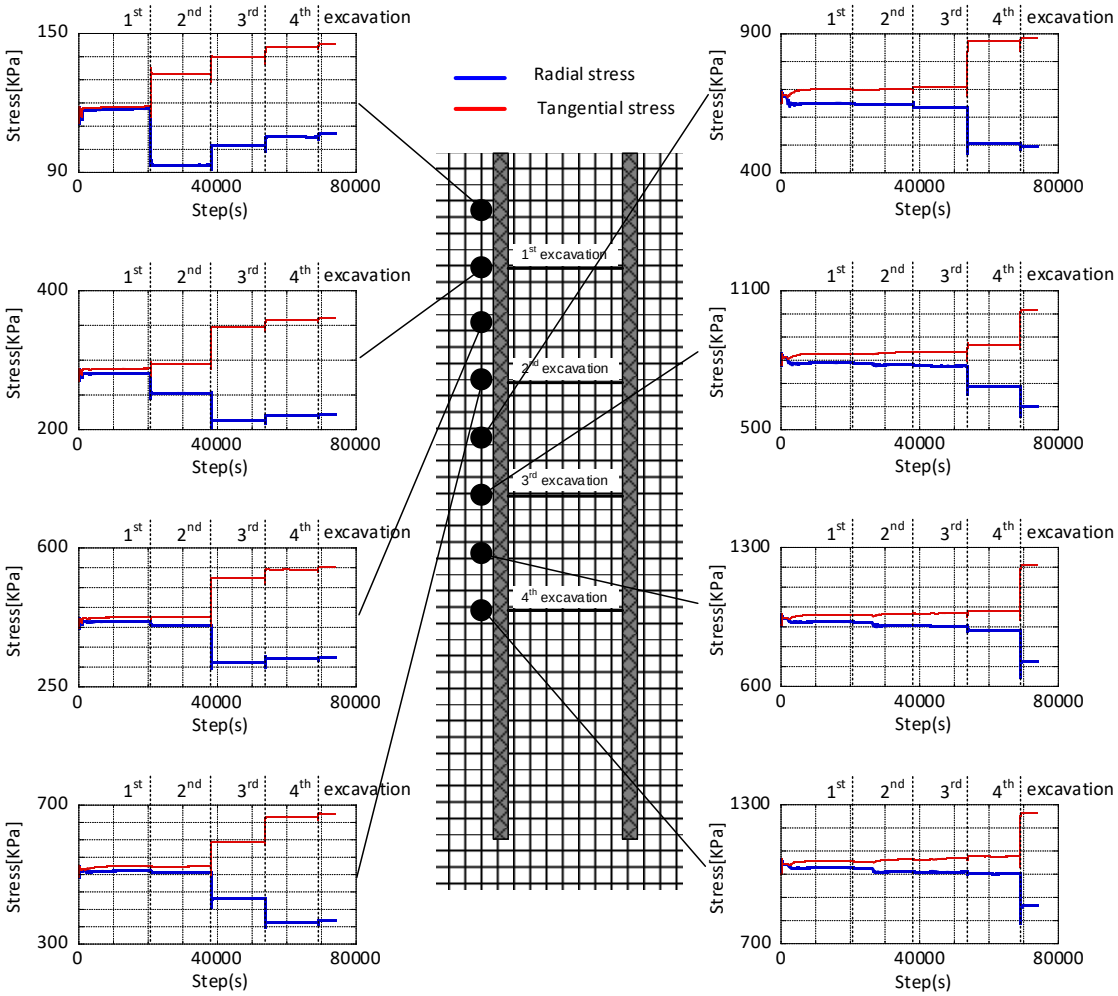

Figure 3.7 The stress history in tangential and radial direction

3.6 Excavation stability in circular vertical shaft during excavation process in high groundwater level

According to investigation on excavation stability, the rigid vertical shaft was used for this analysis, stiffness is 30 GPa. Because in soft vertical shaft generally provides large deformation which also influence on excavation stability. Therefore, in order to consider only the effect from dewatering system on excavation stability, shaft deformation should be neglected.

This section of analysis would show the behavior of soil inside circular vertical shaft (excavation area). According to high different groundwater level, caused by dewatering, could be a cause of seepage failure. Therefore, the analysis model would be

showing the several heights between dewatering location and excavation base which are 20 m, 10 m, 5 m and 2.5 m. The definition of relative mean effective stress,

$$1-\frac{\sigma'_m}{\sigma'_{m0}}$$

is used to express the excavation stability. If the value of relative mean effective stress is close to 1, it would be showing the un-stable excavation base.

3.6.1 Results of excavation stability

The excavation stability has been separated as 2 parts which are the soil heaving and relative mean effective stress contour. **Figure 3.8, 3.9, 3.10 and 3.11** show that the location which is unstable is always located at the excavation surface (value is close to 1). Also, from 2nd step of excavation has been performed, the value of relative mean effective stress of soil underneath excavation surface become increasing, especially in case of 20 m dewatering below excavation base. The comparison between different dewatering location shows that the deeper location of dewatering would be more stable. Eventually, the zone which have high value of relative mean effective stress is still exist at the excavation surface, even the dewatering location is deeper.

The heaving soil has been shown as in the **Figure 3.12**, which are showing for 2 cases of dewatering depth. As in the consequence, the soil heave of shallow dewatering and deep dewatering are similar for first 2 step of excavation. But when the excavation goes deeper (60 m and 80 m), there are some differences of soil heave. As in the **Figure 3.12(c) and (d)**, the soil heave of the 20 m dewatering depth is obviously higher than the 2.5 m dewatering.

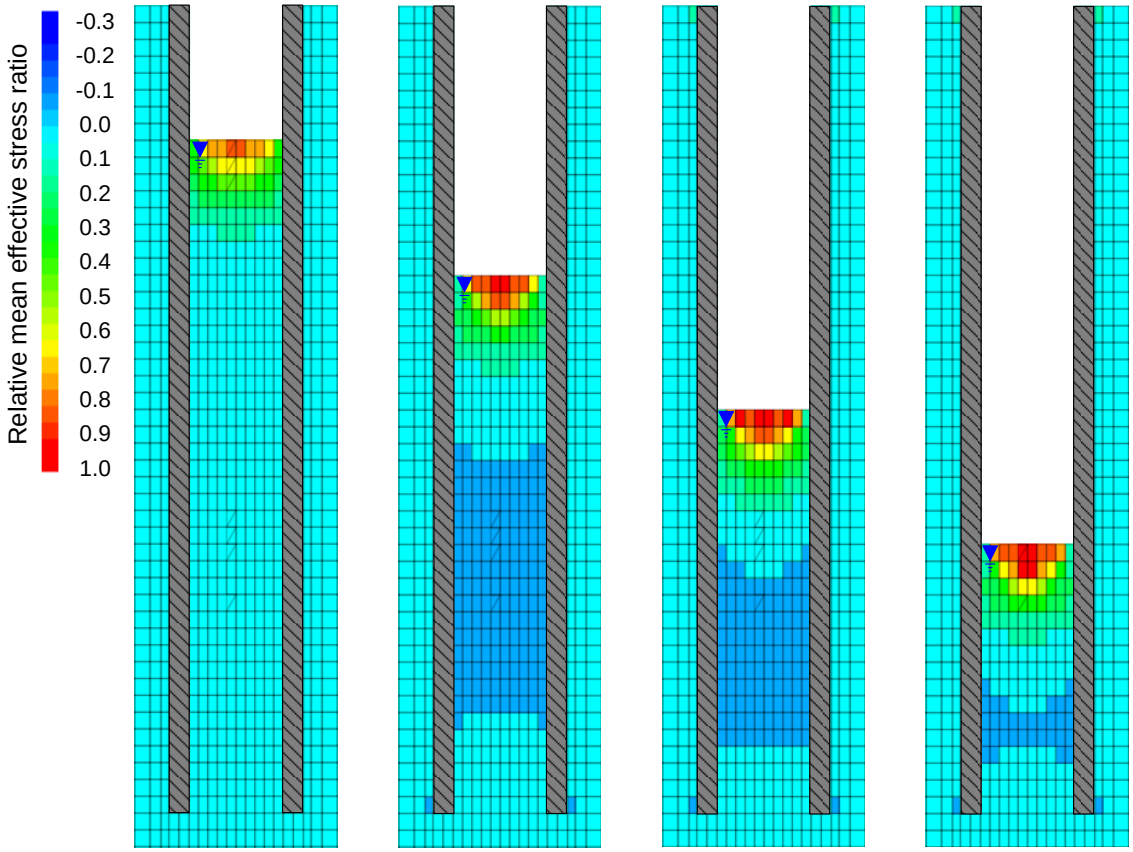

Figure 3.8 The depth of dewatering is 2.5 m below excavation base

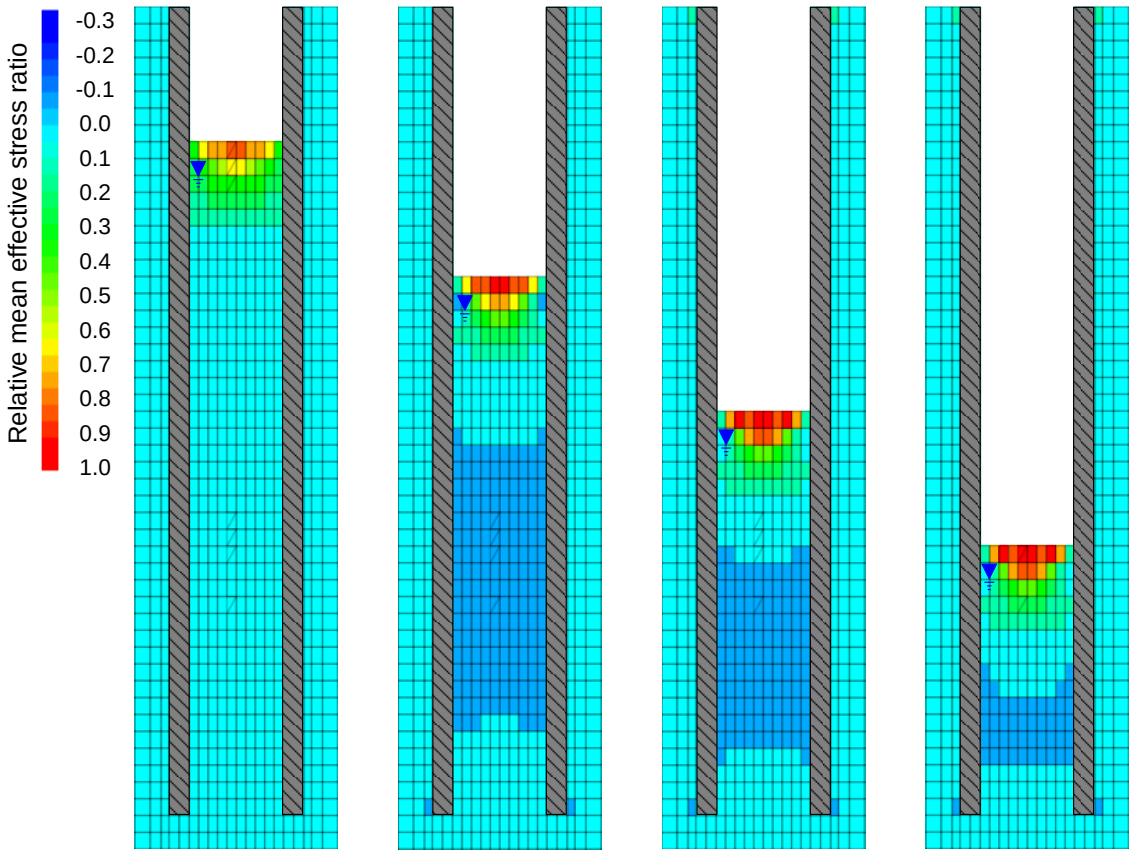

Figure 3.9 The depth of dewatering is 5.0 m below excavation base

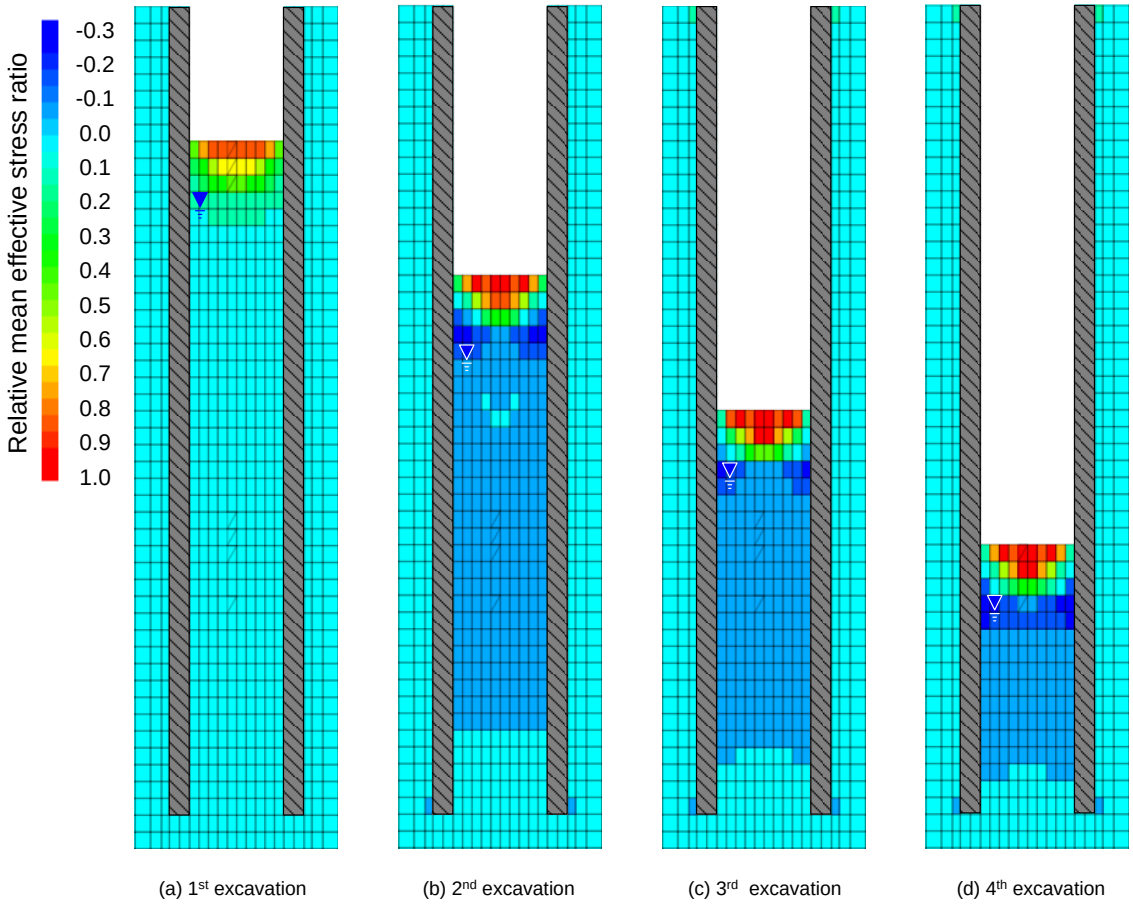

Figure 3.10 The depth of dewatering is 10.0 m below excavation base

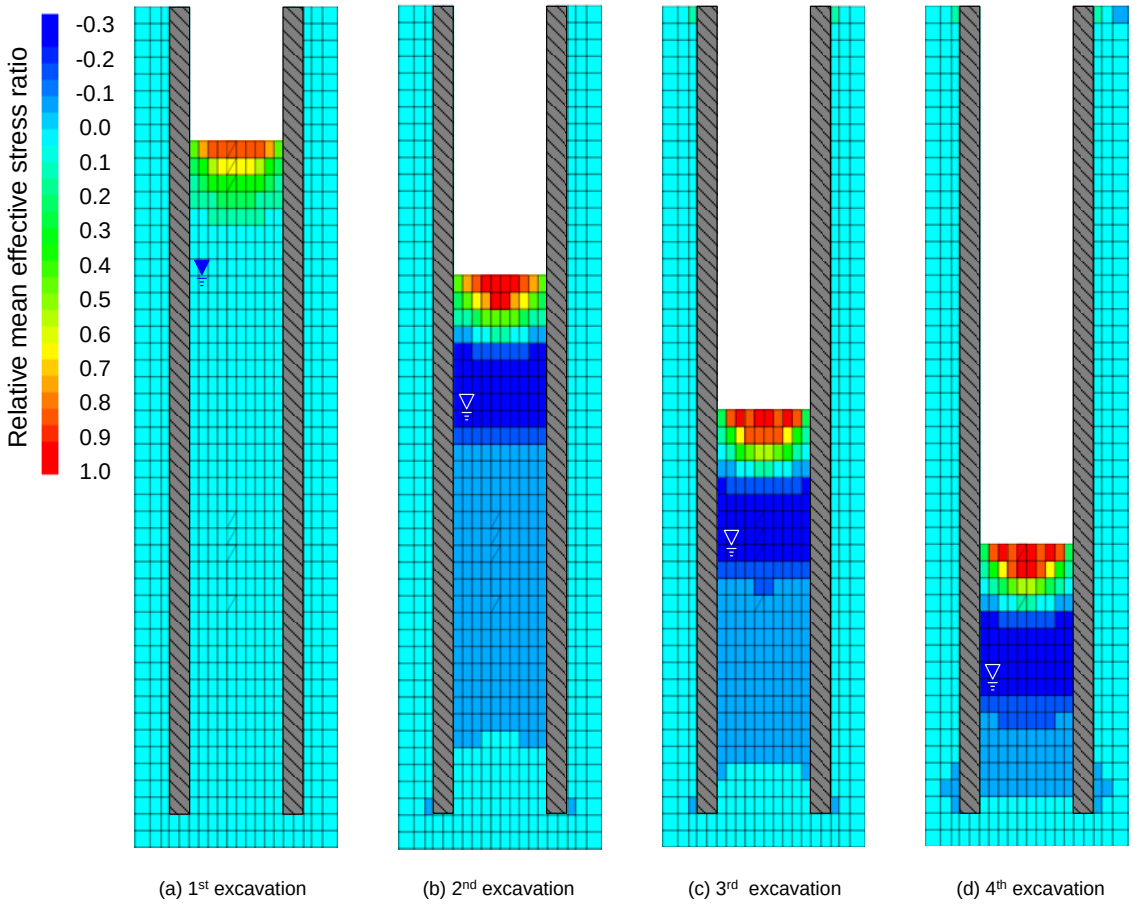

Figure 3.11 The depth of dewatering is 20.0 m below excavation base

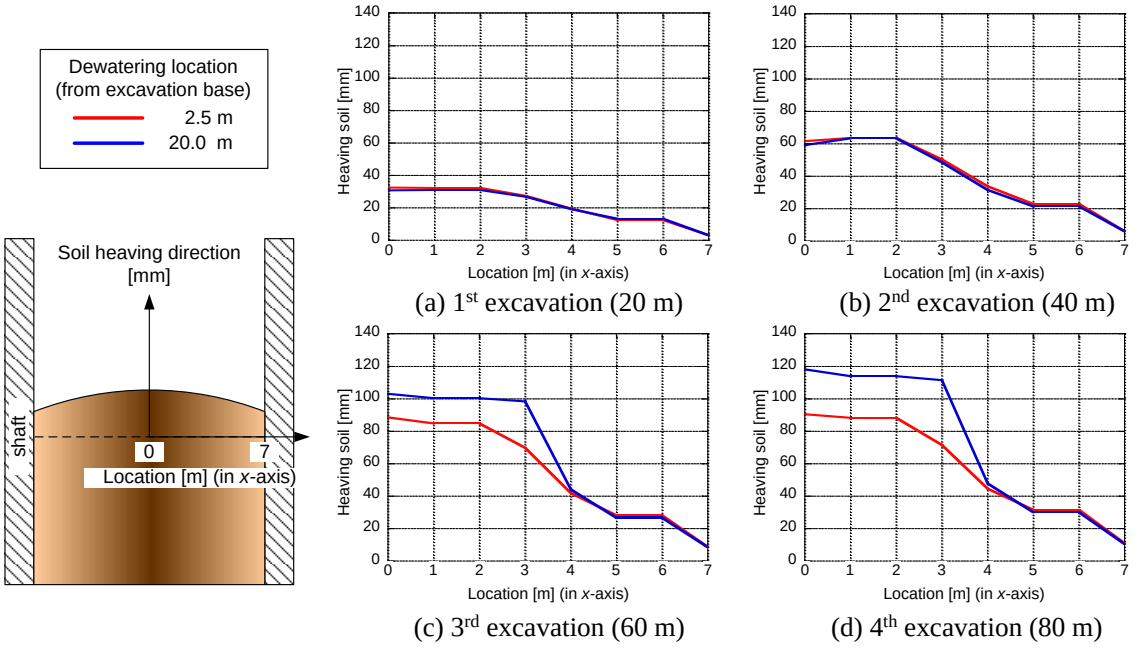

Figure 3.12 Heaving soil at excavation base

3.6.2 Discussion of excavation stability

The excavation stability has been influenced 2 main causes. Firstly, excavation stability is cause by releasing overburden pressure from excavation. Secondly, the influence of pore pressure from dewatering depth is also affecting on the excavation stability. Conversely, the value of relative mean effective stress of soil beneath excavation area become higher after 60 m excavation, because the wall deformation leads to be increasing additional confining pressure. However, the zone of high value of relative mean effective stress could be likely found more at excavation surface when the dewatering depth is located at deeper position. This behavior mainly cause by the deeper dewatering depth reduces more resisting pressure toward the shaft wall, therefore, the deformation of vertical shaft will be larger as well. According to this mechanism, the confining pressure on the soil close to excavation area must be more when the dewatering depth is at the lower position, hence, it effects on the high relative mean effective stress,

Another aspect, which expressing in term of heaving soil, also shows that the soil heave of 20 m dewatering is higher. According to the deep dewatering also release the resisting lateral pressure (inside circular shaft). Therefore, the heaving soil influence by the vertical strain which caused by additional confining pressure. Moreover, the soil heave shape is similar with reverse bell curve which have crest at center. Also, the height of soil heave in each excavation steps are different. The highest soil heave is found at the deepest excavation which is 80 m excavation.

3.7 The pore pressure and fluid flow during the shaft construction

As it mentioned earlier, the vertical shaft construction in high groundwater zone, the dewatering process is required, especially in sandy ground. According to the dewatering utilization during shaft construction, at the same depth, the pore pressure between inside vertical shaft and outside would not be equal due to the water heads are different. Therefore, the fluid flow is basically occurred due the hydraulic gradient.

3.7.1 Result of pore pressure and fluid flow

In this section, the pore pressure in the simulation which was conducted in the previous section will be shown. The pore pressure of the element along the shaft wall was selected and shown in **Figure 3.12**. The pore pressure result is obviously showing that the hydraulic gradient in depth direction between both inside and outside are different. Furthermore, the result of pore pressure contour and vector of fluid flow are shown together. In addition, the pore pressure and vector field of fluid flow at each step of construction are separately shown as in **Figure 3.13**.

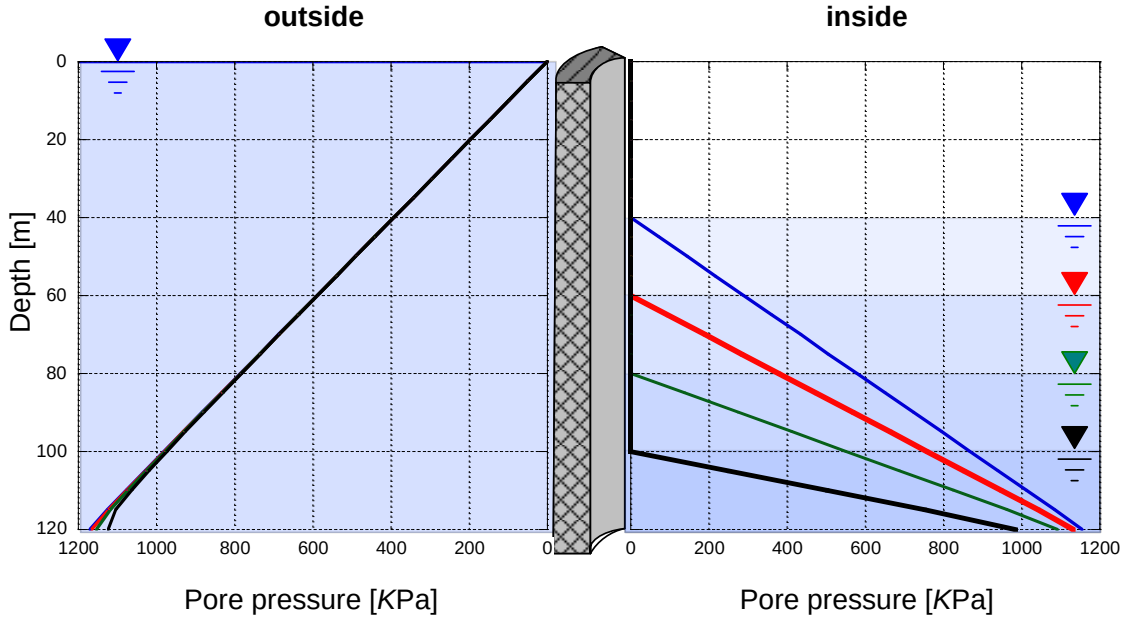

Figure 3.12. Pore pressure distribution for 4 steps of dewatering

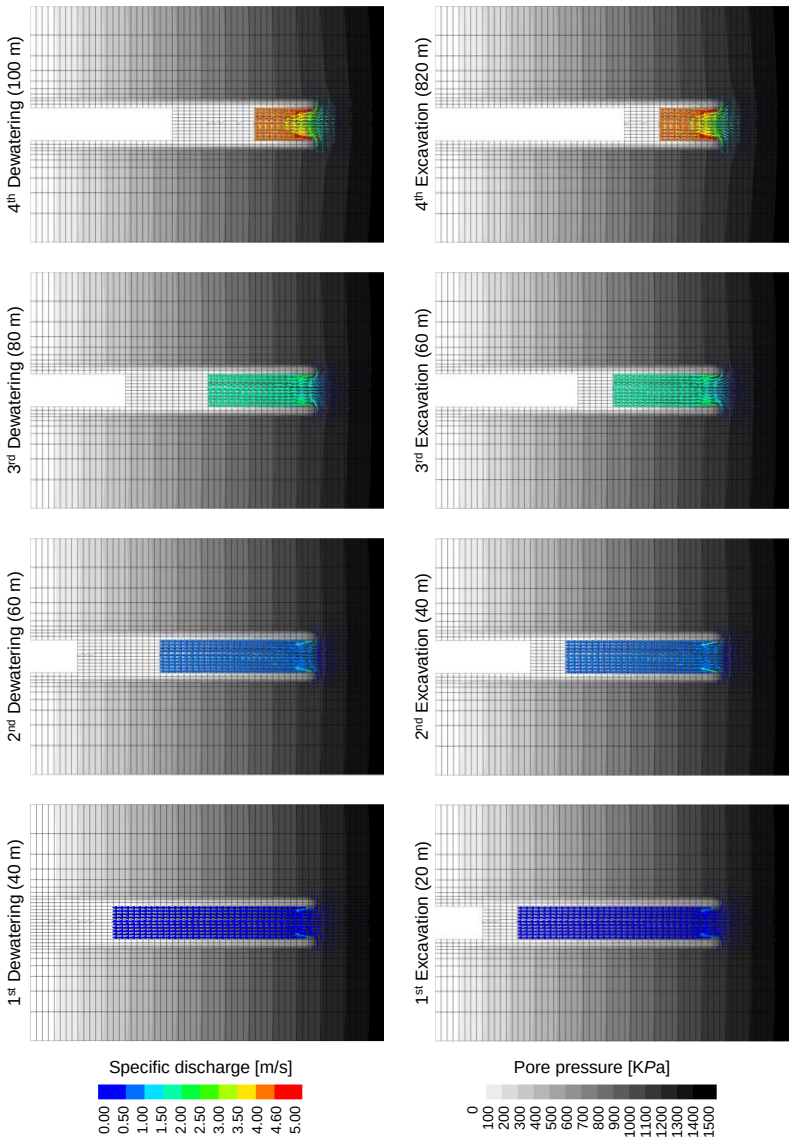

Figure 3.13. Contour of pore pressure and specific discharge

3.7.2 Results of fluid flow velocity at each specific location

The seepage flow is one of the main concerns which might cause a failure due the suffusion. Therefore, the observation at several location in numerical simulation is done in this section to show the seepage history during vertical shaft construction. Figure 3.14 shows the seepage flow velocities history of each specific location along vertical shaft. The results have illustrated that the changes in seepage flow is mainly triggered by dewatering process which is necessary for excavation in high groundwater level area. Moreover, the soil mass beneath the tip of vertical shaft tends to encounter with higher

seepage flow velocity.

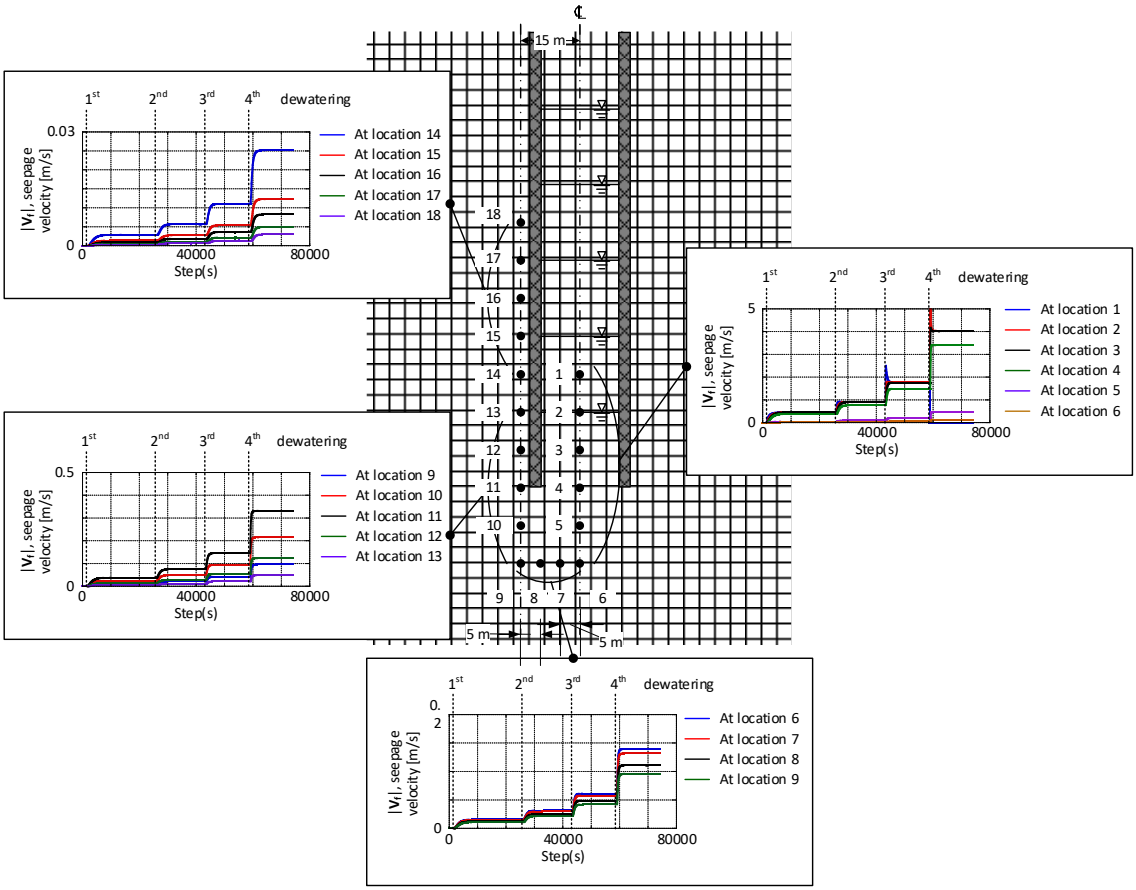

Figure 3.14 The seepage flow velocity of each specific locations along vertical shaft

3.7.3 Discussion of pore pressure and fluid flow

The simulation result shows that the pore pressure gradient in depth direction at inner side has more grater gradient than the outside of shaft wall. According to the bottom of shaft wall, the fluid is allowed flow through permeable material (soil) beneath the shaft wall, therefore, the pore pressure at the inner side which is close to the bottom of shaft wall becomes close to the pore pressure from outside, However, the pore pressure at the bottom of shaft between both inner and outer are slightly different in which the pore pressure at outside is higher than inner side, especially at final step of dewatering process. According to the 80 meters dewatering depth, the pore pressure at outside shaft is about 1100 K*Pa*, while the pore pressure at inner shaft is about 900 K*Pa*. Therefore, the pressure gradient is radial direction is also occurring, and the water would be flowing into the inner shaft. Furthermore, the flow vector field result has confirmed the previous result of pressure

difference at the bottom of shaft. As shown in **Figure 3.13**, the fluid flow is moving from the surrounding zone through the soil layer beneath the shaft and going upward to excavation surface. Moreover, the seepage velocity in the soil layer that vertical shaft lies on become higher when the dewatering depth is going deeper.
However, this simulation was done by abruptly change the pore pressure, hence, the fluid flow velocity is always suddenly changed. In addition, the excessive fluid flow velocity could be found as well, especially at the position close to the dewatering location (inside vertical shaft).

3.8 Conclusion

The numerical simulation could suggest some unfamiliar behavior of excavation process in deep circular vertical shaft. From the fundamental result, the lateral stress distribution is slightly different since shaft installation which caused by difference wall stiffness. Over the excavation base, lateral pressure is decreasing which must be caused by arching effect. The reduction of lateral earth pressure of soft vertical shaft is higher than rigid vertical shaft, even the initial lateral pressure along soft shaft is higher than rigid shaft. The maximum displacement of wall is always located at 5 m above excavation surface.

The dewatering system in circular shaft excavation is necessary to be used which would increase excavation stability. Conversely, indirect effect, which could be increasing soil heave, is come from dewatering as well. According to the consequence, the average depth of unstable zone is about 10 m depending on dewatering depth. Therefore, the deep dewatering location is not always providing advantage for excavation stability, but we have to consider the optimum depth.

Nevertheless, an approaching to understand the stability of excavation inside vertical shaft could be showing only heaving soil at the excavation surface. According to the limitation of the current simulation model, the soil-water coupling simulation still could not explain some behavior such erosion which is likely to occur. According to the high seepage flow is moving beneath the bottom of shaft. Therefore, the soil mass is subjected by the irregular seepage flow could be leading to erosion problem. Furthermore, the dewatering method which was used in the construction process basically induces the difference in water head between inside and outside shaft. Hence, the seepage flow

velocity become higher when the dewatering is applied at the deeper area. Therefore, the further study on erosion such internal erosion is much obligated with the elucidation on the unknown behavior in cylindrical shaft construction in shallow groundwater area.

Chapter 4 Numerical simulation scheme for an erosion

4.1 Introduction

According to the previous research, erosion model for even suffusion or piping type which is used currently still relying on experimental test. Mostly, the erosion model is composed of two main parts which is initiation of erosion and erosion rate, while erosion transportation is rarely investigated. Therefore, the erosion simulation is mainly controlled by the erosion rate which normally a linear empirical equation which obtained for specific soil. This research aims to study on the suffusion erosion or internal erosion by using Finite Difference method (FDM) discretization for an advection equation which is used for erosion transportation. This chapter is going to investigate on the proper erosion model which can be used for difference gradation of cohesionless soil. In this chapter, the erosion model will be associated by force equilibrium concept. Hence, the validity of this model implementation is compared with experimental test from previous research.

4.2 Internal erosion (Suffusion) mechanism

The suffusion is the phenomenon that the fine particle or erodible particle is carried out from the soil mass, as shown in **Figure 4.1**, once the seepage flow is applied. Therefore, it could be implied that the detachment of erodible particle due to the seepage flow is mainly induced by drag force. On the other hand, the larger particle or coarse material is still remaining inside the soil mass and being as soil skeleton, therefore, the amount of erosion mainly depends on the fine particle fraction. In addition, the changes in particle is also sometimes influence on the volumetric strain due to the rearrangement of soil particle. However, in this erosion scheme still does not consider the mechanical behavior of the soil mass encountering erosion. Similar behavior which might be difficult to distinguish from suffusion is sand boiling or piping, there is a difference in the gradation of soil. Normally, suffusion is found in gap-grade soil in which large particle size standing for soil skeleton while fine particle tends to be eroded. The internal erosion will cause an extra void occurring inside the material which could lead to a deformation.

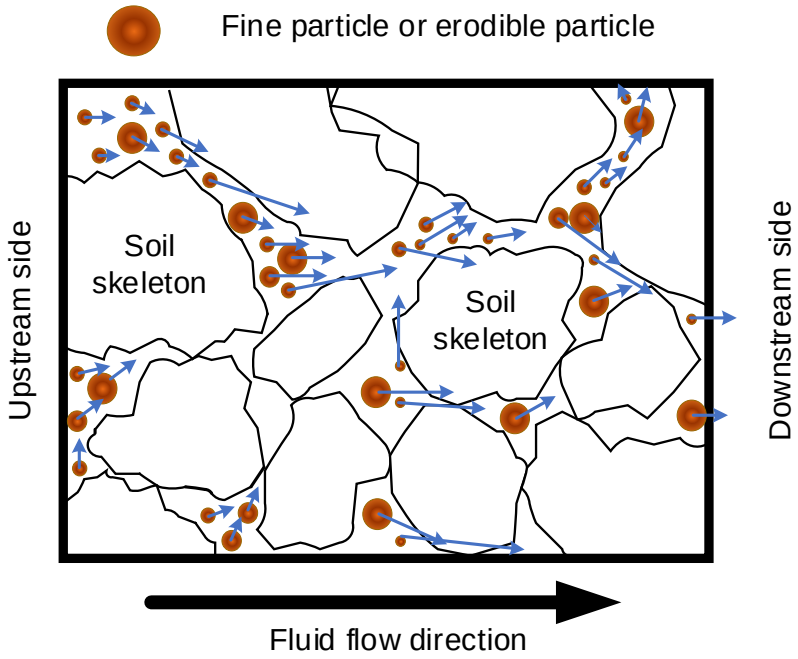

Figure 4.1. Internal erosion (Suffusion type)

4.3 Numerical method

4.3.1 Advection equation

According to the aim of this research, the transportation of erodible particle is a main concern, therefore, the equation which could explained the particle transportation must be initially acquired. In particle flow simulation, the advection equation always associates with the particle transport or moving particle in several media, for an example, the transport of silt in the river. According to advection definition, advection is a transport of substance in accordance with the bulk motion, therefore, the substance in erosion issue would be fine particle or erodible particle while the bulk motion is fluidized motion. The advection equation is the governing equation of motion in scalar field which is transported or advected by known velocity in vector field.

In addition, the advection equation is a derivation of conservation law by Gauss theorem. The basic assumption is that there is a certain initial amount of substance, G_α, remained at time, t, in the space with volume U within the surface S as shown in **Figure 4.2**. Considering the rate of change of G_α, it would be $\frac{DG_\alpha}{Dt}$ in accordance with the

Lagrangian point of view. Conversely, the Eulerian approach shows that a volume of system at time t and $t + \Delta t$ could be expressed as $U = U_1 + U_2$ and $U^{/} = U_2 + U_3$, respectively **(Bear J.; 1988)**. Therefore, the temporal rate of change of G_α can be shown as in **Equation 4.1**.

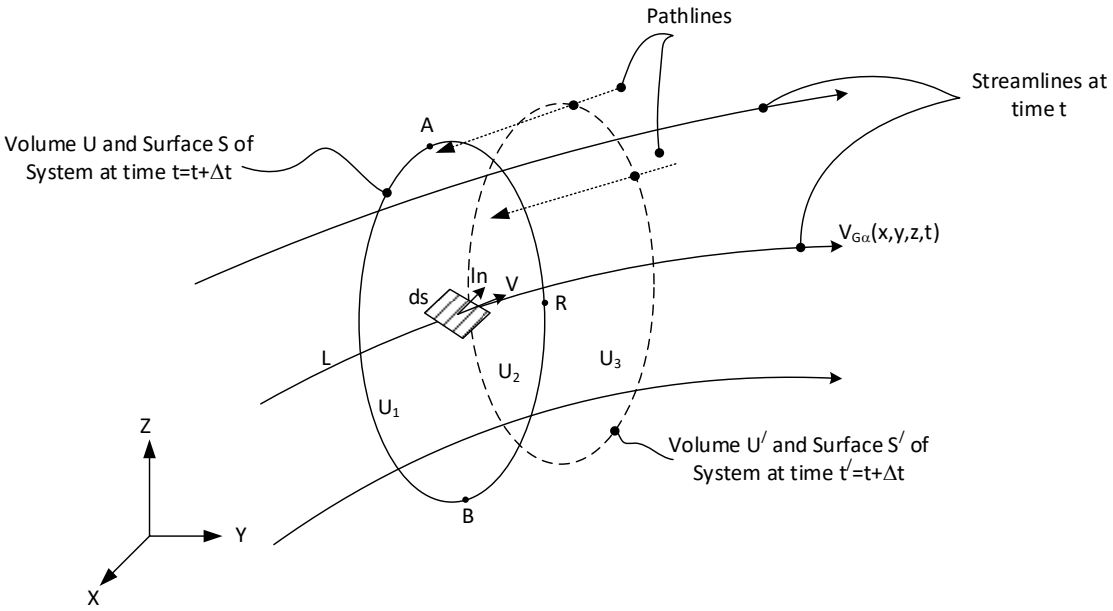

Figure 4.2. Nomenclature for deriving the transport theorem (advection equation) (Bear J.; 1988)

$$\left.\frac{DG_\alpha}{Dt}\right|_{system} = \lim_{\Delta t \to 0}\left\{\frac{[(G_\alpha)_2+(G_\alpha)_3]_{t+\Delta t}-[(G_\alpha)_3+(G_\alpha)_2]_t}{\Delta t}\right\} \tag{4.1}$$

Where, $(G_\alpha)_i = \int_{(U_i)} g_\alpha dU,\ i = 1,2,3$, and g_α is the concentration of substance.

According to infinitesimal time change, $\Delta t \to 0$, on the right side of the Equation 4.1 could be reduced as in the **Equation 4.2**.

$$\left.\frac{DG_\alpha}{Dt}\right|_{system} = \frac{\partial}{\partial t}\int_{(U)} g_\alpha dU + \int_{(S)} g_\alpha V_{G_\alpha} \cdot dS \tag{4.2}$$

Where, V_{G_α} is the flow velocity of substance.

From the Divergence theorem or Gauss's theorem, the Equation 4.2 could be transformed to be **Equation 4.3**.

$$0 = \int_{(U)}\left[\frac{\partial g_\alpha}{\partial t} + div\left(g_\alpha V_{G_\alpha}\right) - I_\alpha\right] dU \tag{4.3}$$

Where, I_α is a temporal rate of production per unit volume which represents for a

production of the property take place within U.

Finally, for considering a general form of an advection, g_α and V_{G_α} will be replaced by φ_n and $u_{i,n}$, respectively, while using S_φ as a source term instead of I_α. Therefore, the general form of advection equation could be expressed in the partial differential equation (PDE) as **Equation 4.4**.

$$\frac{\partial \varphi_n}{\partial t} + \nabla \cdot (\varphi_n u_{i,n}) = \frac{\partial \varphi_n}{\partial t} + u_{x,n}\frac{\partial \varphi_n}{\partial x} + u_{y,n}\frac{\partial \varphi_n}{\partial y} = S_\varphi \tag{4.4}$$

4.3.2 Finite Difference method

In this research, the Finite Difference method or FDM will be used to solve the advection equation in accordance with their simplicity. Finite Difference method is one of the numerical techniques for partial differential equation discretization and their scheme could be shown by Taylor's expansion. According to the pioneer simulation which will be one-directional flow to validate with previous experimental test, the simple finite difference scheme would be initially applied. There are mainly two simple schemes for an explicit in time which is FTCS (Forward Time Centered Space) and upwind (UFDM) scheme.

The consideration of suitable scheme is necessary because sometimes it might cause unstable condition in analysis. According to the governing equation, an advection equation could be classified as a hyperbolic particle differential equation. Therefore, the investigation on stability of advection discretization by FTCS scheme and UFDM scheme would firstly be examined by using von Neumann stability analysis.

Forward Time Centered Space (FTCS) scheme

As it mentioned earlier, the discretization would be centered in space while explicit in time as shown in **Figure 4.3** and equation for one dimensional calculation yields as it shown in **Equation 4.5**.

$$\frac{\varphi_i^{j+1} - \varphi_i^j}{\Delta t} = -u_i \frac{\varphi_{i+1}^j - \varphi_{i-1}^j}{2\Delta x} \tag{4.5}$$

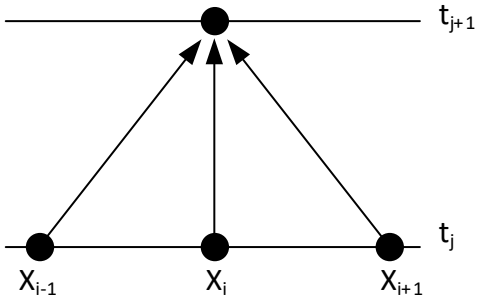

Figure 4.3. Schematic of Forward in time and Centered in space (FTCS)

The stability of advection discretization associated by FTCS scheme could investigate through von Neuman stability analysis. According to this analysis, the error in the approximation of partial differential equation could expand into a Fourier series, therefore, the equation used to explain a harmonic of the error can be shown as **Equation 4.6**.

$$\varepsilon_i^j \sim e^{ikx_i}, \quad k \in \mathbb{R} \tag{4.6}$$

Hence, von Neuman stability analysis with FTCS scheme (Equation 4.5) could yield as the **Equation 4.7**.

$$\varepsilon_i^{j+1} = e^{ikx_i} - \frac{u_i \Delta t}{2\Delta x}\left(e^{ik(x_i+\Delta x)} - e^{ik(x_i-\Delta x)}\right) = \left(1 - \frac{u_i \Delta t}{2\Delta x}\left(e^{ik\Delta x} - e^{-ik\Delta x}\right)\right)\varepsilon_i^j \tag{4.7}$$

Where, ε_i^{j+1} is the accumulative rounding error.

The comparison between **Equation 4.6** and **Equation 4.7**, it could be implied that $g(k) = \left(1 - \frac{u_i \Delta t}{2\Delta x}\left(e^{ik\Delta x} - e^{-ik\Delta x}\right)\right)$. And the stability would be occurring with criteria following the **Equation 4.8**.

$$|g(k)| \leq 1, \ \forall k \tag{4.8}$$

Therefore, the square of $g(k)$ could show a better understanding of this scheme stability with advection equation as in **Equation 4.9**, the result shows that it always greater than unity. Therefore, this scheme is unconditionally unstable.

$$|g(k)|^2 = 1 + \frac{{u_i}^2 \Delta t^2}{\Delta x^2} sin^2(k\Delta x) \tag{4.9}$$

Upwind (UFDM) scheme

Similarly, the upwind scheme is an explicit in time while it is a backward in space. Nevertheless, this scheme could be leading an unstable condition in which reverse flow is occurred. According to this scheme, the discretization equation is shown as in the **Equation 4.10**. According to the limitation of upwind scheme, the direction in vector field must be known in the direction firstly, therefore, the scheme could be defined as in schematic visualization in **Figure 4.4** in **Figure 4.4 (a)** and **Figure 4.4 (b)**.

$$\varphi_i^{j+1} = \varphi_i^j - \frac{(u_i \Delta t)}{\Delta x}\left(\varphi_{i+1}^j - \varphi_i^j\right) \qquad (u_i < 0) \qquad \text{or}$$

$$\varphi_i^{j+1} = \varphi_i^j - \frac{(u_i \Delta t)}{\Delta x}\left(\varphi_i^j - \varphi_{i-1}^j\right) \qquad (u_i > 0) \qquad (4.10)$$

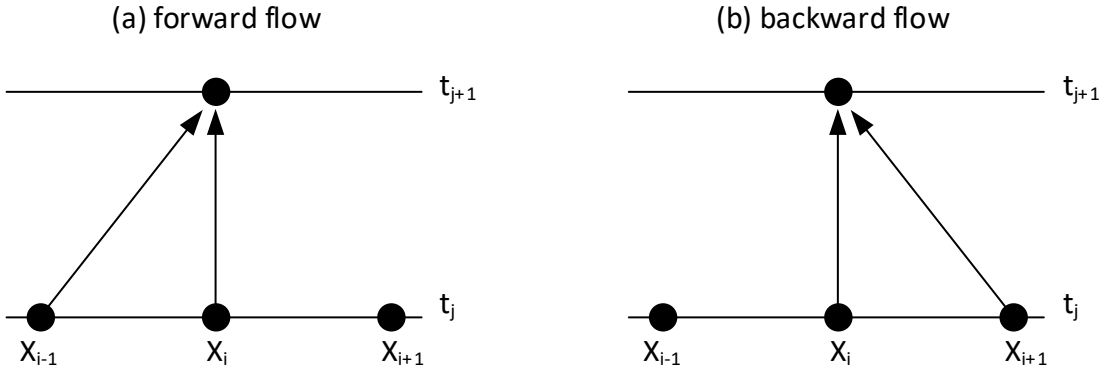

Figure 4.4. Schematic of Upwind scheme

Similarly, the stability of advection discretization associated by upwind scheme could be shown in the **Equation 4.11** under the same analysis with previous scheme.

$$g(k) = 1 - \frac{u_i \Delta t}{\Delta x}\left(1 - e^{-ik\Delta x}\right) = 1 - \alpha + \alpha e^{i\beta} \qquad (4.11)$$

Where, $\left|\alpha = \frac{u\Delta t}{\Delta x}\right|$ and, $|\beta = -k\Delta x|$.

According to the **Equation 4.11**, the analysis would be stable in only some condition as follow **Equation 4.12**.

$$|g(k)| \leq when\ 1 - \alpha \leq 0,$$

$$\therefore \frac{u\Delta t}{\Delta x} \leq 1 \quad or \quad u \leq \frac{\Delta x}{\Delta t} \qquad (4.12)$$

Therefore, this simulation would pick up an upwind scheme for first simulation with directional flow while the analysis would be conditionally stable.

4.4 Background of erosion simulation

The advection is the movement of bulk motion which might drag or carry some substance such particle together with the majority of the advected substance. Therefore, the particle transportation through porous media by the water flow motion, which is considered as a majority of the advected substance, is described by using the advection equation **(Yang et al.; 2020, Russel Em.; 1992)**. According to the partial differential equation of advection as shown in **Equation 4.13**, the velocity of particle, $u_{i,n}$, represent to the particle flow velocity or erodible particle velocity for the erosion phenomena.

$$\dot{\varphi}_i + \mathbf{u}_\mathbf{e}^\mathbf{i} \cdot \boldsymbol{\nabla}\varphi_i = S_\varphi \tag{4.13}$$

Where, φ_i is concentration of erodible particle and S_φ is the source term which could represent for the exchange rate between non-erodible fraction and erodible fraction. In addition, subscript i means the difference particle size.

Basically, the particle flowing in fluid phase, the flow surrounding particle exert a difference drag force on particle which is greatly depending on a particle size, sphericity, and the current flow velocity of particle **(Snorri Gudmundsson; 2014)**. Therefore, the erodible particle flow might not be considered as a group with very wide distribution in particle size through porous media under this advection equation.

According to the primary concept in this section of simulation, not only drag force is considered here but also body force acting on the particle will be considered as well. There are two more body forces which could associate with the movement of erodible particle in porous media which is gravitational force and buoyancy force. The gravitational force normally exerts the force in the direction of gravity while the buoyancy force generally exerts in the opposite direction. The buoyancy force is basically described by Archimedes theory which is the same amount with the weight of fluid replaced by object. Therefore, the force acting on the erodible particle would be shown as in **Figure 4.5**.

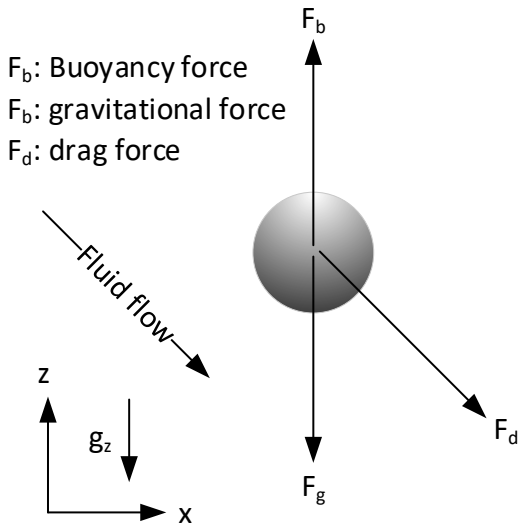

Figure 4.5. Force component on the erodible particle

Currently, numerical modelling of erosion basically considers the erosion for specific soil, the erosion rate is the function of hydraulic shear stress which is needed to obtain from an experiment. Therefore, the different soil could not be predicted with the same model. In addition, the consideration of gradation of soil is pretty much important in accordance with the moveable fine content. Hence, this research tries to make an erosion model for various types of cohesionless soil through investigation of cohesionless soil gradation.

According to the particle transportation, the different particle size would travel with different speed under the same motion of fluid flow, majority of the advected substance. The erodible particle flow is separately described under the advection equation in correspondence with subscript *n* in the equation. The soil model is considered as a three phases model; 1. Fluid, 2. Erodible soil, and 3. Soil skeleton. The erodible particle is divided for several fractions as following the different size of particle as shown in **Figure 4.6**.

As for the notations and symbols in this section, bold letters denote vectors; "·" denotes an inner product of two vectors (e.g., $\mathbf{a} \cdot \mathbf{b} = a_i b_i$); "| |" denotes the norm of a first-order tensor (e.g., $|\mathbf{a}| = \sqrt{\mathbf{a} : \mathbf{a}} = \sqrt{a_i a_i}$); " $\dot{}$ " denotes the time derivative; and the subscript zero denotes the initial state (e.g., v_0 = initial specific volume).

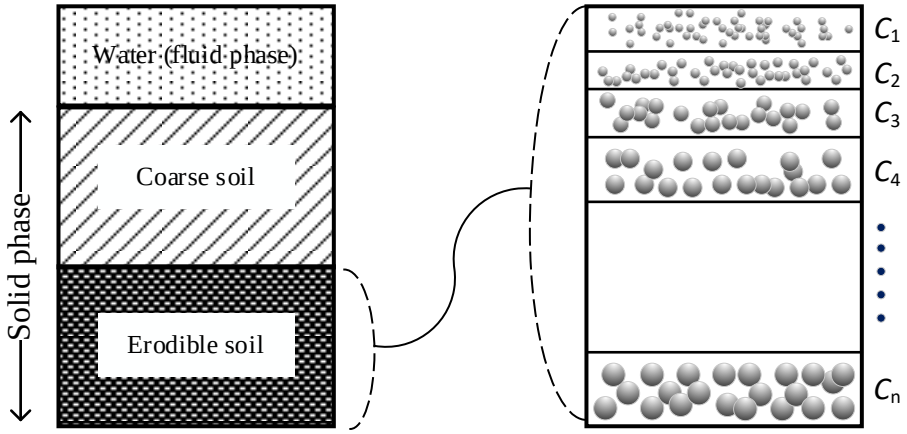

Figure 4.6. The concept of soil model for erosion calculation

Therefore, the total volume of soil mass, V_T, should be the summation among erodible soil, soil skeleton, and fluid volume as follow **Equation 4.14**.

$$V_T = V_e + V_s + V_{void} \tag{4.14}$$

Where, V_e is the erodible soil volume, V_s is the soil skeleton volume, and V_{void} is the volume of fluid.

Furthermore, the volume of erodible particle must be divided as several groups for representing as an individual size of erodible particle in narrow range, hence, the V_e must be replaced by the relationship as in **Equation 4.15**.

$$V_e = \sum_{i=1}^{n} V_e^i \tag{4.15}$$

Where, V_e^i is the volume of erodible particle in group i.

According to the body force of erodible particle, there are three main force which might play a big role in the behavior of particle flow in porous media. As it mentioned earlier, there are three main components; 1. Drag force, F_D, 2. Gravitational force, F_G , and 3. Buoyant force, F_B.

The gravitational force can be simply explained by as in **Equation 4.16**.

$$\mathbf{F_G} = \rho_s V_s \mathbf{g} \tag{4.16}$$

Where, ρ_s is the density of particle, and V_s is the volume of particle.

Considering in the acceleration fluid, the buoyant force obtained from the Archimedes' principle could explain in the inertial frame of reference in accordance with

classical physics. In addition, the Einstein's equivalence principle explains that there is no difference in an accelerating frame of reference and in a gravitational field. Therefore, the buoyant force could be become **Equation 4.17**.

$$\mathbf{F_B} = -\rho_f V_s(\mathbf{g} + \mathbf{a_f}) \tag{4.17}$$

Where, ρ_f is the density of fluid, $\mathbf{a_f}$ is the fluid acceleration.

Drag force is one of the force components that can cause a particle flow by both pressure drag and skin friction drag. According to the previous research about particle flow, the utilization of drag force from aerodynamic law always shows a promising result in many research field **(Chadil M.A., Vincent S. & Estivalezes J.L.; 2018).** The aerodynamic drag force, the force acting on the particle is proportional to the square of the relative velocity between fluid and particle as in Equation 4.18.

$$\mathbf{F_D} = \frac{1}{2}\rho_f C_d A_p |\mathbf{u_f} - \mathbf{u_p}|(\mathbf{u_f} - \mathbf{u_p}) \tag{4.18}$$

4.5 Calculation scheme

In this chapter, the simulation aims for an investigation on the proper erosion model formulation for describe the suffusion behavior. The model will be validated with previous experimental result which was controlling the fluid flow condition, therefore, the calculation scheme in this part will not deal with the fluid flow calculation. **Figure 4.7** shows the erosion calculation scheme including two main paths which are the erosion calculation and fluid flow formulation. However, as it mentioned earlier, the fluid flow calculation will not be described in this section due to the aim of numerical formation of erosion scheme. According to the experiment from Ke & Takahashi (2014), the fluid flow through porous media was technically controlled **(Lin Ke & Akihiro Takahashi; 2014)**. Therefore, the manually giving a fluid flow velocity in correspondence with the experiment is required instead of solving diffusion equation for fluid flow. Therefore, the research work in this section will be trying to form the numerical simulation with different force component acting on the erodible particle to obtain the suitable model for suffusion calculation.

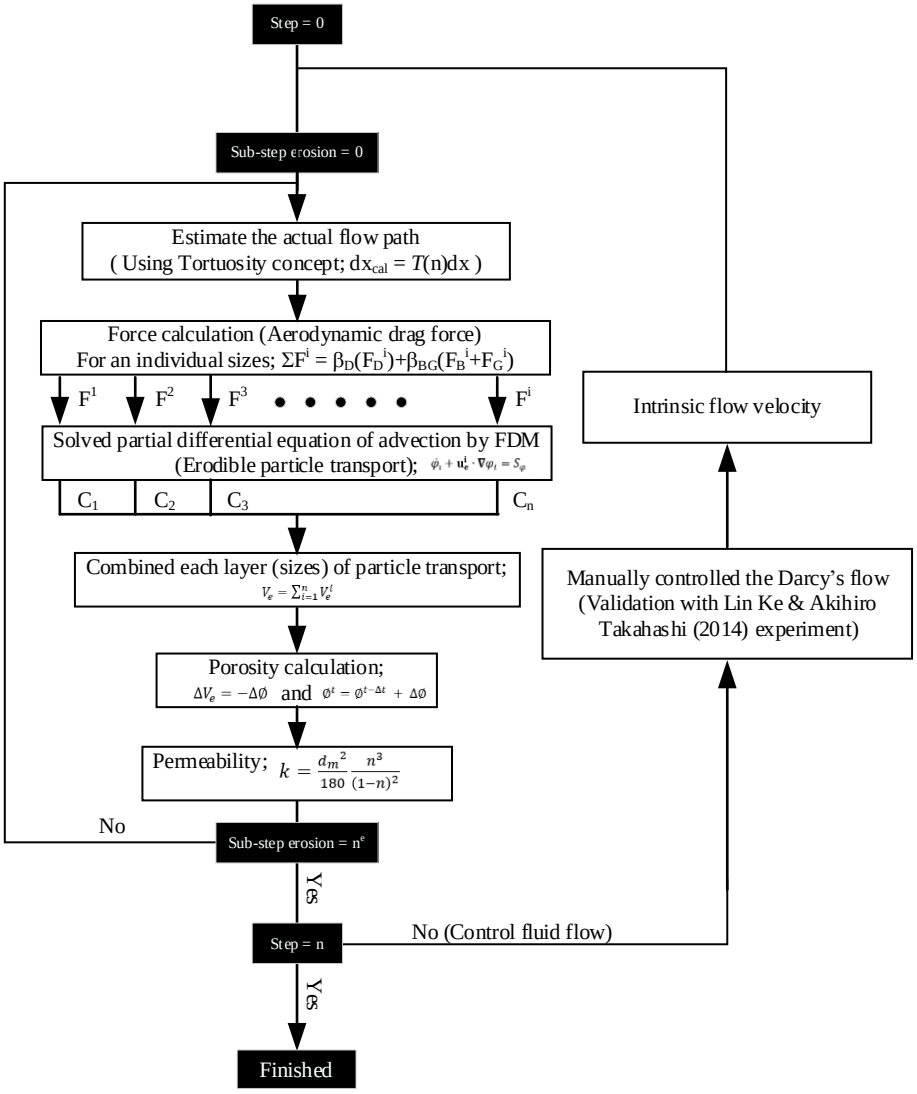

Figure 4.7. Flowchart of erosion calculation

In the erosion calculation, it begins from force calculation which is governed by the summation of force from aerodynamic law, gravitational force, and buoyant force. According to the drag force equation, it is a function of particle diameter, therefore, the drag force, F_D^i, calculation is calculated individually for each erodible particle sizes. In addition, the original drag force equation, as shown in **Equation 4.18**, is originally developed for considering a single particle flow, which mean it is not capable for considering a group of particle flow. Rusche and Issa (2000) recommended that it should have an effect of phase fraction on drag force **(Rusche H. & Issa R.; 2000)**. Therefore, the multiplier of drag force coefficient, $f(\alpha)$, is necessary to add into the original

equation, then, it becomes **Equation 4.17**.

$$\mathbf{F_D^i} = \frac{1}{2}\left[f(\alpha)C_D^i\right]\left[\frac{\pi}{4}\left(d_e^i\right)^2\right]\rho_f(\mathbf{u_e^i} - \mathbf{u_f})\left|\mathbf{u_e^i} - \mathbf{u_f}\right| \tag{4.19}$$

Where, C_D^i is the drag force coefficient for single particle flow, $f(\alpha)$ is a multiplier on drag force coefficient, d_e^i is the diameter of erodible particle, ρ_f is the density of fluid, $\mathbf{u_e^i}$ is the particle velocity, $\mathbf{u_f}$ is the fluid velocity, and the subscript i represent for each particle group (size). In addition, the multiplier on a drag force coefficient, $f(\alpha)$, is a function of particle fraction, α, which has a relationship as follow **Equation 4.20**.

$$f(\alpha) = \exp(K_1\alpha) + \alpha^{K_2} \tag{4.20}$$

Where, α is a particle phase fraction, K_1 and K_2 are the coefficients which is recommended to be 2.68 and 0.43, respectively, in accordance with particle flowing system **(Rusche H. & Issa R.; 2000)**. According to the relation between particle fraction and drag force multiplier for the type of particle flow, the multiplier increases when the particle phase become greater, conversely, when the particle fraction, α, is very close to zero, the multiplier is becoming unity or it represents for single particle flow as it described in **Figure 4.8**.

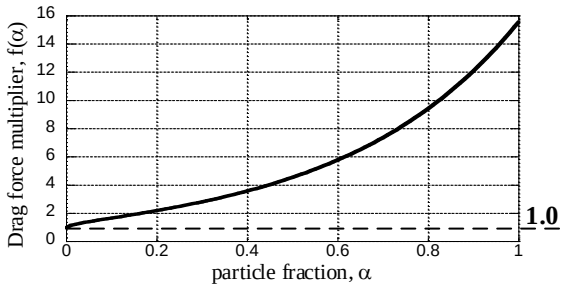

Figure 4.8. The relation between particle fraction and drag force multiplier

Moreover, there are several suggestions for the drag force coefficient, especially, for the case of single particle flow in fluid phase. The drag force coefficients depending on particle size, particle shape, viscosity of fluid, and fluid density, or it is known as a function of Reynolds number, *Re*, which is calculated by the **Equation 4.21**. The drag force coefficient is highly depending on a Reynolds number, while the Reynolds number increases, the drag force coefficient is decreasing as in **Figure 4.9.** In this paper, the most famous estimation equation for drag force coefficient from Haider & Levenspiel (1989),

as shown in **Equation 4.22**, is used for the simulation under the assumption of spherical particle **(Haider A. & Levenspiel O.; 1989)**.

$$Re = \frac{\rho_f |\mathbf{u_f} - \mathbf{u_e^i}| d_e^i}{\mu_f} \tag{4.21}$$

Where, ρ_f is a fluid density, $|\mathbf{u_f} - \mathbf{u_e^i}|$ is a relative velocity between fluid and particle, d_p is a particle diameter, and μ_f is dynamic viscosity of fluid.

$$C_D^i = C_{D,sphere}^i = \frac{24}{Re}(1 + 0.1806Re^{0.6459}) + \frac{0.4251}{1+\frac{6880.95}{Re}} \tag{4.22}$$

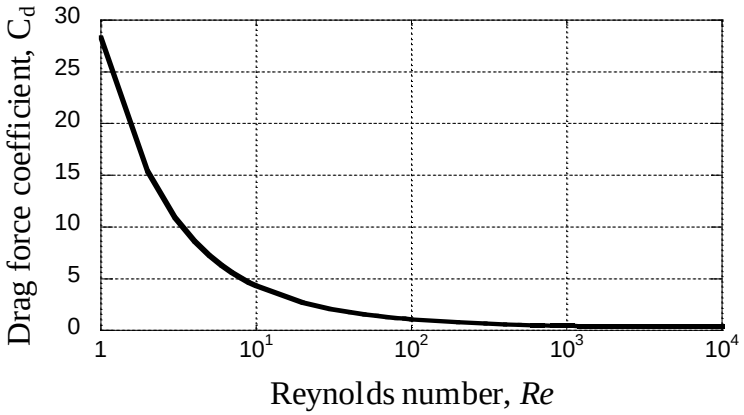

Figure 4.9. The relationship between Reynolds number and drag force coefficient (Haider & Levenspiel; 1989)

The particle velocity, required in the advection equation, would be obtained from the force and velocity equation or momentum balance equation as in **Equation 4.23**.

$$\mathbf{F_D^i} = m^i \dot{\mathbf{u}}_\mathbf{e}^\mathbf{i} \tag{4.23}$$

According to the use of advection form for particle flow, the Finite Difference method (FDM) is used to solve the partial differential equation, hence, the concentration of each particle would be obtained.

The new porosity and permeability are subsequently computed. The erosion or erodible particle transported causes a reduction in the volume of erodible particle, V_e. Therefore, the change in porosity would be depended on the erodible particle volume changed, ΔV_e. According to the current simulation, the calculation does not consider the occurring volumetric strain, therefore, the reduction of erodible soil volume directly

become the increment of porosity, $\Delta\emptyset$, as in **Equation 4.24**. Subsequently, the new porosity would be updated by the **Equation 4.25**.

$$\Delta V_e = -\Delta\emptyset \tag{4.24}$$

$$\emptyset^t = \emptyset^{t-\Delta t} + \Delta\emptyset \tag{4.25}$$

Furthermore, the erodible particle loss in each soil element would calculate from the differences between the residual erodible particle and the erodible particle volume at the previous step as in **Equation 4.26**.

$$\frac{\Delta V_e}{V_T} = \sum_{i=1}^{n} \varphi_i^t - \sum_{i=1}^{n} \varphi_i^{t-\Delta t} \tag{4.26}$$

Where, φ is the erodible particle concentration and obtained from the solving an advection equation by Finite Difference method, subscript n mean the particle group as following the diameter or size, and t shows the current time step, t, or previous step of calculation, $t-1$.

Moreover, the thought of intrinsic flow velocity was concerned which explicitly effect a drag force on erodible particle flow. Therefore, an average flow or Darcy flow velocity obtained from numerical calculation or experimental condition (validation with Lin Ke & Akihiro Takahashi; 2014) must be adjusted as follow in **Equation 4.27 (Fanchi J.R.; 2002)**.

$$\mathbf{u_f} = \frac{\mathbf{u_0}}{\emptyset} \tag{4.27}$$

Where, $\mathbf{u_0}$ is an average flow velocity or Darcy flow velocity, and $\mathbf{u_f}$ is the intrinsic flow velocity which will be used in the drag force calculation.

The particle flow would not be travelling as linear line or the total distance of particle flow is not the same with the length of soil sample or soil mass. In order to predict the distance of actual flow path, the concept of Tortuosity is used. There are several suggestions on Tortuosity for porous media as follow the **Equation 4.28-4.31 (Matyka M., Khalili A. & Koza Z.; 2008)**.

$$T(n) = n^{-p} \tag{4.28}$$

$$T(n) = 1 - p\ln n \tag{4.29}$$

$$T(n) = 1 + p(1-n) \tag{4.30}$$

$$T(n) = [1 + p(1-n)]^2 \tag{4.31}$$

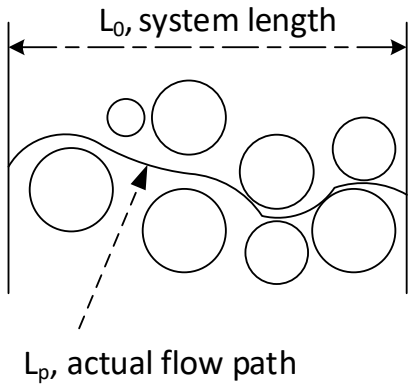

Figure 4.10. The concept of Tortuosity for actual flow path of particle

According to the concept of Tortuosity, the path of flow would not be a straight line but it would be a path that flowing through a void inside porous media as shown in **Figure 4.10**. The element length in the discretization for an advection equation would be adjusted in corresponding with the estimated flow path every calculation step. Therefore, the Tortuosity multiplier is used to extend the size of element for considering the actual particle transported length in each element in the following **Equation 4.32**.

$$dx = T(n)dx_0 \tag{4.32}$$

Where, the dx_0 is the size of the original element as following the domain or the size of soil mass.

4.6 Numerical simulation

According to this erosion scheme, the scheme has newly developed while the validity of analysis is unknown. Therefore, the aim of this section would be the validation of numerical simulation based on force calculation with the experimental result from Ke and Takahashi (2014).

Ke and Takahashi (2014) had conducted an experiment for investigating on suffusion or internal erosion rate with a cylindrical specimen as in **Figure 4.11**. They had used the soil mixture which is composed of silica No.3 and No.8 to be representing the coarse grain and fine grain, respectively. According to the sieve analysis on silica sand, the accumulative of grain size and distribution of grain size are shown in **Figure 4.12**.

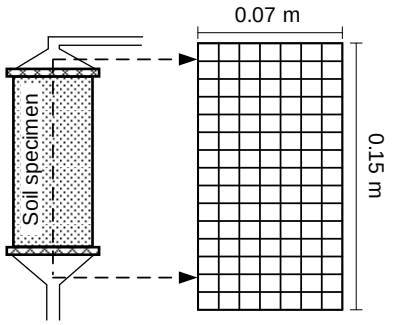

Figure 4.11. The size of specimen from Ke and Takahashi (2014)

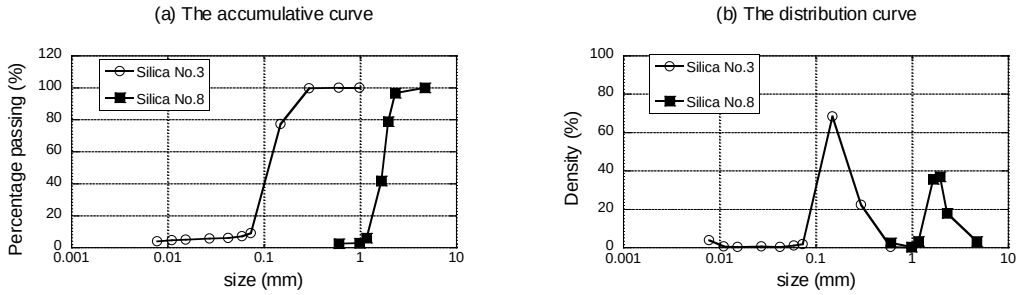

Figure 4.12. The grain size distribution of silica sand No.3 and No. 8 from Ke and Takahashi (2014).

In their experiment, the three mixture of silica sand had been utilized for suffusion testing as follow the proportion in **Table 4.1**. In addition, the necessary parameter such specific gravity of material, dynamic viscosity of fluid or fluid density which are needed to use in the simulation are listed in **Table 4.2** and **Table 4.3** as well.

Table 4.1. The content of soil mixture

	1st mixture	2nd mixture	3rd mixture
fine grain (No.3)	0.35	0.25	0.15
coarse grain (No.8)	0.65	0.75	0.85

Table 4.2. Parameters

Physical property	
Specific gravity of soil, $\boldsymbol{G_s}$	2.645
Fines content of each particle index, $\boldsymbol{\varphi_i^t}$	Distribution curve of grain size (Fig. 4.12)
Initial void ratio, $\boldsymbol{e_0}$	As shown in Table 4.3
Inactive fines content ratio, $\boldsymbol{\varphi_i/\varphi_i^t}$	As shown in Table 4.3
Fluid density (water), $\boldsymbol{\rho_f}$	$1000\ kg/m^3$
Dynamic viscosity, $\boldsymbol{\mu}$	$0.8 \times 10^{-3}\ Pa \cdot s$

Table 2. Contents of soil mixtures

	1st mixture	2nd mixture	3rd mixture
Fine grain (No. 3)	0.35	0.25	0.15
Coarse grain (No. 8)	0.65	0.75	0.85
Initial void ratio, $\boldsymbol{e_0}$	0.64	0.61	0.68
In active fines content ratio	0.73	0.63	0.52

The soil mixture, which was used in the experiment of Ke and Takahashi (2014), is shown in **Figure 4.13** in both distribution curve and accumulative curve from sieve analysis.

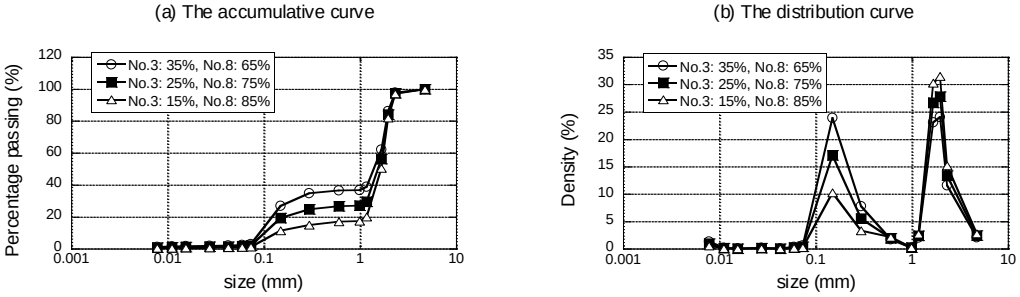

Figure 4.13. The grain size distribution of soil mixture from Ke and Takahashi (2014).

According to the erosion calculation, the range of erodible particle size must be defined, then, the solid-phase can be separated in two group; 1. Erodible particle, and 2. Soil skeleton. According to the Ke and Takahashi (2014) experiment, the opening size of filter was decided as following the maximum of fine grain which is about 1 mm or 0.001 m. Therefore, the size of erodible or fine fraction must be less than 1 mm in accordance

with their experiment condition. According to the aim of performing steady flow, the fluid flow was conditioned as three main stages as shown in **Figure 4.14**. Ke and Takahashi (2014) had targeted the maximum flow rate about 5.17E-6 [m^3/s] with the specimen 0.07 m in diameter at the final stage (stage 3).

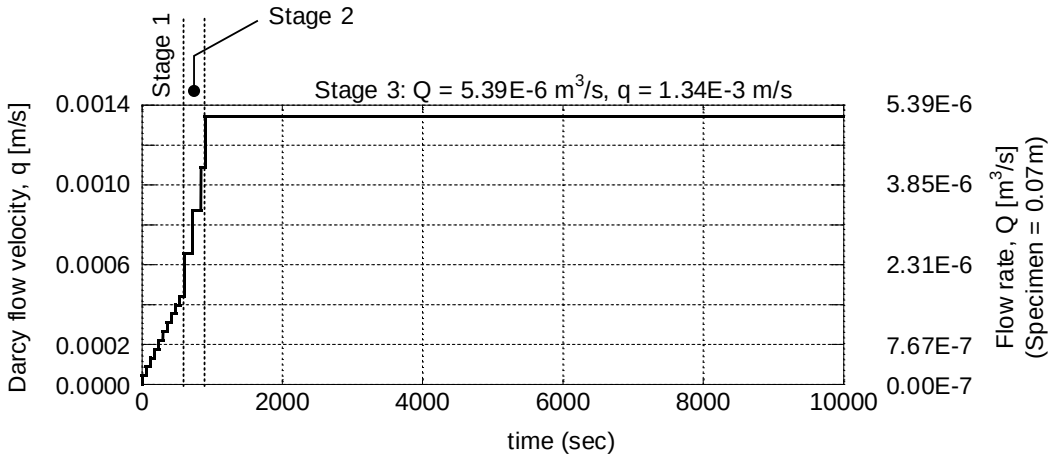

Figure 4.14. The flow rate in the experiment test from Ke and Takahashi (2014).

The experiment result from Ke and Takahashi (2014) is shown that the initiation of erosion is likely occurring at the beginning of stage 3, therefore, the modified fluid flow curve will be applied in the simulation as well in accordance with the initiation of erosion in the experiment as in **Figure 4.15**.

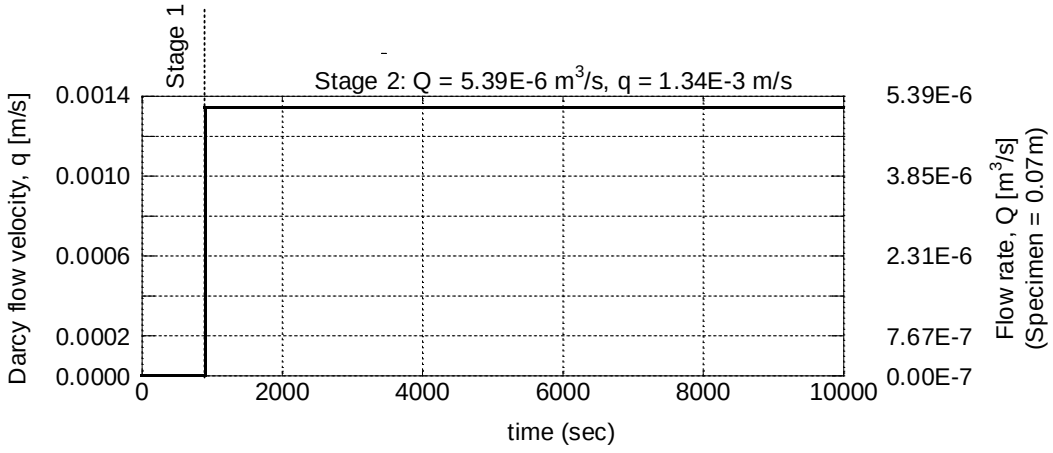

Figure 4.15. The fluid flow for considering an initial erosion.

4.6.1. The simulation with three components of force

4.6.1.1. Analysis background

In this primary simulation, all of three force components (drag force, buoyant force, and gravitational force) will associate in the movement of particle. In addition, the additional parameter which is associating with the force calculation is suggested. According to the force calculation, the summation of force would be divided as two group which is drag force and body force, therefore, two coefficient, effective drag force coefficient, β_D, and effective body force coefficient, β_{BG}, is included in the calculation as shown in **Equation 4.33** in which each coefficient must be in the range of $0 < \beta \leq 1$.

$$\sum \mathbf{F} = \beta_D \mathbf{F_D} + \beta_{BG}(-\mathbf{F_B} + \mathbf{F_G}) \tag{4.33}$$

In this first section of analysis, the study in influence of each force will study with the simplest concept of Tortuosity as in **Equation 4.26** with the p-value equal to unity. According to the experiment result from Ke and Takahashi (2014), the result that will be used to compare is the accumulative fine loss at the downstream.

4.6.1.2. Result and discussion

According to the aim of this first section, the difference coefficient would be used to confirm the influence from each force component. Initially, the effective force coefficient will be replaced by either zero or unity to show three different cases of simulation.

The first simulation is shown as in **Figure 4.16** in which the coefficient of effective force for both drag force and body force are unity, $\beta_D = 1, \beta_{BG} = 1$. The simulation result show that erodible particle is quickly came out from the soil sample even before fluid flow was applied. According to this result, the body force including gravitational force and buoyant force likely to apply excessive force on the erodible particle. Once, the body force is discussed, the force that is really induce the fast movement of particle is gravitational force. In example, if there is no acceleration on the fluid flow, the result of summation between gravitational force and buoyant force is $\rho_s V_s \mathbf{g}(\rho_s - \rho_f)$. Hence, the body force (gravitational force and buoyant force) dominated in this simulation while the drag force could not show any influence.

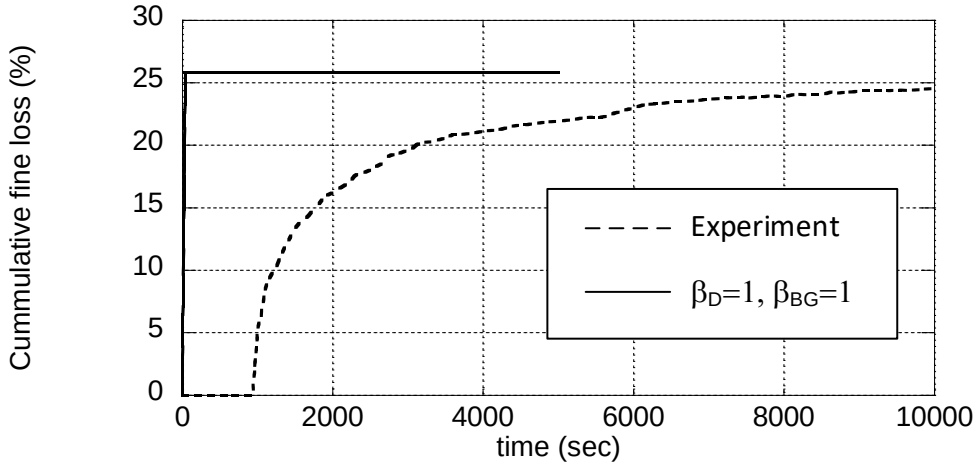

Figure 4.16. The comparison between an experiment with the simulation of $\beta_D = 1, \beta_{BG} = 1$

The previous simulation has shown that the consideration all of the forces do not give a promising result. Therefore, the simulation which separately considered body force and drag force might be necessary. Therefore, the other simulation might be needed to confirm the fine loss due to each force components. The calculation will be separated as two cases which considers only drag force or body force.

The case of consideration only body force is shown in **Figure 4.17** where $\beta_{BG} = 1$ and $\beta_D = 0$ to show the erosion influenced by only body force. The result shows that the erosion behavior speed is still very high as seen from the steep slope of the cumulative fine loss. According to this result and previous result as in **Figure 4.16** and **Figure 4.17**, respectively, it could be confirmed that the result from body force generate immoderate force on a particle which could rarely observe an influence from drag force. Hence, the next simulation will just only consider the erosion due to drag force in which $\beta_{BG} = 0$.

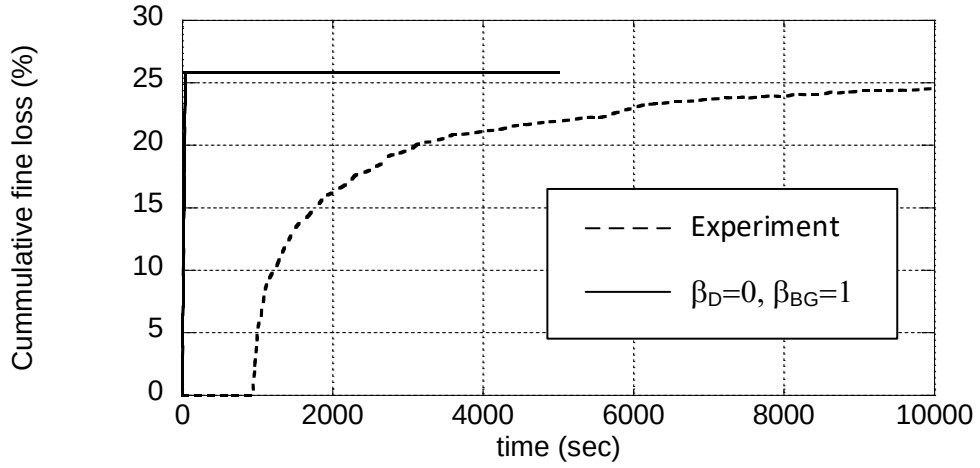

Figure 4.17. The comparison between an experiment with the simulation of $\beta_D = 0, \beta_{BG} = 1$

Conversely, the simulation of erosion undergoing with only drag force is conducted as well as shown in **Figure 4.18**, in which $\beta_D = 1, \beta_{BG} = 0$ were assigned to represent only drag force in the force calculation. The simulation result was clearly showing that the erosion rate is still higher than experiment, while the erosion rate seemly slower than the case of consideration in body force. However, the simulation result could show more promising behavior in comparison with previous simulation. It also can be implied that drag force tends to exert a proper force on the erodible particle. According to the cumulative fines loss data from experiment, erosion rate is basically calculated by the ratio between different fines loss and time increment, $erosion\,rate = \left(\frac{current\ fines\ loss - previous\ fines\ loss}{current\ time - previous\ time}\right)$. Hence, the erosion rate of the simulation has been examined and shown in **Figure 4.19**. The erosion rate result shows the difference between the beginning of erosion between both experiment and simulation with only drag force. The erosion rate in current simulation is relatively higher than the experiment, especially at the beginning of the test, while after around 1200 second the erosion rate seems to be similar with the experiment.

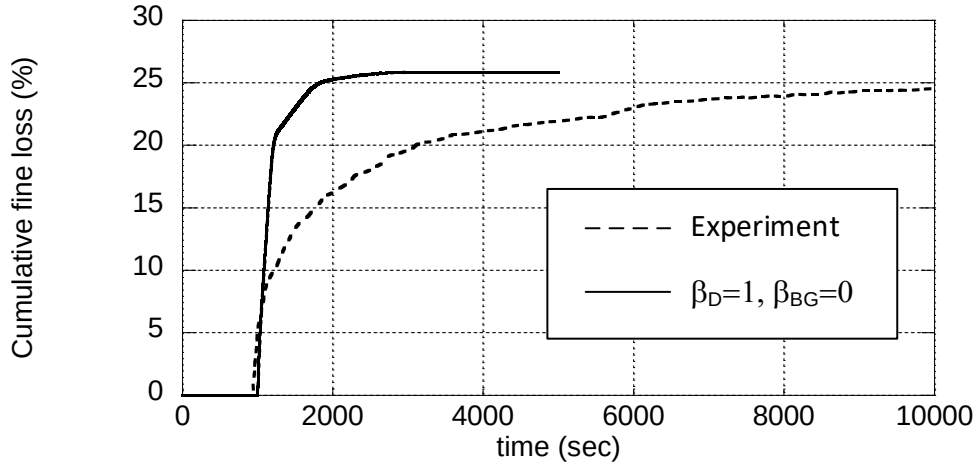

Figure 4.18. The comparison between an experiment with the simulation of $\beta_D = 1, \beta_{BG} = 0$

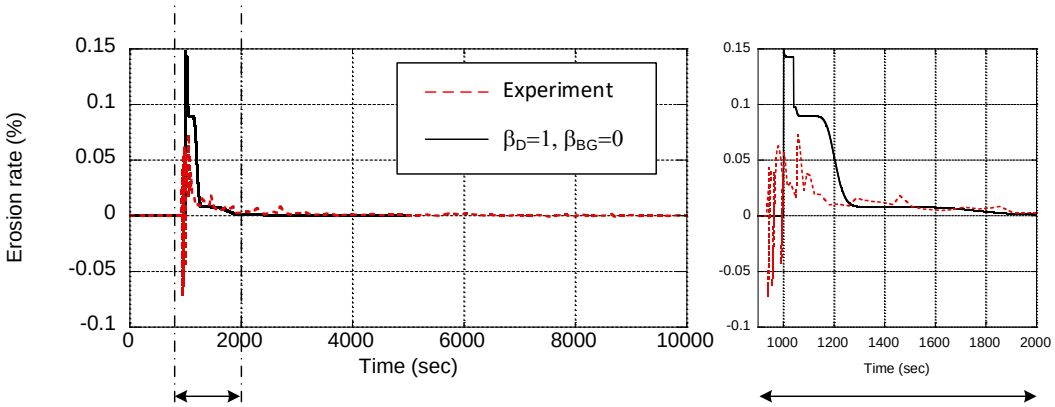

Figure 4.19. The erosion rate from both experiment and numerical simulation with drag force

4.6.2. The simulation with a theory of buoyancy-gravitational force ratio

4.6.2.1. Analysis background

According to the previous study about particle segregation, the larger particle tends to separate from surrounding particle. The large particle dispersing in dense granular media is normally encountering with lift force as shown in **Figure 4.20**.

Therefore, the particle with larger size tends to segregate or separate from the surrounding particle. Nevertheless, the previous simulation of discrete particle method also reported that the force associating with particle in granular media is not only gravitational force and buoyant force but lifting force as well **(van der Vaart K., van Schrojenstein Lantman M.P., Weinhart T., Luding S., Ancey C. & Thornton A.R.; 2018)**. Lift force is basically exerting on particle intruder or particle with larger size, and responsible for segregation in granular media. In addition, the previous study also shows the buoyant force in granular media and lift force in the ration of gravitational force as shown in **Figure 4.21**.

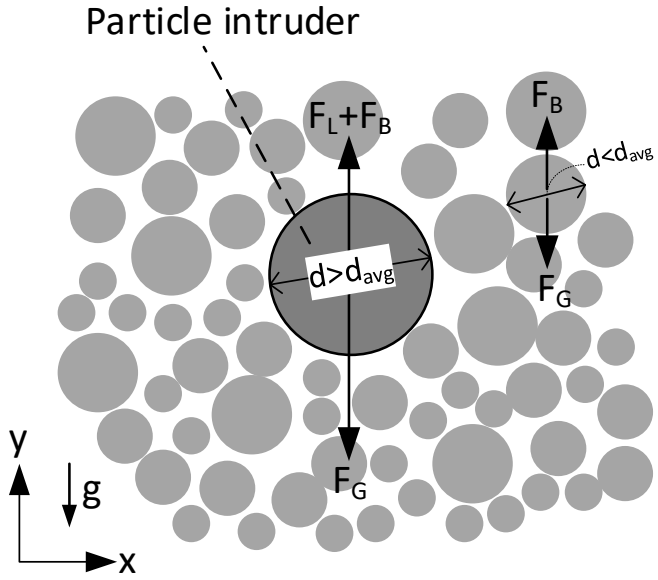

Figure 4.20. The schematic of force diagram of particle intruder concept

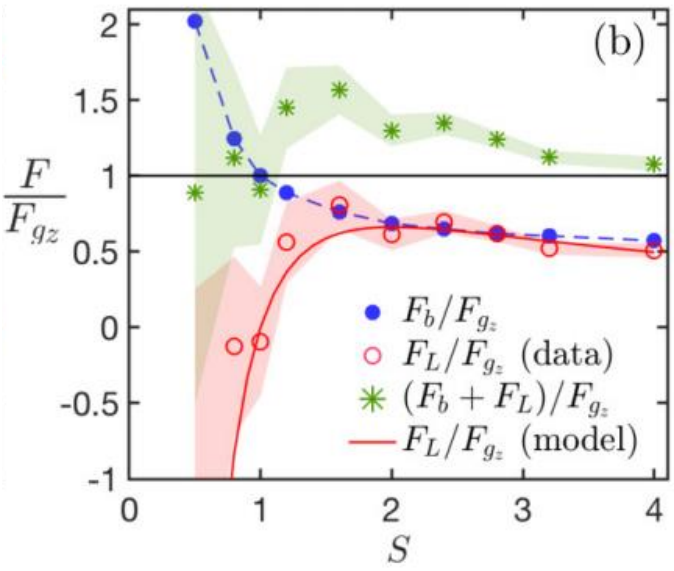

Figure 4.21. The ratio of buoyant force and lift force in granular media (van der Vaart K., van Schrojenstein Lantman M.P., Weinhart T., Luding S., Ancey C. & Thornton A.R.; 2018)

According to the erosion, it is not a single particle in fluid system but there are many of particle within the same system. Therefore, in this section, the simulation that tried to include an effect from particle in granular media would be conducted. Fortunately, there is a theoretical prediction method for a buoyant-gravitational force ratio, $\frac{F_B}{F_G}$. Conversely, there is still no theoretical calculation in lift-gravitational force ratio, $\frac{F_L}{F_G}$., for particle intruder in the granular media. However, the lifting force might be assumed as constant ratio with gravitational force in which the particle ratio is larger than unity.

The calculation of buoyant force in granular media is recently theoretically explained by Kumar A., Khakhar D.V., Tripathi A. (2019). The buoyant-gravitational force ratio could be simply calculated in the function of total solid fraction, $\emptyset$, and partial molar volume, $\tilde{V}_i$, as shown in **Equation 4.34**.

$$\frac{F_{By}}{F_{Gy}} = \frac{\emptyset \rho_p \tilde{V}_i g_y}{\rho_p V_i g_y} = \frac{\emptyset \tilde{V}_i}{V_i} \tag{4.34}$$

Moreover, partial molar volume is corresponding with pressure, volume, temperature, and the number of particles as follow **Equation 4.35**.

$$\tilde{V}_i = \left(\frac{\partial V}{\partial N_i}\right)_{P,T,N_j} \tag{4.35}$$

where, N_i is number of species i, V is volume, P is pressure, T is temperature, and N_j is number of particles of other species.

According to the requirement of $\tilde{V}_i$ in the **Equation 4.35**, the equation of state for binary mixture of hard sphere as in shown in **Equation 4.36** has been used to solve a partial molar volume.

$$P = nT + \left(\frac{2}{3}\right)\pi T \sum_{i=1}^{2}\sum_{j=1}^{2} \mathcal{G}_{ij} R_{ij}^3 n_i n_j \tag{4.36}$$

Where, i and j represent for each species of particle in the system (considering two types of particle in the system), $R_{ij} = R_i + R_j$ while R_i is the radius of particle i, $n = n_i + n_j$ in which n_i is the density of particles i, $n_i = \frac{N_i}{V}$, and $\mathcal{G}_{ij}$ is a pair correlation function which calculated as in **Equation 4.37**.

$$\mathcal{G}_{ij} = \frac{1}{1-\emptyset} + \frac{3R_iR_j\epsilon}{R_{ij}(1-\emptyset)^2} + 2\left(\frac{R_iR_j}{R_{ij}}\right)^2\left(\frac{\epsilon}{1-\emptyset}\right)^2 \tag{4.37}$$

Where, $\emptyset = \frac{N_1V_1+N_2V_2}{V}$ is the particle fraction, and $\epsilon = \frac{n_1V_1}{R_1} + \frac{n_2V_2}{R_2}$ is a total density of particle.

After, theoretically solved, the solution can be shown as in **Equation 4.38 (Kumar A., Khakhar D.V., Tripathi A.; 2019)**.

$$0 = 1 - \frac{(N_1+N_2)\tilde{V}_2}{\tilde{V}_i} + \left(\frac{2}{3}\right)\pi V\left(\frac{\partial \mathcal{G}_{11}}{\partial N_2}R_{11}^3 n_1^2 + \frac{\partial \mathcal{G}_{22}}{\partial N_2}R_{22}^3 n_2^2 + 2\frac{\partial \mathcal{G}_{12}}{\partial N_2}R_{12}^3 n_1 n_2\right) + \left(\frac{4}{3}\right)\pi(\mathcal{G}_{12}R_{12}^3 n_1 + \mathcal{G}_{22}R_{22}^3 n_2) - \left(\frac{4}{3}\right)\pi\tilde{V}_2(2\mathcal{G}_{12}R_{12}^3 n_1 n_2 + \mathcal{G}_{22}R_{22}^3 n_2^2 + \mathcal{G}_{11}R_{11}^3 n_1^2) \tag{4.38}$$

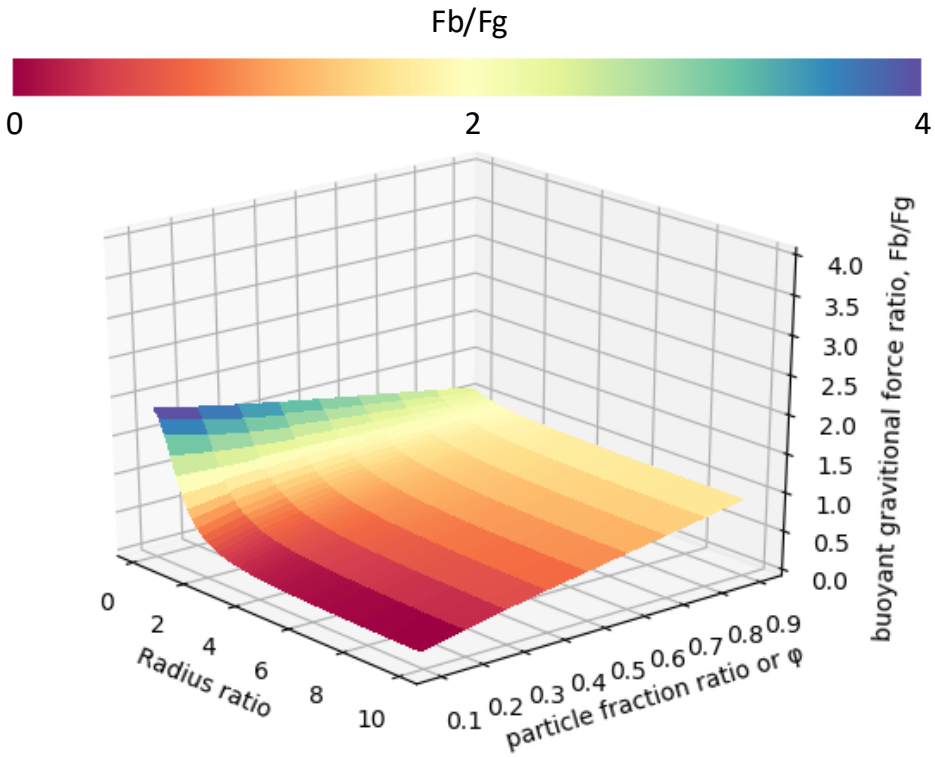

Figure 4.22. The buoyant-gravitational force ratio with the variation in particle fraction ratio

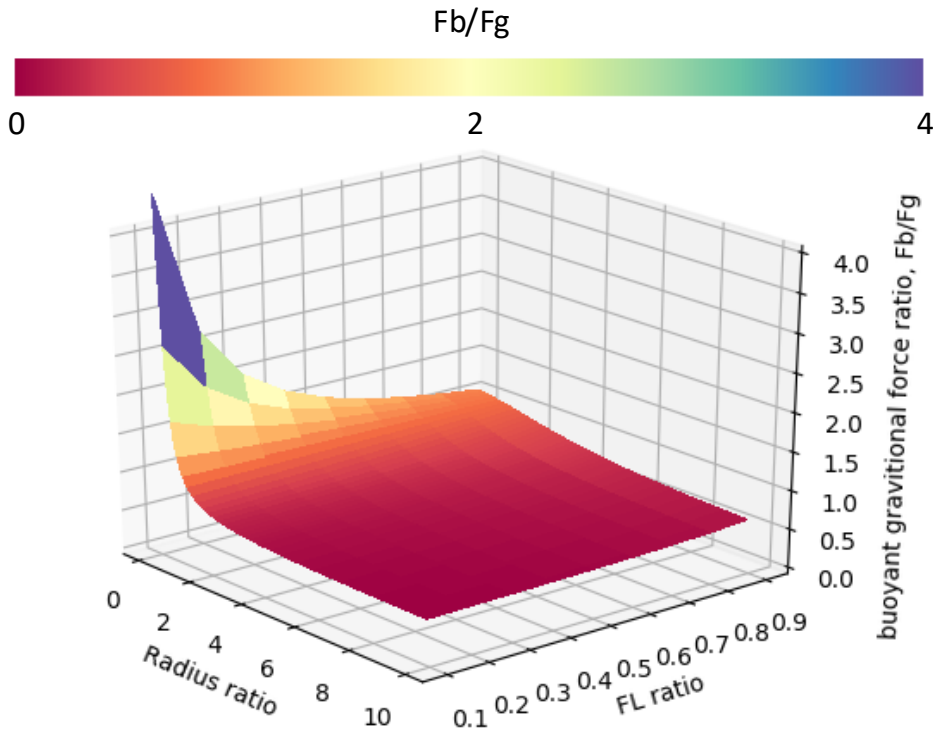

Figure 4.23. The buoyant-gravitational force ratio with the variation in concentration of large particle

According to the solution of partial molar volume, this could be known that it is a function of radius ration, particle fraction or particle intruder concentration. Therefore, the calculation of the buoyant-gravitational force ration is calculated to shown the influence from radius ratio, $\frac{R_2}{R_1}$, particle fraction, $1-\emptyset$, and concentration of large particle, FL, as shown in **Figure 4.22.** and **Figure 4.23**.

4.6.2.2. Result and discussion

The erosion simulation including an effect from particle intruder is considered in this section, therefore, the simulation is similarly conducted as the previous section by using an effective force coefficient. Nevertheless, the force calculation in this section would not be same with the previous one, the summation of force also includes lift force as shown in **Equation 4.39**. According to the previous study on particle intruder, the lift force on a particle is almost constant when the size ratio become higher in accordance with **Figure**

4.21. Hence, the lift force which could not still theoretically calculated, the assumption that the lift force is a constant value when radius ratio is greater than 1 was used as shown in **Equation 4.40**.

$$\sum \mathbf{F} = \beta_D \mathbf{F_D} + \beta_{BGL}(-\mathbf{F_B} + \mathbf{F_G} - \mathbf{F_L}) \tag{4.39}$$

$$\frac{\mathbf{F_L}}{\mathbf{F_G}} = \begin{cases} \omega, & \frac{R_2}{R_1} \geq 1 \\ 0.0, & \frac{R_2}{R_1} < 1 \end{cases} \tag{4.40}$$

According to the previous study, the lift-gravitational force ratio is about 0.5 in accordance with the **Figure 4.21**. Therefore, this simulation would try a several value of ω which represents for lifting force calculation. The result as in **Figure 4.24** shows an erosion with different value of ω within the range $[0.3,0.5]$. The simulation shows that when the ω is higher than 0.4, the effect of body force cause a slow erosion. Because, the summation of lift force and buoyant force is always greater than gravitational force. Conversely, while applying a smaller value of ω could make an erosion quickly developed in accordance with the gravitational force become dominant. Moreover, the reduction of influence from body force is also applied in this calculation, while the β_{BGL} is become smaller the erosion seems to be slower but still very high in comparison with experiment. Therefore, particle intruder concept might not be suitable for an erosion mechanism in which the particle in the system may not be dense enough to be considered as a system of particle. In addition, the body force including lift force, buoyant force, and gravitational force might not be influence on the erodible particle because the small particle or erodible particle may just be moving along the soil skeleton surface in which body force can be ignored.

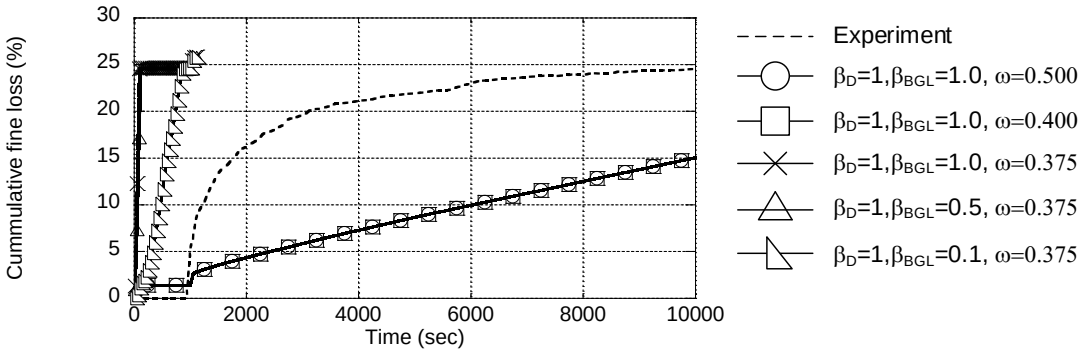

Figure 4.24. The simulation of erosion with the concept of particle intruder

4.6.3. The simulation of erosion induced by drag force

4.6.3.1. Analysis background

According to the two previous simulations, the result was showing that the influence from body force is relatively high and cause of quick erosion. The erosion from gravitational effect might not play a big role in the erosion mechanism in accordance with the existence of soil skeleton. In general, soil skeleton will not move due to the seepage flow, hence, when the fine particle encounter with soil skeleton the body force tend to be equilibrium in correspondence with the reaction force from the soil skeleton. Therefore, the reason behind this behavior might be the particle is generally moving on the surface of soil skeleton as shown in **Figure 4.25**. The soil skeleton could sometime be an obstacle for erodible particle flow, especially on the flat surface.

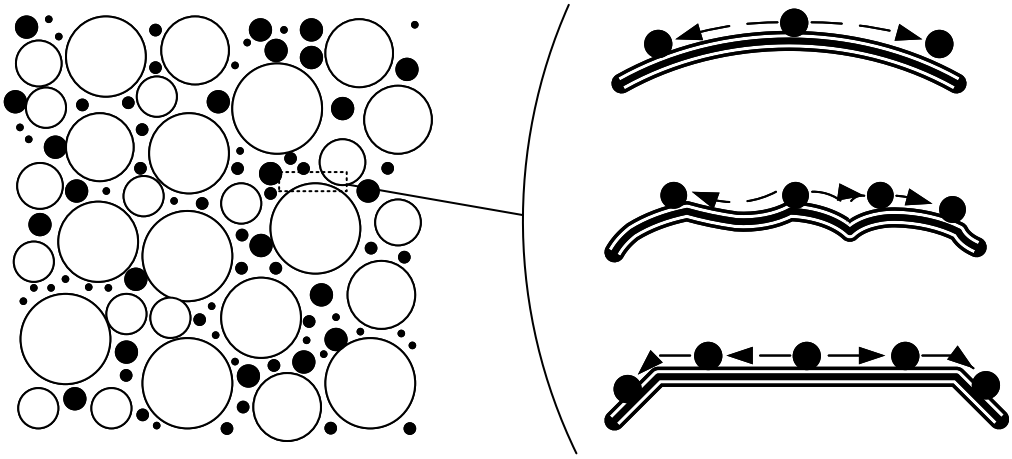

Figure 4.25. The particle flow on the soil skeleton surface.

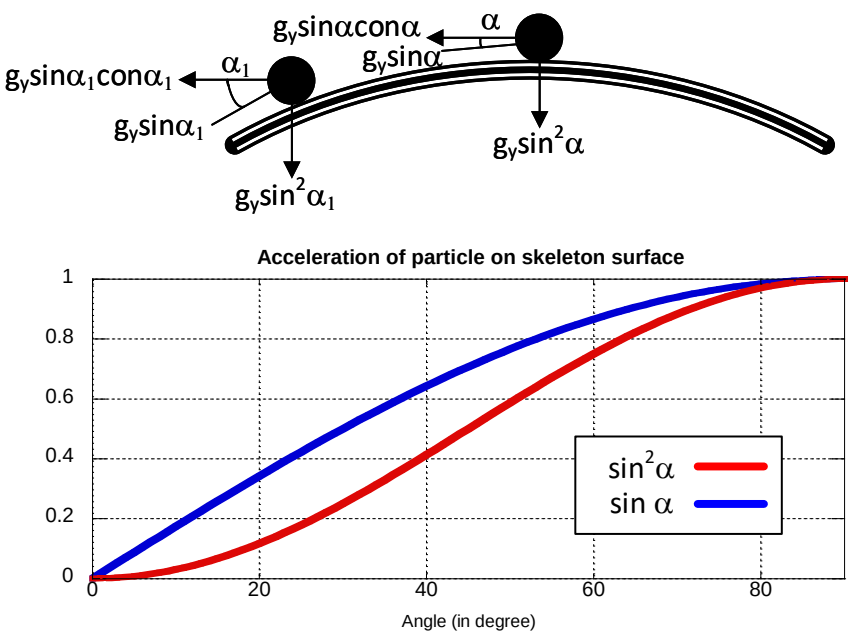

Figure 4.26. The value of $(\sin\alpha)^2$ to show the downward acceleration component

Moreover, the basic calculation of the acceleration on fine particle on the soil skeleton surface is shown to emphasize the reason that gravitational force generates less effect on the particle movement in porous media. The reduction of gravitational acceleration is a function of angle between the horizontal line and moving direction as shown in **Figure 4.26**. In addition, the calculation shows that the effect of gravitational acceleration is very small while the angle is small.

4.6.3.2. Result and discussion

In this section of simulation, the consideration only drag force will be applied to show an erosion rate in corresponding with the reason of neglect in body force. Therefore, the summation of force is reduced to be an **Equation 4.41**.

$$\sum \mathbf{F} = \beta_D \mathbf{F_D} \tag{4.41}$$

According to the existence of soil skeleton and the effect from particle clogging, an applying total amount of drag force on particle flow might not be a good idea which could cause an excessive force on the particle flow as it shown previously. Therefore, the reduction of the drag force applying on the particle flow is used. The simulation in this section will be conducted with various value of β_D which should be in the range of $(0, 1]$. **Figure 4.27** shows the cumulative fine loss from each simulation different in the effective drag force coefficient. According to the result, the simulation result is lower than the experiment at the beginning while $\beta_D = 0.2$ was used, however, all the result still generates a higher rate of erosion than the experiment. The result in this section could also refers to that the particle flow path might be still short, therefore, the particle is quickly coming out from the sample. Hence, the further study in the following section will be about the utilization of different tortuosity concept to consider the length of particle flow path.

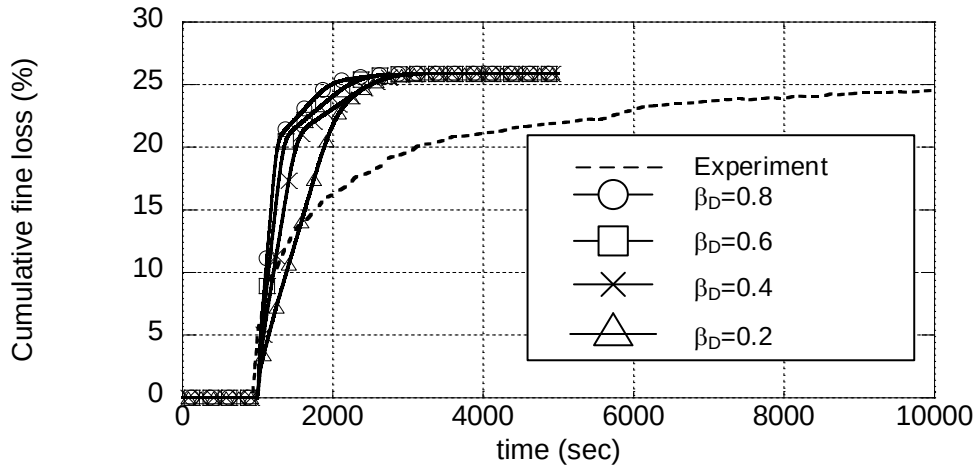

Figure 4.27. The simulation of erosion effected by drag force

4.6.4. The simulation of erosion with difference tortuosity concept

4.6.4.1. Analysis background

Tortuosity is the ratio between and actual path length and the length of domain as mentioned before. The actual path length is directly related with the erosion rate, because the particle would take more time to come out at the downstream in the longer path. In addition, there are several suggestions on the tortuosity concept as following **Equation 4.26-4.29**. Therefore, in this section is trying to show a difference behavior of erosion under a difference concept of tortuosity.

4.6.4.2. Result and discussion

The length of particle flow path is difficult to estimate in microscopic scale due to the randomness of particle arrangement and its shape. Hence, the concept of tortuosity which is widely used in several field will be applied in this simulation to estimate the length of flow path. The simulation in this part aims to show the difference behavior while applying a difference function of tortuosity. The different function of tortuosity will represent the different length of particle flow path, moreover, the higher p-value in tortuosity function stand for the flow path is longer under the same porosity. In addition, the simulation in this section was considered with only drag force and its coefficient, β_D, is about 0.4 which could be seen in **Figure 4.27**.

The first calculation in this section performed the simplest model of tortuosity as shown in **Equation 4.26**. Moreover, the variation of p-value in the function has been done as well in the range $\left[\frac{1}{3}, 2\right]$ as shown in **Figure 4.28**. The result obviously shows that the erosion rate is much closer to the experiment when the p-value become larger. Because, the higher number of p-value leads to the higher tortuosity, therefore, the fine particle is taking more time to come out at the downstream.

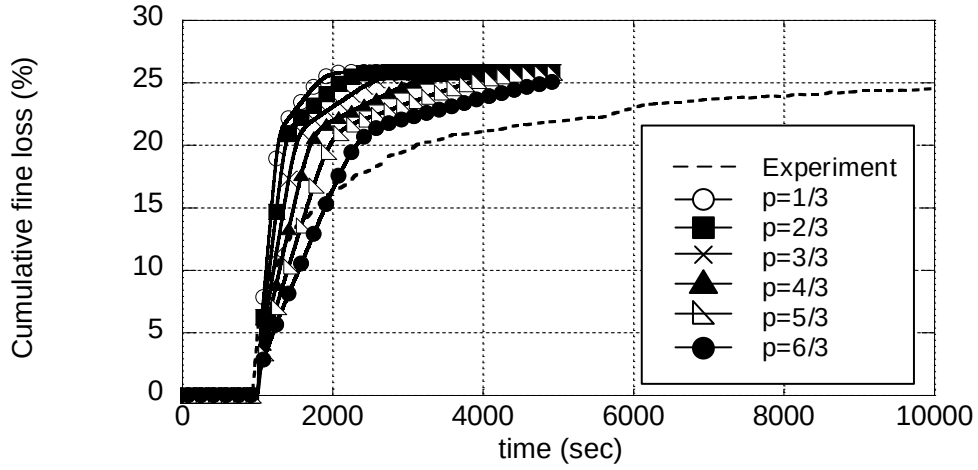

Figure 4.28. The simulation with 1st concept of tortuosity, $T(\phi) = \phi^{-p}$

Similarly, the simulation has be done by the tortuosity concept as shown in **Equation 4.27**. Nevertheless, this tortuosity model could not give much difference at each p-value, which the erosion rate is still much higher than the experiment as shown in the **Figure 4.29**.

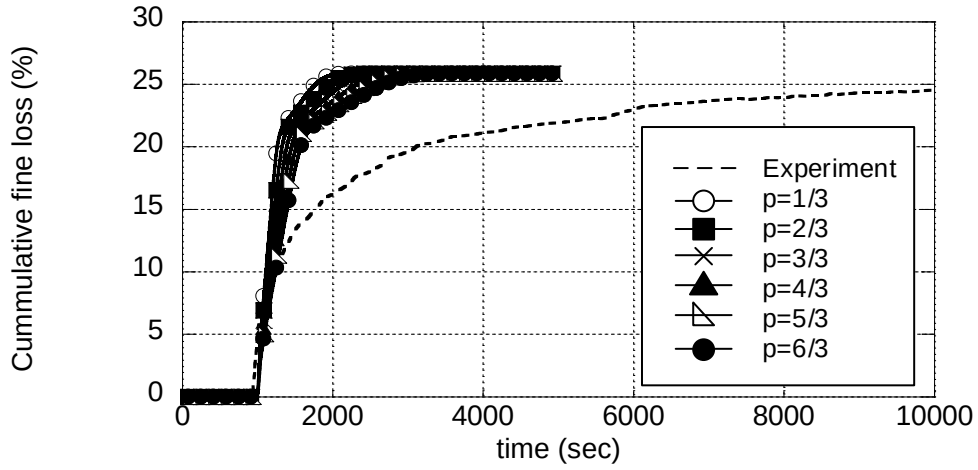

Figure 4.29. The simulation with 2nd concept of tortuosity, $T(\phi) = 1 - pln(\phi)$

The simulation in **Figure 4.31** and **Figure 4.32** are conducted with the same expression in tortuosity, while the **Figure 4.30** shows a result tortuosity concept as in **Equation 4.30**, it also shows that the erosion rate is slightly change with various p-value. While the concept from **Equation 4.31** which is a square of **Equation 4.30** could show a better result as in **Figure 4.32**.

Finally, the result from each concept may be concluded that the tortuosity model from **Equation 4.28** and **Equation 4.31** generate a promising result, especially, the **Equation 4.28**.

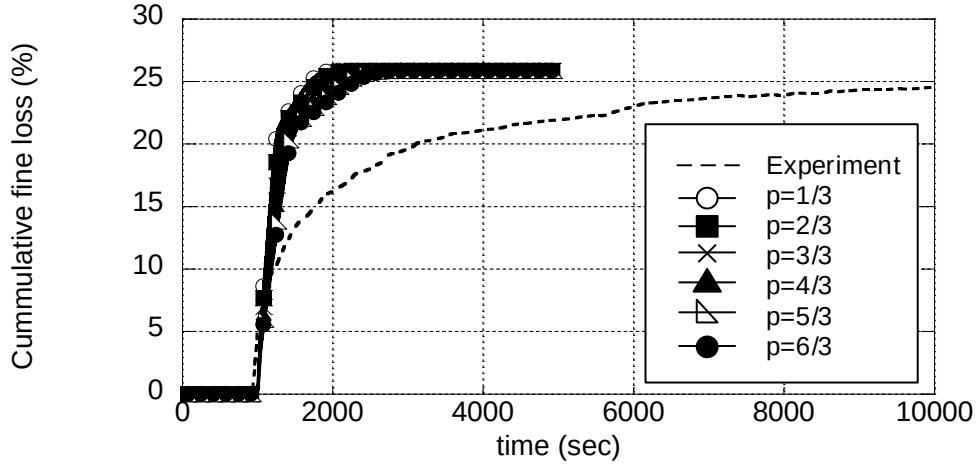

Figure 4.30. The simulation with 3rd concept of tortuosity, $T(\phi) = 1 + p(1-\phi)$

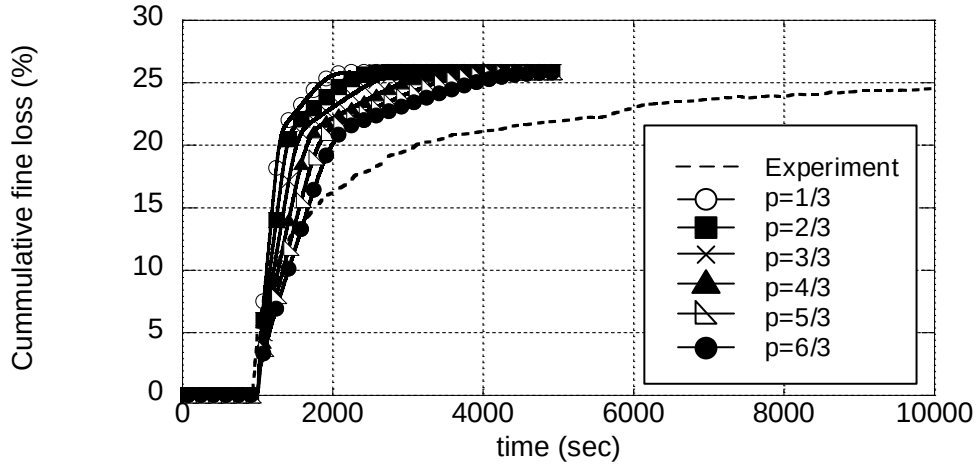

Figure 4.31. The simulation with 4th concept of tortuosity, $T(\phi) = [1 + p(1-\phi)]^2$

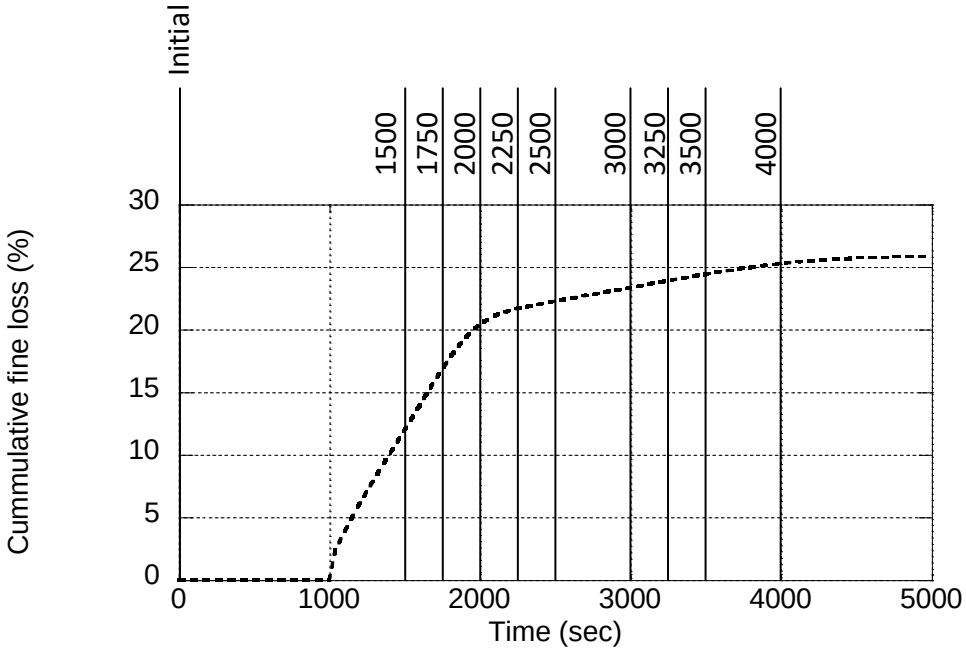

Figure 4.32. The erosion result from the first concept of tortuosity with p=5/3

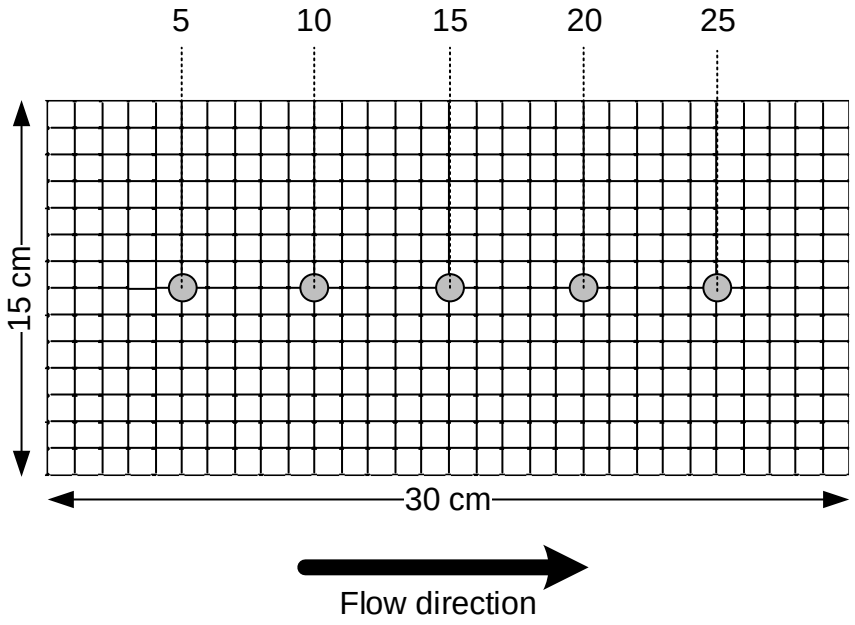

Figure 4.33. The location of observation of particle size distribution

Furthermore, the simulation with only drag force with the first concept in tortuosity as shown in **Figure 4.28** will be calculated further to show other behavior such porosity distribution at each difference in both time steps and locations. The series of time

steps was chosen as shown in **Figure 4.32** to show the contour map at each point of time. The results which will be further shown is the distribution of soil grain at difference location as in **Figure 4.33**. And the result of each distribution at difference locations are shown as following **Figure 4.34 – Figure 4.38**. According to the grain size distribution, it is obviously shown that the particle of erodible at the beginning is nearly no erosion at the location close to upstream as shown in **Figure 4.34**. Conversely, the erosion is occurring at the downstream firstly or the erodible particle starts to move out from the soil mass before the erosion at other locations which could clearly observed in the **Figure 4.38**.

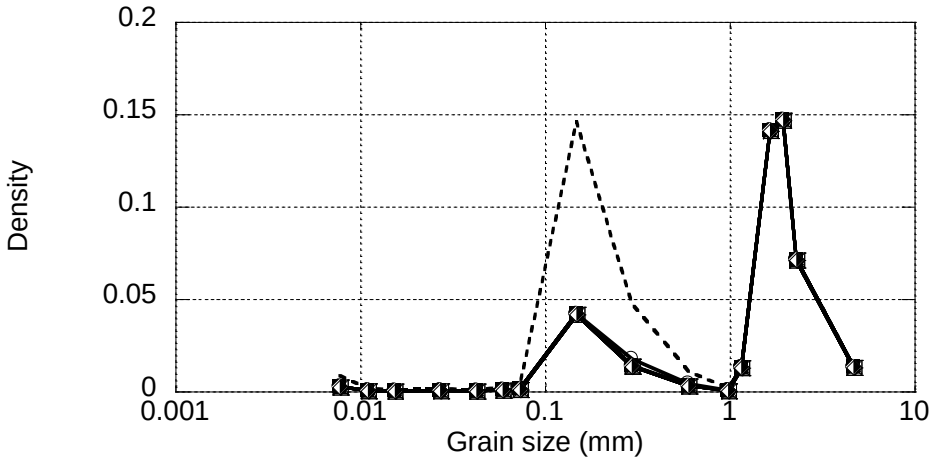

4.34. The particle size distribution at 5 cm. from the upstream

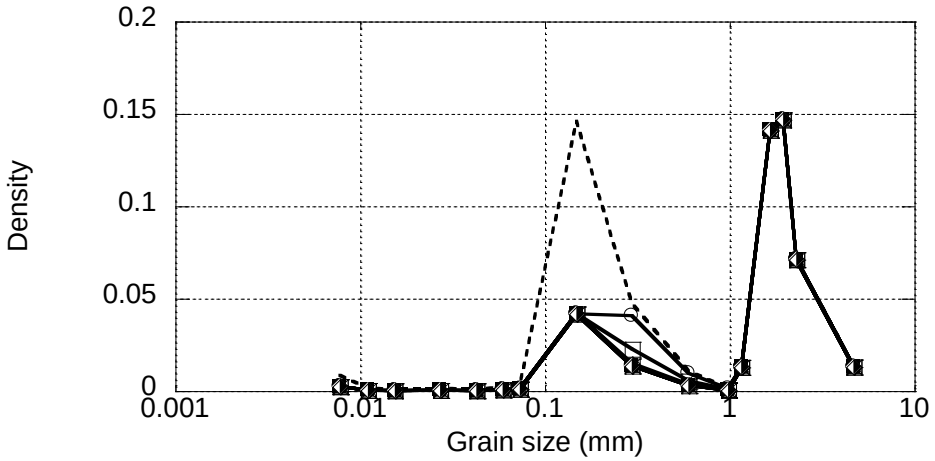

Figure 4.35. The particle size distribution at 10 cm. from the upstream

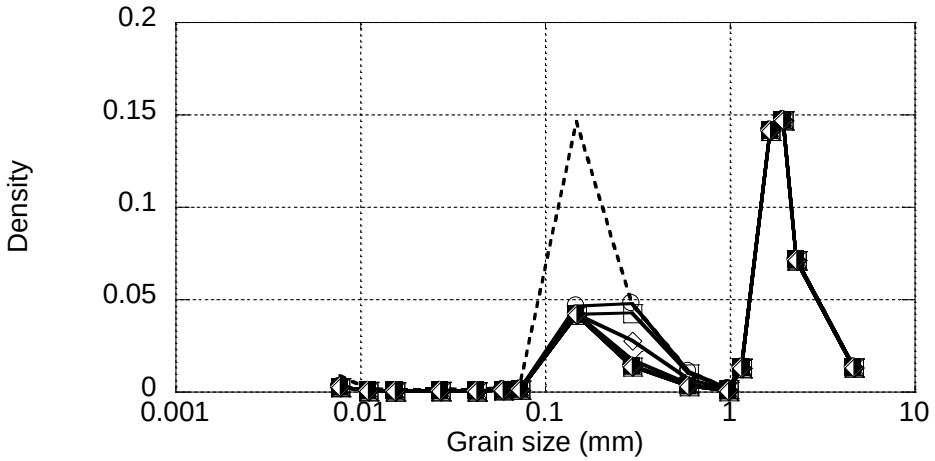

Figure 4.36. The particle size distribution at 15 cm. from the upstream

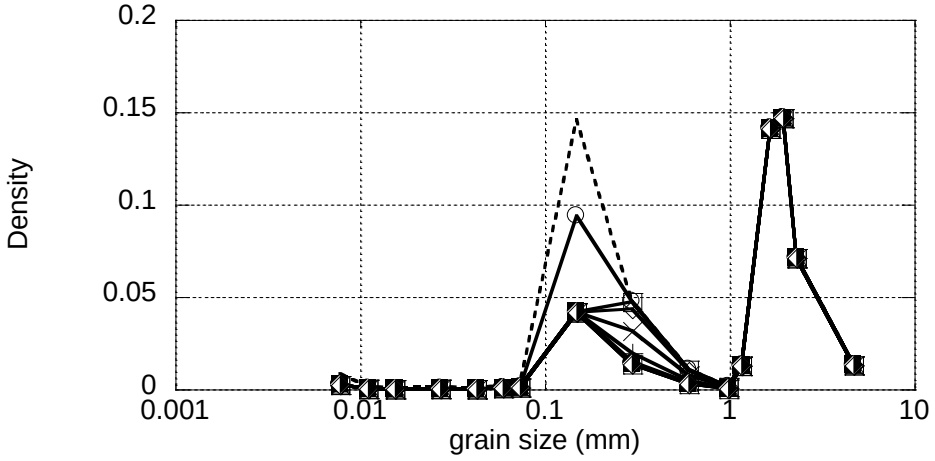

Figure 4.37. The particle size distribution at 20 cm. from the upstream

The representative size of erodible particle was also picked to shown an erosion rate as shown in **Figure 4.39**. The fineness particle, 0.0078 mm, eroded faster, while the biggest erodible particle, 0.9883 mm, tends to come out from soil mass slower than other sizes. This behavior could show that even finer particle is encountering with lower drag force but the acceleration might be grater due to the smaller mass. On the other hand, it could be said that the force-mass ratio in small particle is greater than large particle.

According to the erosion, the porosity is highly depended on the erosion because

the erosion is removing the erodible particle, hence, the void space inside porous media become larger. Therefore, at the last section, the contour of porosity at each time step is shown as in **Figure 4.40**.

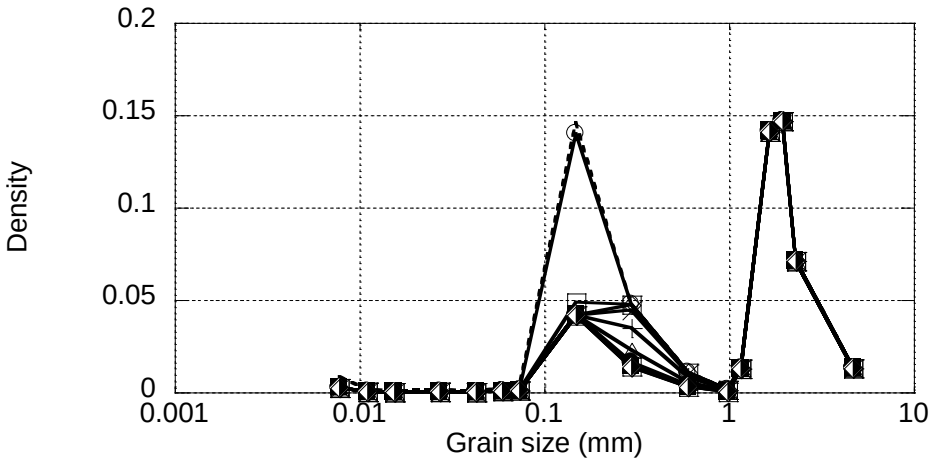

Figure 4.38. The particle size distribution at 25 cm. from the upstream

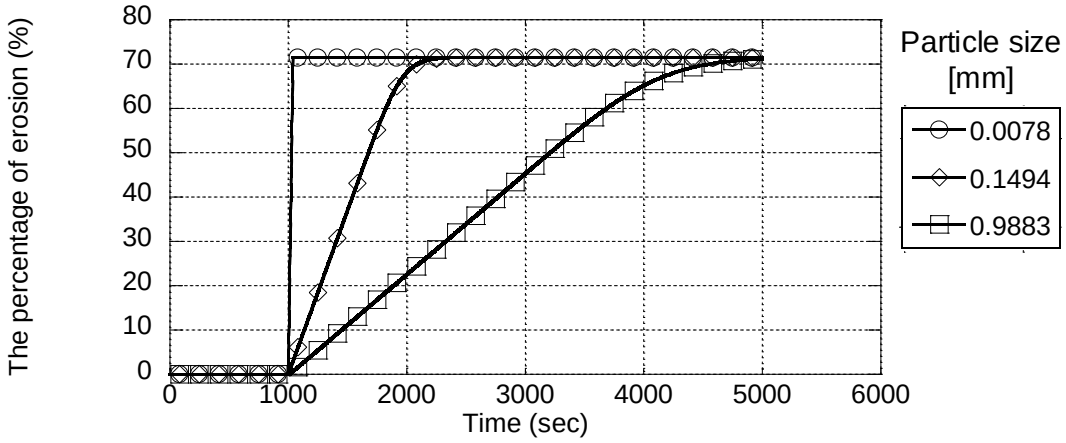

Figure 4.39. The erosion from each three representative sizes of particle

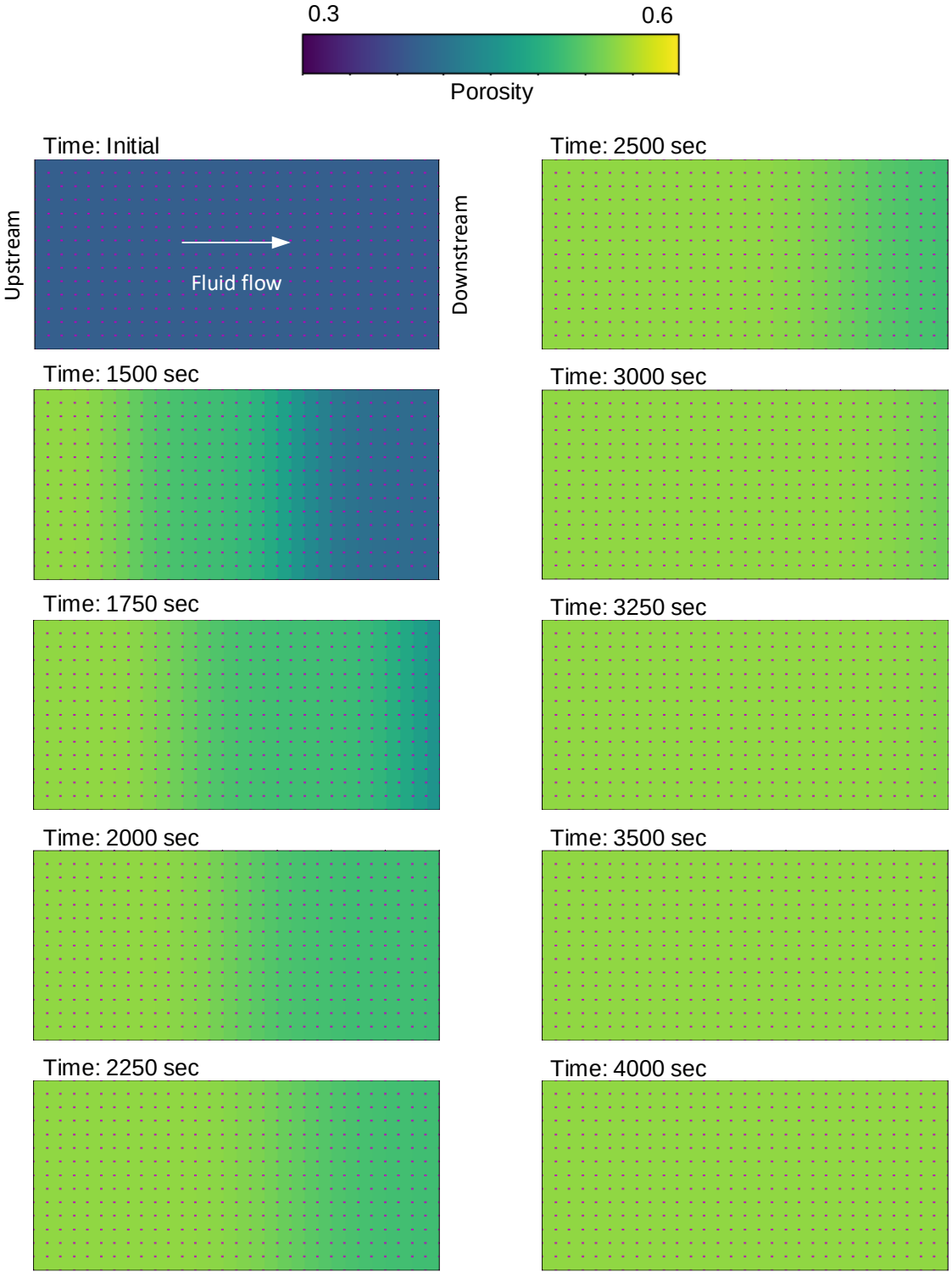

Figure 4.40. The porosity distribution at each time

4.7 Conclusion

The development of erosion model in this research is an estimation of erodible particle movement based on momentum balance equation or force equilibrium on particle. According to the erosion simulation, several attempts has been tried to clarify the force component which will be used for the erosion calculation.

The first simulation which was done by employing all of three main force (drag force, buoyant force, and gravitational force) showed a fast erosion rate in comparison with the previous research experiment result. The acceleration from each from might be divided as two main group which are acceleration from body force and drag force. According to the body force component, the summation of both buoyant force and gravitational force, $\mathbf{F_G} + \mathbf{F_B} = (\rho_s - \rho_f)V_s\mathbf{g} - \rho_f V_s(\mathbf{a_f})$, is normally much higher than the drag force, additionally, the gravitational force is always control the direction in accordance with the specific gravity of particle is more than unity ($S.G._{soil} > 1$). Therefore, when the simulation is complied with three force components, the body force is always dominating in the simulation.

The subsequence simulation was done with only drag force component under the assumption that the body force might not play a big role in granular flowing in porous media. Because the soil skeleton might be being as an obstacle for granular free falling, the erodible particle or fine particle could be stay still on the soil skeleton surface while there is no seepage flow. In addition, the result shows that the correlation between experimental data and simulation data is quite better than considering all of three force components. Therefore, it might be concluded that the particle flow in porous media is mainly dominated by drag force.

Further analysis including lift force could not show a promising result in which the erosion rate could be very quick or slow. The reason behind this mechanism is that the additional lift force and buoyant force are still a function of gravitation force which is relatively high in comparison with drag force. Therefore, the increment in lift force and buoyant force component could reduce the gravitational force effect, however, these forces adjustment is very sensitive due to the massive value. Even if the calculation of buoyant force could be computed by previous analytical solution, but the estimation of lift force is still very rough. Since, there is still no suggestion in analytical solution of

particle flow in granular media but only result from discrete particle simulation. Therefore, the simulation scheme that will be used in the following chapter will be associated with only drag force, as shown in **Figure 4.41**, in which this scheme could show the most promising data in accordance with the experimental data.

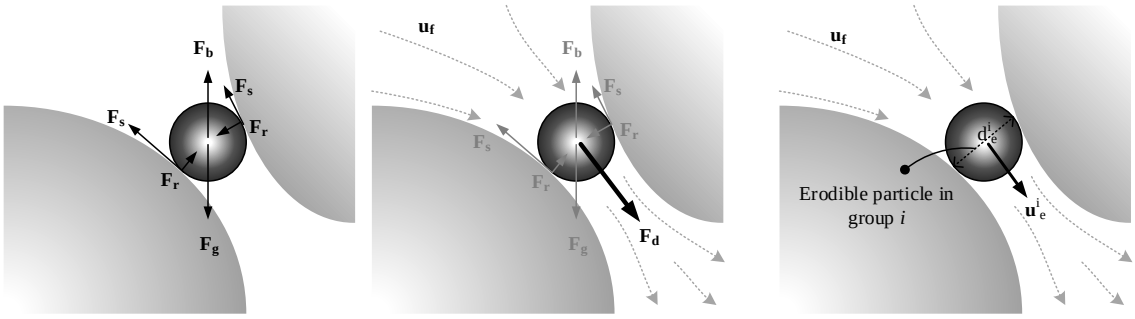

(a) Initial condition (equilibrium of concurrent forces)

(b) Fluid flow (additional drag force)

(c) Erodible particle

Figure 4.41. The force diagram on erodible particle

Finally, the tortuosity concept which would extent the flow path for each element is studied with various concepts. The difference tortuosity function gave a difference characteristic of particle flow. According to the tortuosity, normally it is a function of porosity, in addition, the tortuosity become higher or erosion could be faster with same particle flow velocity, when the porosity is increasing.

Moreover, the additional result of porosity changes and particle size distribution at several location in the soil sample show that the erosion starts from the upstream side and continue to the upstream. Also, the finer particle tends to move out from the soil mass faster than bigger size of particle.

Chapter 5 Particle-fluid flow coupling simulation for an erosion for one-directional flow

5.1 Introduction

The previous chapter was considering an erosion mechanism under constant seepage flow in accordance with the previous experiment. Nevertheless, in general condition, the seepage flow is not constant which might be caused by porosity changed or the change in hydraulic gradient. In order to develop the particle-fluid flow simulation, the addition domain should be added for fluid flow calculation. Therefore, half staggered grid has been used to describe the connectivity between these domains.

5.2 The simulation of fluid flow

In this section, the explanation of fluid flow calculation will be described. The calculation of fluid flow is still based on Finite Difference method (FDM) which was used for the particle flow simulation as well. Nevertheless, the partial differential equation which is used to describe the fluid flow is different form particle flow (advection equation). In the fluid flow calculation, the pressure distribution is described by diffusion equation, subsequently, the fluid flow will be produced as follow Darcy's law.

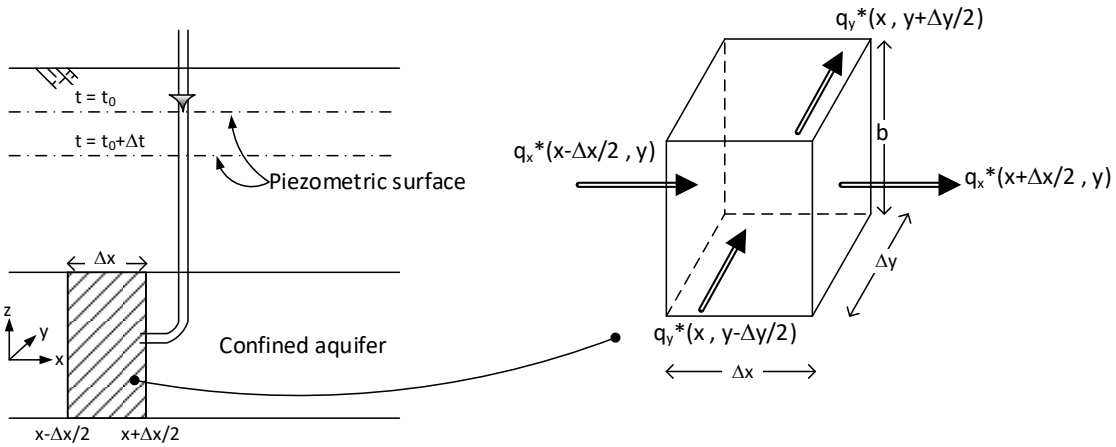

Figure 5.1. Flow in a confined aquifer (Bear J.; 1988)

According to the **Figure 5.1**, the flow in confine aquifer is considered in which the flow in z-direction is ignored. Considering the transmissivity of this aquifer in the horizontal direction, the transmissivity, T, should be in the function of hydraulic conductivity, K, and the thickness of aquifer in the z-direction, b, as shown in the **Equation 5.1**.

$$T = Kb \tag{5.1}$$

In addition, the volume of water, ΔU_w, which is released from the storage of aquifer per unit area, ΔA, and the average difference in piezometric head, φ, is defined as aquifer storativity, S. Therefore, the storativity could expressed as in **Equation 5.2**.

$$S = \frac{\Delta U_w}{\Delta A \Delta \varphi} = S_s b \tag{5.2}$$

Where, φ is the piezometric head in the aquifer which is the summation of pressure head and elevation head as shown in **Equation 5.3**.

$$\varphi = z + \frac{p}{\gamma} \tag{5.3}$$

Where, z is the elevation, p is pressure, and γ is unit weight of fluid.

Furthermore, the consideration of control volume as shown in **Figure 5.1** could mathematically suggest a continuity of fluid flow as shown in **Equation 5.4**.

$$\Delta t\left\{\Delta y\left[q_x^*\left(x-\frac{\Delta x}{2},y\right)-q_x^*\left(x+\frac{\Delta x}{2},y\right)\right]+\Delta x\left[q_y^*\left(x,y-\frac{\Delta y}{2}\right)-q_y^*\left(x,y+\frac{\Delta y}{2}\right)\right]\right\}$$
$$= S\Delta x\Delta y[\varphi(t+\Delta t)-\varphi(t)] \tag{5.4}$$

Where, q^* is the discharge per unit width and could be calculated as $q^* = -Tgrad\varphi$.
By mathematical procedure, the **Equation 5.4** could be reduced the form to be as **Equation 5.5**.

$$-\left(\frac{\partial q_x^*}{\partial x}+\frac{\partial q_y^*}{\partial y}\right) = S\frac{\partial \varphi}{\partial t} \quad \text{or}$$

$$div(Tgrad\varphi) = S\frac{\partial \varphi}{\partial t} \tag{5.5}$$

According to the relationship as following Equation 5.1. and Equation 5.2. with the assumption that transmissivity and hydraulic conductivity are isotropic and independent with location, hence, the continuity of flow in partial differential equation for two-dimensional flow become as in **Equation 5.6**. In addition, the partial differential as in **Equation 5.6** is also well-known as the diffusion equation.

$$\frac{\partial}{\partial x}\left(K\frac{\partial \varphi}{\partial x}\right)+\frac{\partial}{\partial y}\left(K\frac{\partial \varphi}{\partial y}\right) = S_s\frac{\partial \varphi}{\partial t} \quad \text{or}$$

$$\frac{\partial}{\partial x}\left(K\frac{\partial\left(z+\frac{p}{\rho_f g}\right)}{\partial x}\right)+\frac{\partial}{\partial y}\left(K\frac{\partial\left(z+\frac{p}{\rho_f g}\right)}{\partial y}\right)=S_s\frac{\partial\left(z+\frac{p}{\rho_f g}\right)}{\partial t} \tag{5.6}$$

4.3 The staggered grid formation

According to the numerical solution for partial differential equation, the finite difference method generally requires the definition of a grid of nodal points. In erosion simulation, several variables have been utilized, therefore, the variables could be either stored at the same nodal point or difference point depending on their characteristic. The simplest grid is called as non-staggered grid in which all of variables are located at the same nodal point. Conversely, staggered grid takes over the difference location of variables. Furthermore, the example of each two-dimensional grids is compared and shown as in **Figure 5.2**.

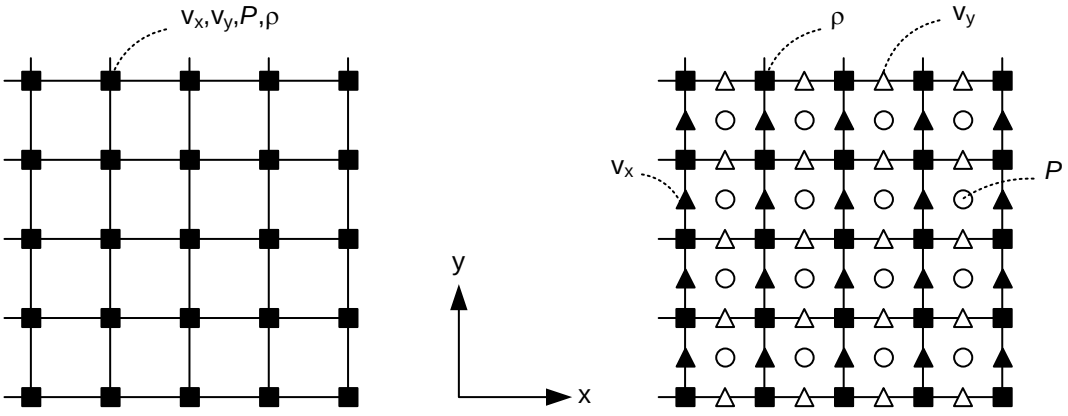

Figure 5.2. The comparison between non-staggered grid and fully staggered grid

In this research, the simplest element which is rectangular element is chosen for the numerical modelling. Nevertheless, considering the erosion calculation the fluid flow velocity is always discretized together with the particle concentration at the nodal node. Therefore, this research considered the grid as half-staggered grid in which the velocity in both x-direction and y-direction are located at the same nodal point as shown in **Figure 5.3**, while pore pressure is located at the center of element in the erosion domain.

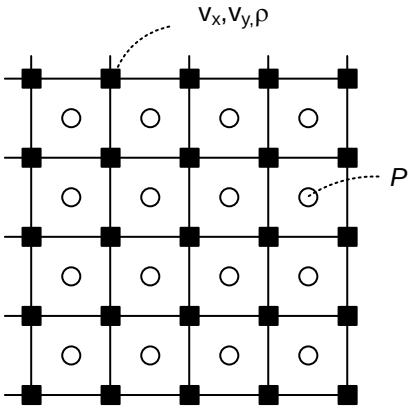

Figure 5.3. Half staggered grid based on erosion domain

5.4 Permeability calculation

In order to conduct the particle-fluid flow coupling simulation, one of the important variables is hydraulic conductivity which is basically a result in erosion calculation and used in the diffusion calculation as following **Equation 5.6**.

According to the erosion calculation, the erosion simulation is mainly resulted in porosity changed. Fortunately, there are many suggestions in the permeability-porosity relation, while the most famous in several major including geomechanics study is known as Kozeny-Carman equation. In addition, the Darcy's shows that the fluid flow in porous media in two-dimensional calculation ($i = 1,2$) is proportional to the hydraulic conductivity and hydraulic gradient as shown in **Equation 5.7**, while the relation between hydraulic conductivity and permeability or intrinsic permeability is shown as **Equation 5.8.**

$$q_i = -K\left(\frac{\partial \varphi}{\partial x_i}\right); \quad i = 1,2 \tag{5.7}$$

$$K = \frac{k\gamma}{\mu} \tag{5.8}$$

Where, q_i is the fluid flow in direction i, k is permeability, K is hydraulic conductivity, and μ is the dynamic viscosity of fluid.

As it mentioned earlier, the permeability could be a function of porosity and most of the function are empirical equation. Kozeny firstly developed the permeability function under the assumption that the porous media is combined with a bundle of capillary tube as shown in **Figure 5.4** with the same length in accordance with Poiseuille's equation as

shown in **Equation 5.9** and suggested the primary equation of permeability as in **Equation 5.11**.

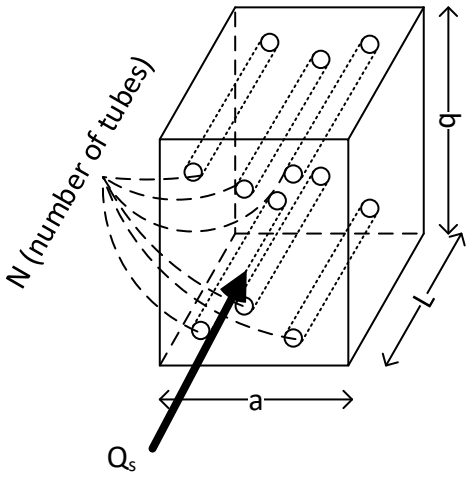

Figure 5.4. The capillary tube models

$$Q_s = -\frac{\pi\delta^4\rho g}{128\mu}\frac{\partial\varphi}{\partial s} \tag{5.9}$$

Where, δ is the capillary tube diameter in direction s, ρ is density of fluid, and μ is dynamic viscosity of fluid.

According to the definition of flow rate, $q_s = \frac{Q_s}{ab}$, and the porosity formation, $n = N\frac{(\pi\delta^4)}{4}$, therefore, the flow rate calculation become **Equation 5.10**.

$$q_s = -\left(\frac{k\rho g}{\mu}\right)\frac{\partial\varphi}{\partial s}; \quad k = \frac{n\delta^2}{32} \tag{5.10}$$

$$k = \frac{c_0 n^3}{M^2} \tag{5.11}$$

Where, c_0 is Kozeny's constant, M is specific surface which is a function of hydraulic radius, R, and porosity, n, $M = \frac{n}{R}$.

In addition, the consideration in the definition of specific surface, $M = (1-n)M_s$, where, M_s is specific area. Henceforth, Carman has used this relation together with the relationship between mean particle size ratio, d_m, and specific area, M_s. Finally, the permeability in a function of porosity become as in **Equation 5.12**, which is well-known as original Kozeny-Carman equation. In addition, the further development of permeability equation from Kozeny-Carman by including the effect of sphericity of

particle, Φ_s, was shown in **Equation 5.13**.

$$k = \frac{{d_m}^2}{180}\frac{n^3}{(1-n)^2} \tag{5.12}$$

$$k = \Phi_S^2\frac{{d_m}^2}{150}\frac{n^3}{(1-n)^2} \tag{5.13}$$

5.5 Calculation scheme

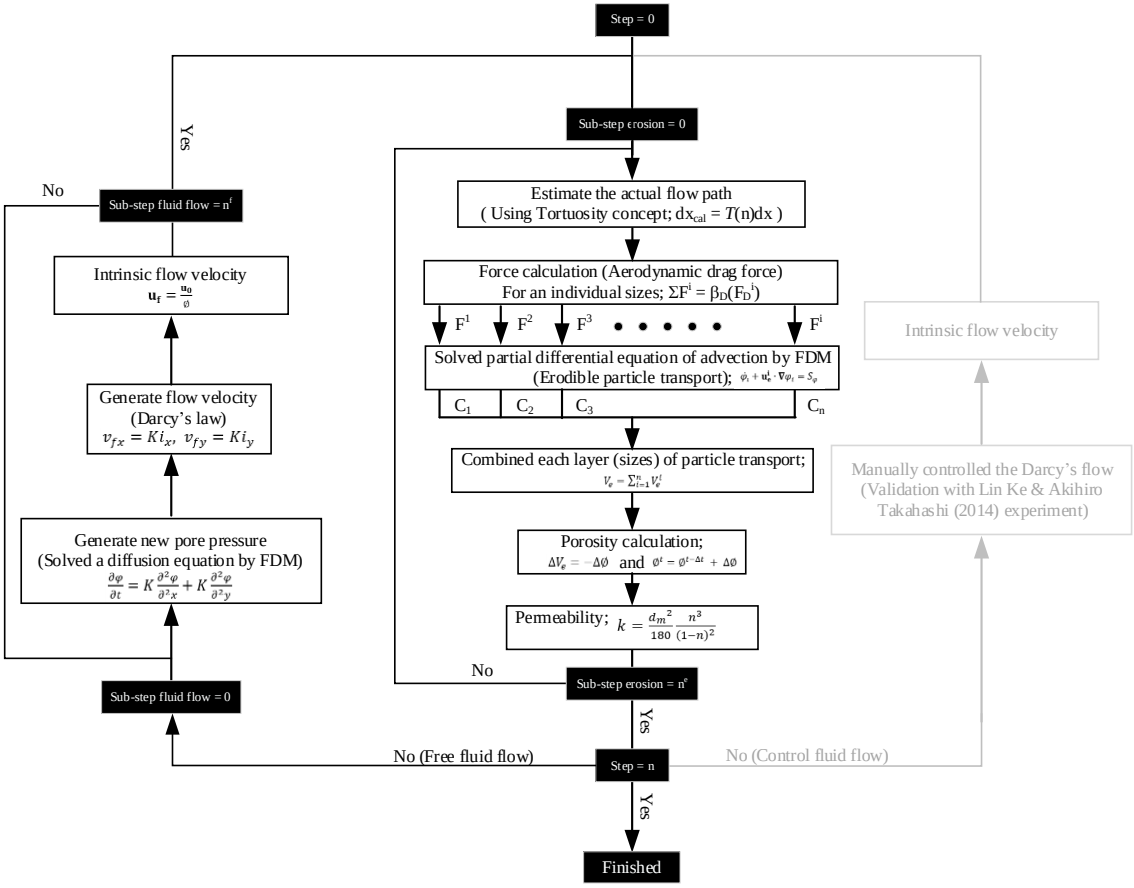

Figure 5.5. The particle-fluid flow coupling analysis

The calculation scheme in this chapter was improved from the previous simulation scheme which was considering the constant flow in corresponding with previous experiment. The extension in the simulation was shown as in **Figure 5.5**, the finite difference method is used to simulate the fluid flow under the utilization of diffusion equation as governing equation.

According to the erosion simulation, the porosity is always regenerated at each

step of calculation in erosion loops, subsequently, the new permeability is calculated as mentioned in previous section which will be used in the fluid flow calculation.

As it mentioned in the previous section, the half-staggered grid is used for the simulation which pressure is located at the centroid of each zone in the erosion domain, while, particle flow velocity is located at the nodal points. Moreover, in the erosion calculation associated by aerodynamic drag force, the fluid flow velocity and particle flow velocity must be located at the same point which is at the nodal point in erosion domain.

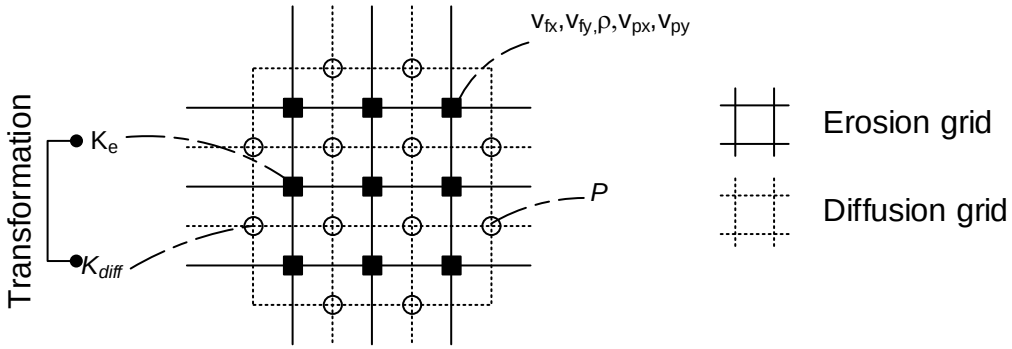

Figure 5.6. Both erosion grid and fluid flow grid

Figure 5.6 shows the erosion grid and diffusion grid together on the same schematic figure. The pore pressure is located at the centroid of erosion domain, conversely, the pressure is located at the nodal point in the diffusion grid which could be discretized by finite difference method. In addition, the permeability which is obtained from the erosion simulation is stored at the nodal points in erosion grid, therefore, it needs to be transformed into the diffusion grid as follow **Figure 5.7**.

According to the size of diffusion domain $(nx + 1, ny + 1)$ is larger than erosion domain (nx, ny), hence, the ghost node has been added surrounding the domain before forming a permeability at the node of diffusion grid as in **Figure 5.7**.

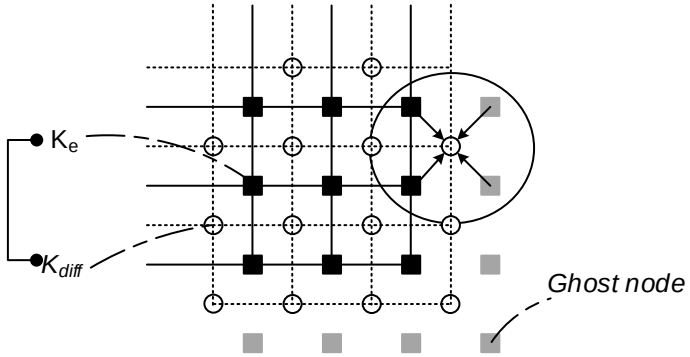

Figure 5.7. The method of permeability transformation

The calculation of fluid flow which should be located at the same point with particle velocity, in addition, the fluid flow velocity is calculated under Darcy's law which requires a hydraulic gradient variable. As shown in **Figure 5.6**, pore pressure is located at the nodal of diffusion domain, therefore, the hydraulic gradient over each nodal point in erosion could be calculated as in **Equation 5.14** and shown in **Figure 5.8**. Subsequently, under the assumption of isotropic of hydraulic conductivity, the fluid flow velocity is computed by using a hydraulic gradient together with hydraulic conductivity as shown in **Equation 5.15**.

$$i^e_{x\,(i,j)} = \frac{1}{\gamma_w}\frac{\partial p}{\partial x} = \frac{1}{\gamma_w}\frac{\frac{1}{2}\left[\left(p^{diff}_{(i,j)}+p^{diff}_{(i,j+1)}\right)-\left(p^{diff}_{(i+1,j)}+p^{diff}_{(i+1,j+1)}\right)\right]}{dx} \quad \text{and}$$

$$i^e_{y\,(i,j)} = \frac{1}{\gamma_w}\frac{\partial p}{\partial y} = \frac{1}{\gamma_w}\frac{\frac{1}{2}\left[\left(p^{diff}_{(i,j)}+p^{diff}_{(i+1,j)}\right)-\left(p^{diff}_{(i,j+1)}+p^{diff}_{(i+1,j+1)}\right)\right]}{dy} \tag{5.14}$$

$$v_{fx} = Ki_x,\ v_{fy} = Ki_y \tag{5.15}$$

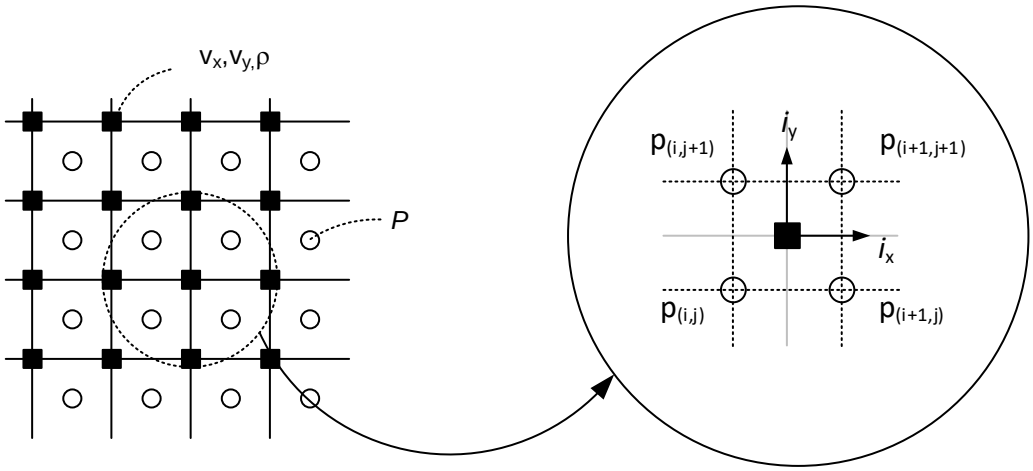

Figure 5.8. The calculation of hydraulic gradient

5.6 Finite Different method for fluid flow

According to the additional scheme for diffusion equation, the simplest scheme is applied which is an explicit calculation. The explicit in time with central in space (FTCS) scheme will be applied on the discretization of diffusion equation. The scheme in two-dimensional calculation is shown as in schematic figure as in **Figure 5.9**.

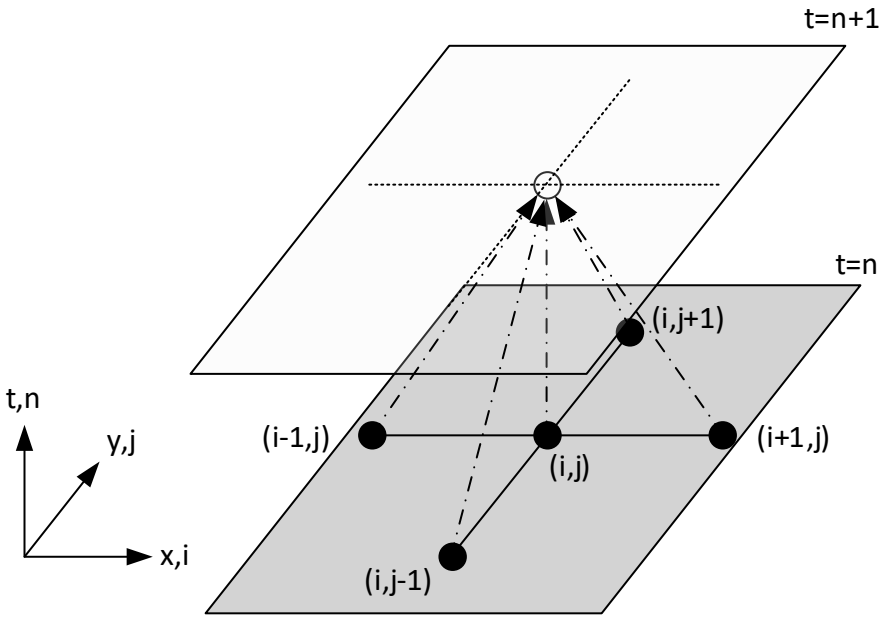

Figure 5.9. The FTCS scheme for discretization of diffusion equation

The diffusion equation as shown in Equation 4.6, when, it was simplified with the normal storativity ($S_s = 1$), the form could be show as in **Equation 5.16**. In corresponding with diffusion equation, the equation is second order partial differential equation, therefore, the discretization of the diffusion become as **Equation 5.17**.

$$\frac{\partial \varphi}{\partial t} = K\frac{\partial^2 \varphi}{\partial^2 x} + K\frac{\partial^2 \varphi}{\partial^2 y} \tag{5.16}$$

$$\frac{\varphi_{i,j}^{n+1} - \varphi_{i,j}^{n}}{\Delta t} = K\frac{\varphi_{i+1,j}^{n} - \varphi_{i,j}^{n} + \varphi_{i-1,j}^{n}}{(\Delta x)^2} + K\frac{\varphi_{i,j+1}^{n} - \varphi_{i,j}^{n} + \varphi_{i,j+1}^{n}}{(\Delta y)^2} \tag{5.17}$$

In this scheme, the stability of scheme with diffusion equation is checked again as well as the scheme for advection equation, Similarly, von Neuman analysis was clearly shown that this scheme is conditionally stable under the criteria as shown in **Equation 5.18**.

$$\Delta t \leq \frac{1}{2K}\frac{(\Delta x \Delta y)^2}{(\Delta x)^2+(\Delta y)^2} \quad \text{or}$$

$$K\Delta t(\Delta x)^2 + K\Delta t(\Delta y)^2 \leq \frac{1}{2} \quad (5.18)$$

5.7 Numerical simulation

In this chapter, the numerical simulation of coupling analysis is conducted to show an erosion undergoing the permeability change as well as pore pressure. The soil which was used in the previous chapter is taken to use in this chapter again.

5.7.1 The coupling simulation of particle-fluid flow with difference pressure head

5.7.1.1 Analysis background

In this simulation firstly, the various pressure at the upstream would be applied as follow **Figure 5.11**. Nevertheless, this simulation keeps using the same size of soil model. The different pressure head at the upstream would generate different seepage force in accordance with the Darcy's law, the seepage velocity is a function of hydraulic gradient. In addition, in this section of simulation will not show only erosion mechanism but permeability change and pore pressure distribution as well. In addition, the pressure head, Δh, at the upstream was initially assigned about 0.6 m which will generate a similar seepage flow to the previous study. However, the particle-fluid flow coupling simulation would not be showing a behavior in the experiment from Ke and Takahashi (2014), since, their experiment had controlled the seepage velocity.

Furthermore, in this simulation would show two different conditions in the fluid flow calculation. The first simulation would be calculated the erosion and fluid flow simultaneously since the beginning of simulation, while the second simulation would be the decoupling analysis at the beginning until hydraulic gradient become uniform or steady flow condition as shown in **Figure 5.10**.

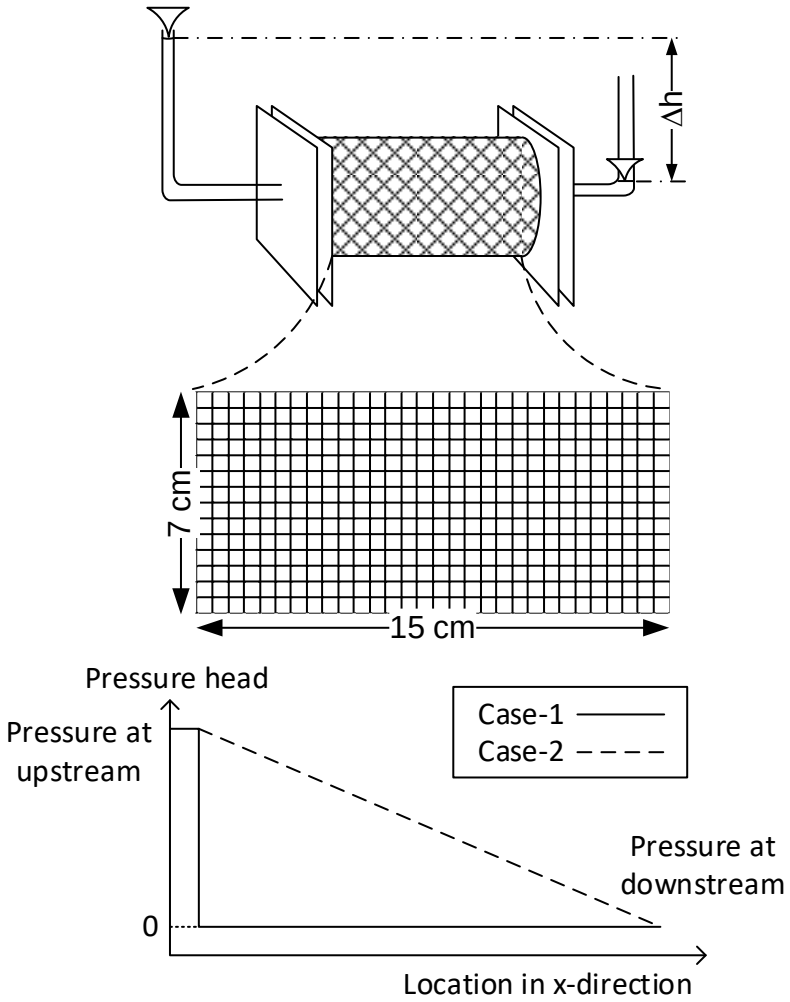

Figure 5.10. The schematic figure of simulation with various pressure head

5.7.1.2 Result and discussion (Case-1)

In this simulation, the pressure head is applied at the upstream only which will begin to flow at the same time with particle flow as mentioned in **Figure 5.10**. In addition, the example of pressure head distribution over the domain is shown in **Figure 5.11**, the pressure is being close to constant gradient when the calculation time is about 2000 sec. Therefore, fine particle will be gradually eroded in accordance with slow seepage flow at the beginning as shown in **Figure 5.12**. In addition, this section of simulation also tried to vary a pressure head at the upstream, when the hydraulic head is about 0.6, the erosion takes more longer time for being eroded.

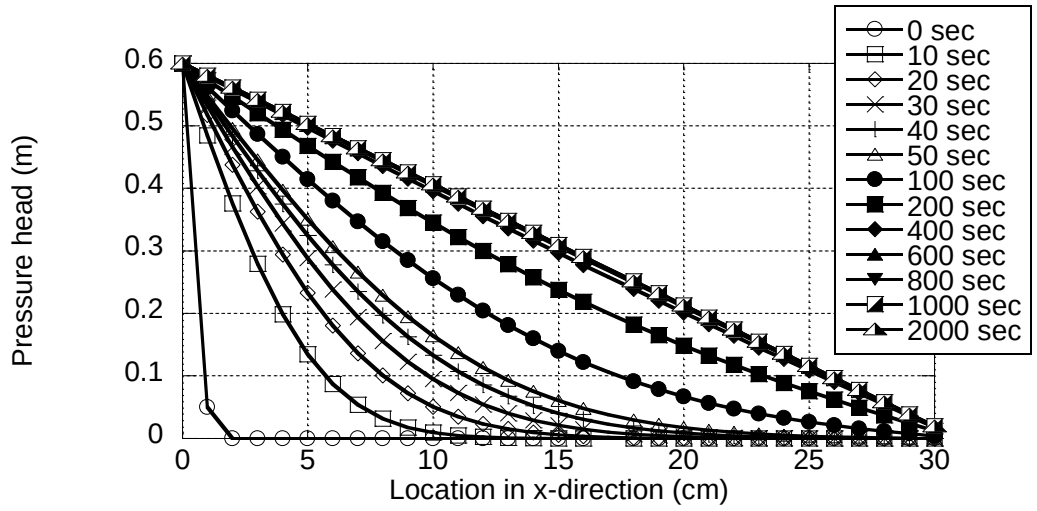

Figure 5.11. The pore pressure distribution over the domain

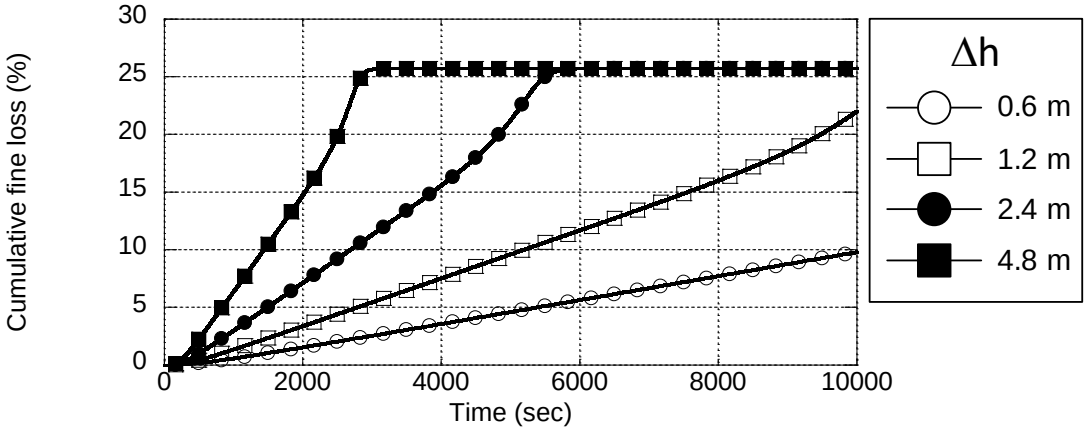

Figure 5.12. The cumulative fine loss in particle-fluid coupling simulation case-1

5.7.1.3 Result and discussion (Case-2)

Similarly, the coupling simulation in particle-fluid flow has done with the same condition, but there is a difference in the fluid flow condition. In this test, the fluid flow would be simulated first until the hydraulic gradient become uniform or fluid flow become steady temporary before conducting coupling analysis. According to the **Figure 5.13**, the erosion rate seems to be higher than erosion in case-1. In addition, the erosion rate might be constant as well in corresponding with liner propagation of cumulative fine loss.

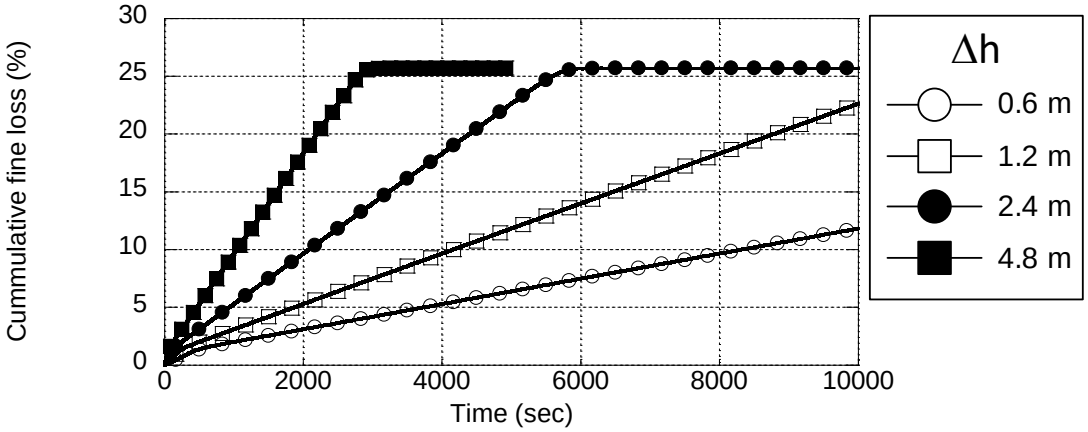

Figure 5.13. The cumulative fine loss in particle-fluid coupling simulation case-2

5.8 Conclusion

In this chapter, the simulation of particle-fluid flow coupling calculation including one-directional flow and two-directional flow was shown and discussed. The first simulation which was about the one-directional flow show the difference between simulation procedure, where the period of fluid flow calculation was considered. The difference calculation method is standing for the difference of the model or geological condition. In the long-term behavior, where the permeability of material is relatively low in accordance with the size of domain, the uncoupling simulation for generate fluid flow might be necessary to save computational cost and continuing with conducting couple simulation.

However, the difference initiation of pore pressure or fluid flow calculation could be done, but the consideration in state of flow is also important. According to the one-directional flow simulation, the different initiation of pore pressure is much influence on the erosion behavior. Therefore, the subsequence simulation which will be conducted, the consideration of initiation of pore pressure is should be considered as following either vertical shaft construction condition or experimental condition.

Chapter 6 Particle-fluid flow coupling simulation for an erosion for two-dimensional flow in gravitational field

6.1 Introduction

In this chapter, the it is a subsequence simulation from simulation in previous chapter. The particle-fluid flow simulation was conducted previously to examine the erosion rate under difference flow condition as shown in chapter 5. Therefore, the investigation will move to the simulation of two-directional flow which is related with either real construction or previous experiment. The background of simulation in this chapter came from the dewatering in vertical shaft during excavation process might be inducing an internal erosion. However, the limitation of computational performance, only the soil behind vertical shaft structure would be conducted here. Furthermore, the small scale of experiment which was done for air bubble experiment has been taken to apply for internal erosion simulation as well.

6.2 The simulation procedure

Basically, the simulation scheme and concept were obtained from the previous section of simulation as well as the staggered grid formation which was done by Finite Difference method (FDM). However, the simulation of in this chapter is related with gravitational field and two-directional flow. Therefore, the scheme for advection discretization could no longer valid in accordance with the unpredictable direction of flow. In addition, the gravitational field is normally associating in the flow in gravitational direction.

6.2.1 The modification of simulation scheme for two-directional flow in gravitational field

6.2.1 The fluid flow in gravitational field

In this chapter, the simulation will continue in the two-directional flow in gravitational

field as well. The difference between fluid flow as following Darcy's law in gravitational direction and non-gravitational direction is the consideration of gravity effect. Therefore, the fluid flow calculation which was used in the **Equation 5.14** will become **Equation 6.1**. According to this equation, it is clearly shown that the fluid flow is occurring, when the pressure gradient is difference from gravity.

$$v_{fx} = K_x \frac{1}{\gamma_w} \frac{\partial}{\partial x}(p - \rho_w g_i x) \text{ and } v_{fy} = K_y \frac{1}{\gamma_w} \frac{\partial}{\partial y}\left(p - \rho_w g_y y\right) \quad (6.1)$$

6.2.2 The erosion scheme for two-directional flow

In addition, the upwind discretization for advection in erodible particle basically stands for one-directional flow as mentioned in chapter 4. In general, the simulation apart from soil sample test, both fluid flow and particle flow could be forward and reveres in any direction due to the uncertain pressure distribution. Therefore, the unstable calculation of simulation in this chapter, especially in the case of sheet pile simulation, might occur due to the upwind scheme.

According to the characteristic of advection equation, the explicit in time and central in space scheme (FTCS) could not be used due to the unconditionally stable. Fortunately, the modified FTCS scheme by Lax-Friedrichs method could become a conditionally stable scheme as shown in **Equation 6.2**. Lax-Friedrichs method has stabilized the central node by averaging surrounding node value and replace with central node at current time step as shown in **Figure 6.1**.

$$\varphi_{i,j}^{n+1} = \frac{1}{4}\left(\varphi_{i+1,j}^{n} + \varphi_{i,j+1}^{n} + \varphi_{i-1,j}^{n} + \varphi_{i,j-1}^{n}\right) - \frac{\Delta t}{2\Delta x} u_x \left(\varphi_{i+1,j}^{n} - \varphi_{i-1,j}^{n}\right) - \frac{\Delta t}{2\Delta y} u_y \left(\varphi_{i,j+1}^{n} - \varphi_{i,j-1}^{n}\right) \quad (6.2)$$

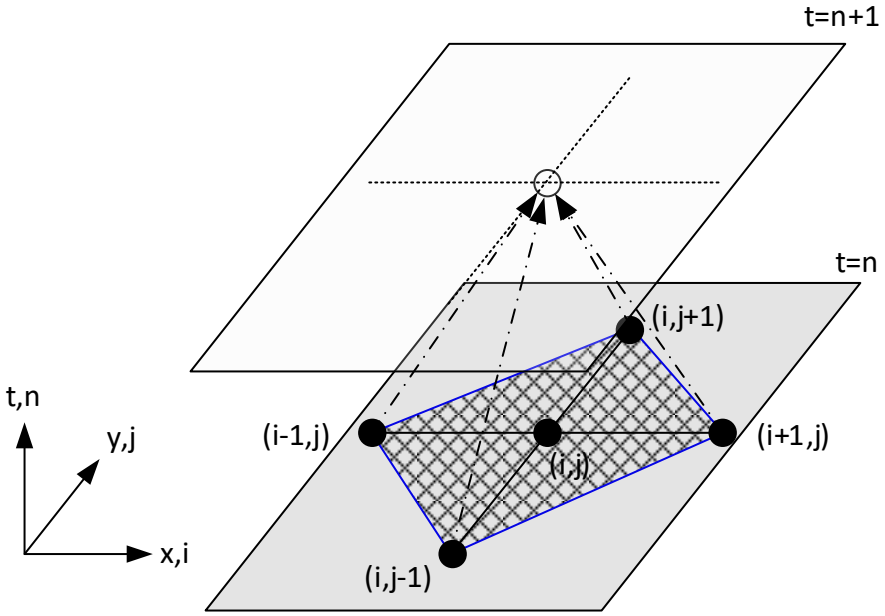

Figure 6.1. The Lax-Friedrichs scheme for advection equation discretization

According to the simulation model, the uniform grid is always utilized, hence, the Lax-Friedrichs is also conditionally stable scheme which will be stable under the condition as following **Equation 6.3**.

$$\Delta t \leq \frac{\Delta x}{\sqrt{2\left(u_x^2+u_y^2\right)}};\ \Delta x = \Delta y \tag{6.3}$$

6.3 Numerical simulation

In this chapter, the numerical simulation of coupling analysis is conducted to show an erosion undergoing the permeability change as well as pore pressure. According to the numerical simulation in gravitational field, not only advection discretization for particle flow is changed but the Darcy's flow calculation is changed as it was mentioned earlier and in **Figure 6.2**. The soil which was adopt from the previous chapter is taken to use in this chapter again as showing with the gradation of soil as shown in **Figure 6.3.**

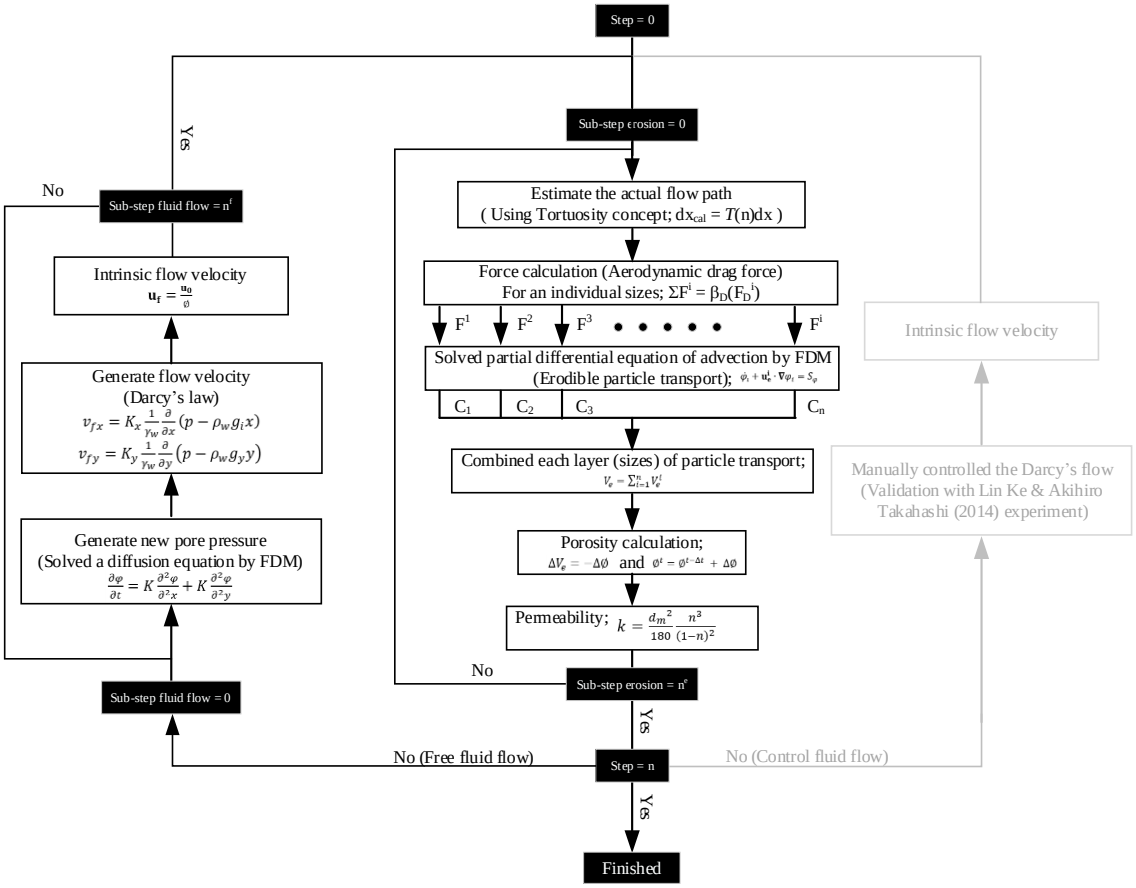

Figure 6.2. The calculation scheme for numerical simulation in gravitational field

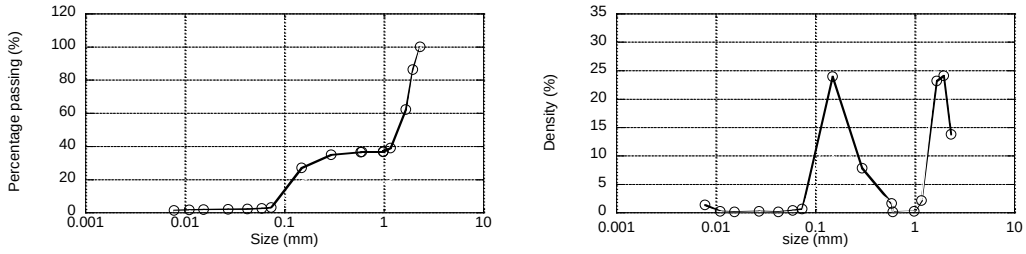

Figure 6.3. The grain size distribution of soil

6.3.1 The simulation of erosion in two-dimensional analysis

6.3.1.1 Analysis background

According to the shaft structure, the construction process is always required a dewatering system to reduce the water level inside vertical shaft. According to the dewatering method,

the difference of waterhead inside and surrounding shaft is basically inducing a seepage flow beneath cylindrical shaft. Furthermore, the pore pressure distribution from the simulation of soil-water coupling analysis chapter shows that the pore pressure distribution along the shaft wall as shown in **Figure 6.4**. The pore pressure at the bottom of shaft is slightly different between inner shaft and outer shaft.

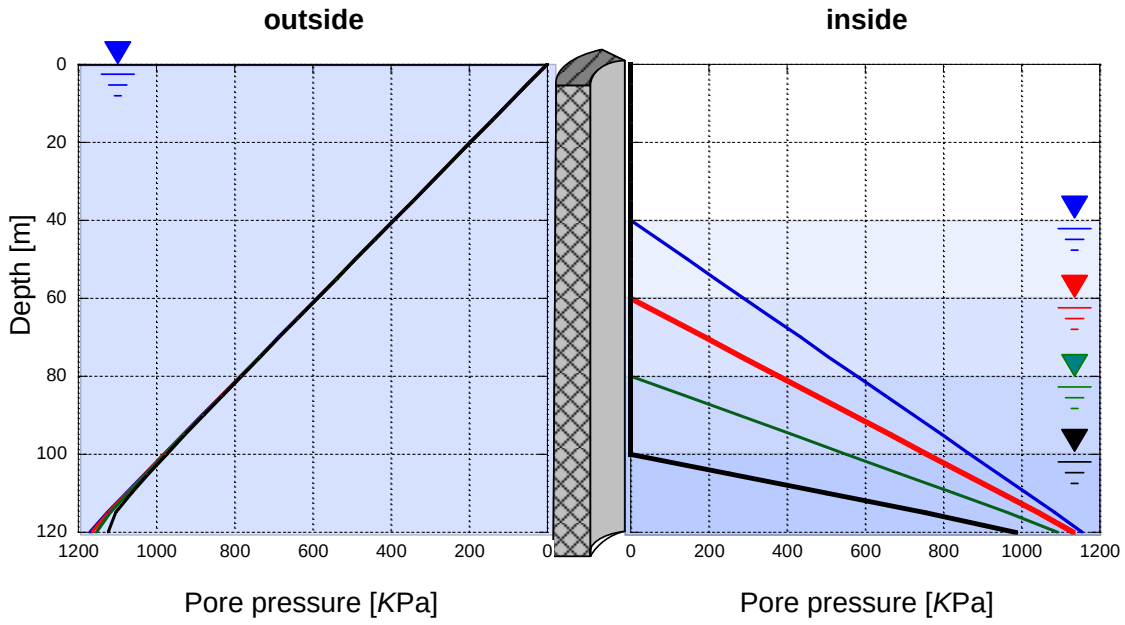

Figure 6.4. The pore pressure distribution along vertical shaft wall

According to the limitation of simulation code which still could not describe all over the domain, hence, the soil behind the shaft wall would be focused as shown in **Figure 6.5**. The erosion is likely to occur at the bottom layer nearby the shaft tip in which the high fluid flow located. The simulation is conducted in two-dimensional domain.

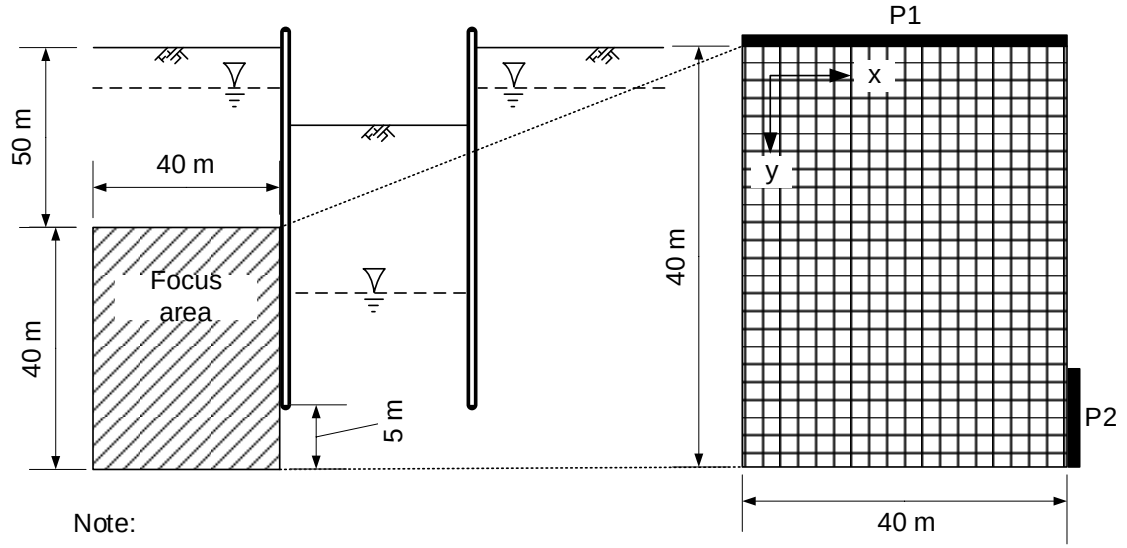

Figure 6.5. The focus area for two-dimensional flow simulation

6.3.1.2 Result and discussion

In this simulation, the area of interest is the surrounding soil, therefore, the conditions of analysis model would be applied as following to the area as shown in **Figure 6.5**. In this simulation, the pore pressure at the bottom of shaft is basically influenced by the dewatering process as shown in **Figure 6.4**. The simulation also shows that the soil domain is located at 50 m beneath ground surface. According to the dewatering induce the pore pressure changes, hence, at the bottom of shaft wall the pore pressure would be controlled with the lower pressure than hydrostatic pressure.

The first case of simulation, the pressure head at the downstream was controlled at 70 m which is representing for shallow dewatering. Conversely, the 30 m of pressure head at downstream would be the deeper dewatering. According to **Figure 6.6** and **Figure 6.10**, the progression of porosity could also express the erosion zone, the result shows that the erosion basically starts to occur from the bottom of shaft and then laterally and vertically expanded. In addition, the changes in porosity results in the permeability and hydraulic conductivity change as shown in **Figure 6.8** and **Figure 6.12**. However, the mechanism of this simulation might be defined as long term behavior in accordance with the low permeability in comparison with the domain size, therefore, the seepage flow is

relative slow. In addition, the pore pressure distribution is also confirmed that the pore pressure development is gradually change as shown in **Figure 6.7** and **Figure 6.11**. Similarly, the high seepage velocity is mostly located at the bottom of shaft in corresponding with the high hydraulic conductivity and high hydraulic gradient as in **Figure 6.9** and **Figure 6.13**. Moreover, the deeper dewatering depth triggers the faster erosion as following comparison of porosity between two difference pressure controlled.

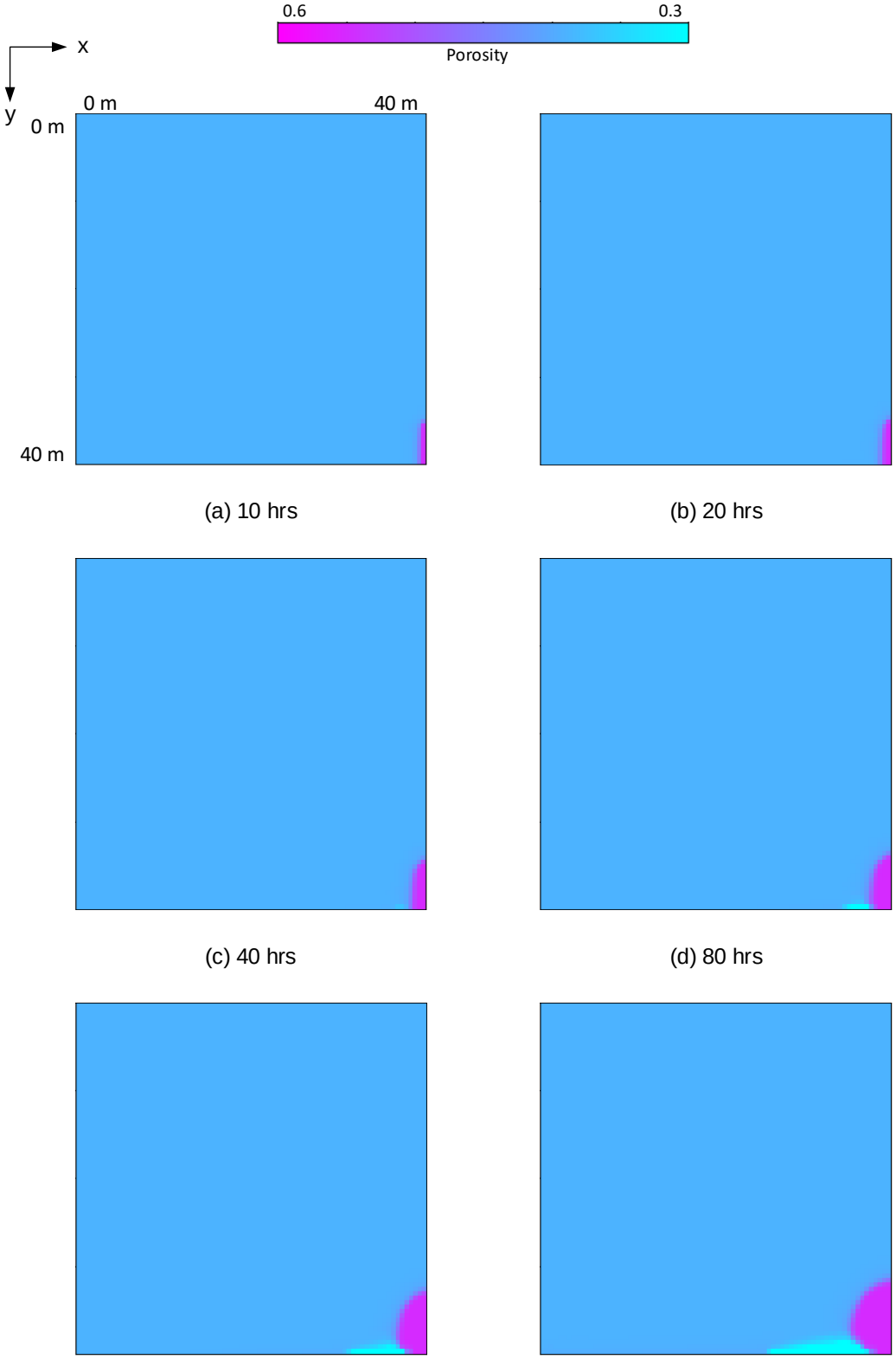

Figure 6.6. Porosity contour (P2 = 70 m)

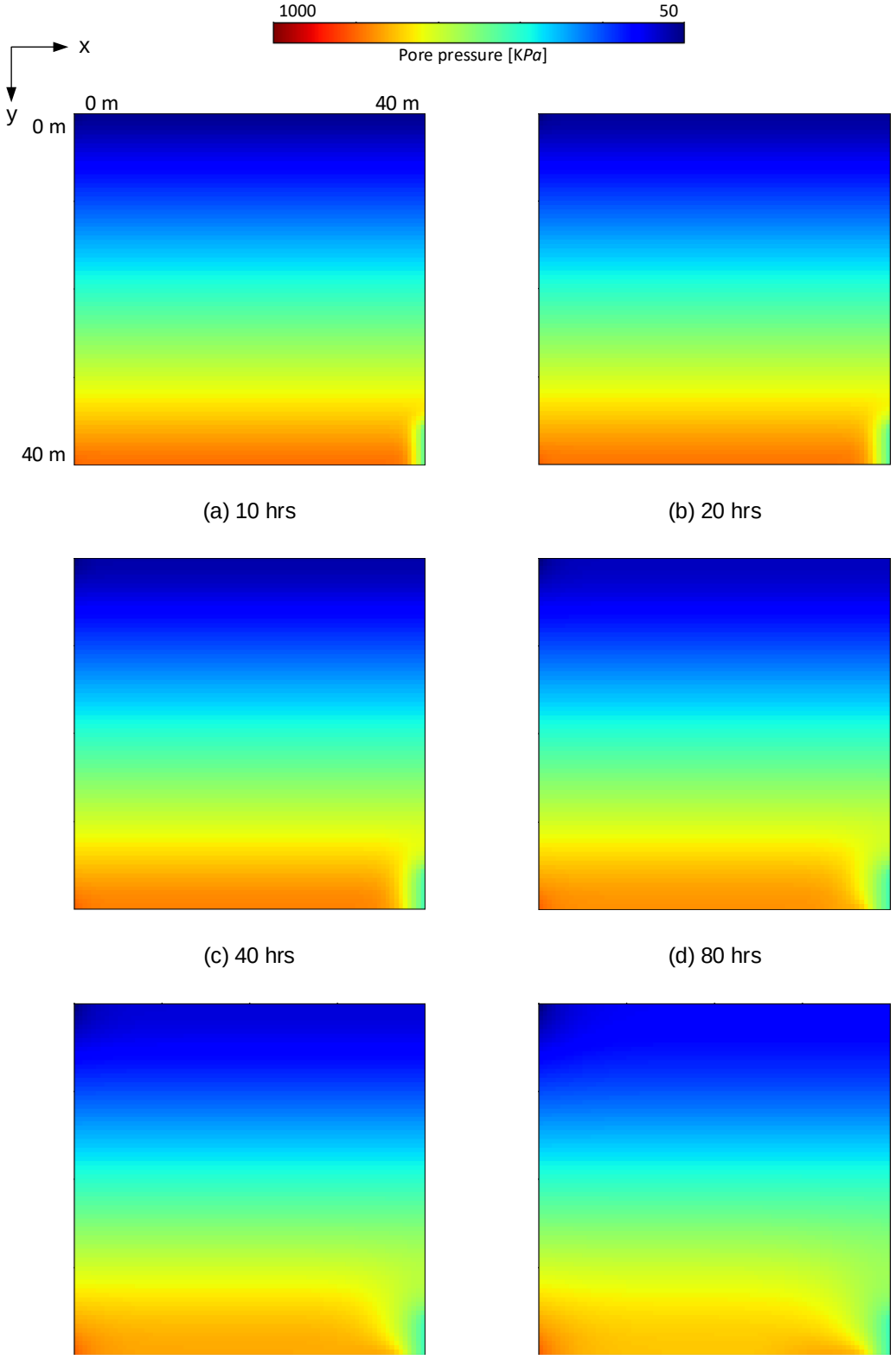

Figure 6.7. Pore pressure contour (P2 = 70 m)

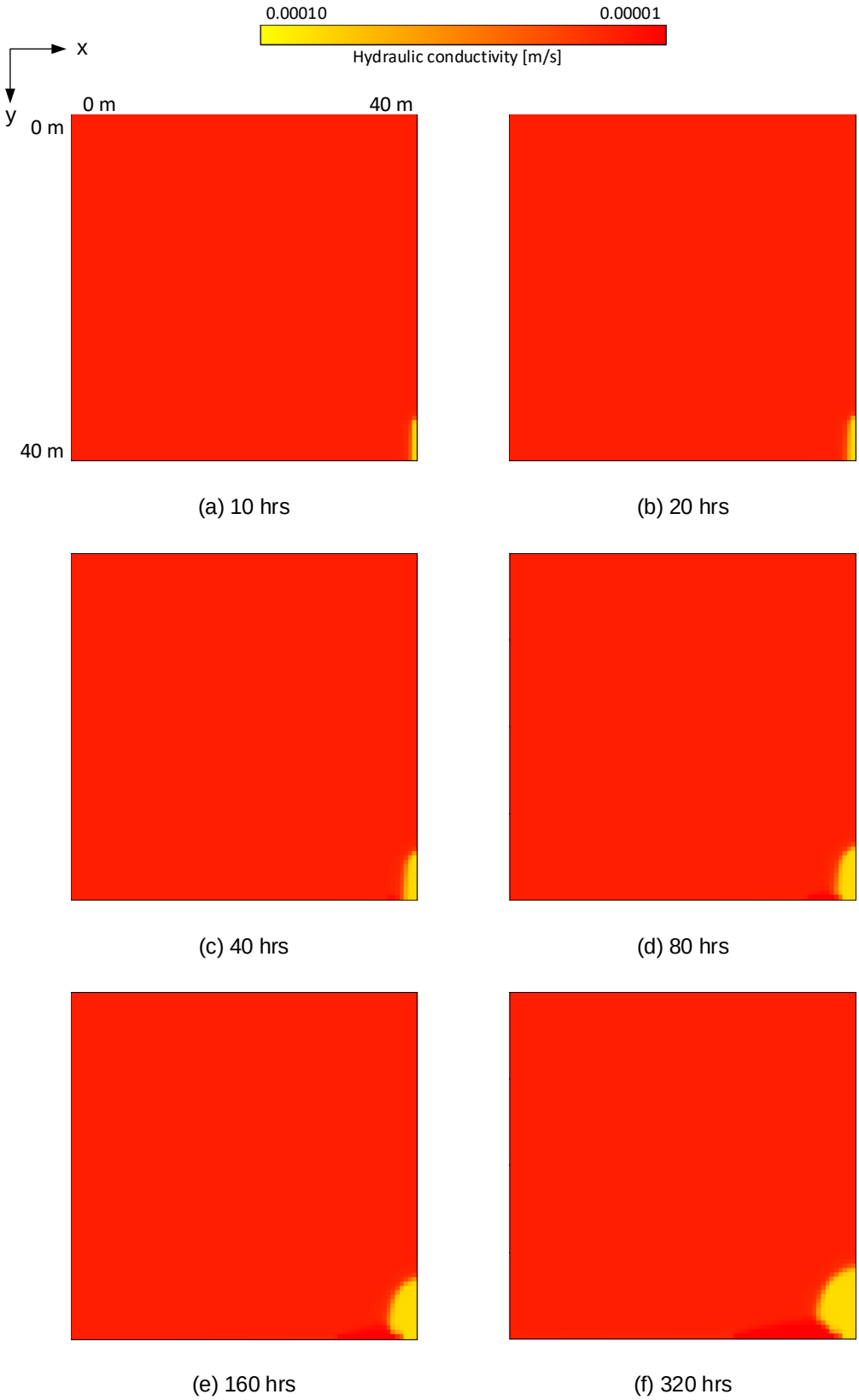

Figure 6.8. Hydraulic conductivity contour (P2 = 70 m)

(a) 10 hrs

(b) 20 hrs

(c) 40 hrs

(d) 80 hrs

(e) 160 hrs

(f) 320 hrs

Figure 6.9. Flow vector field (P2 = 70 m)

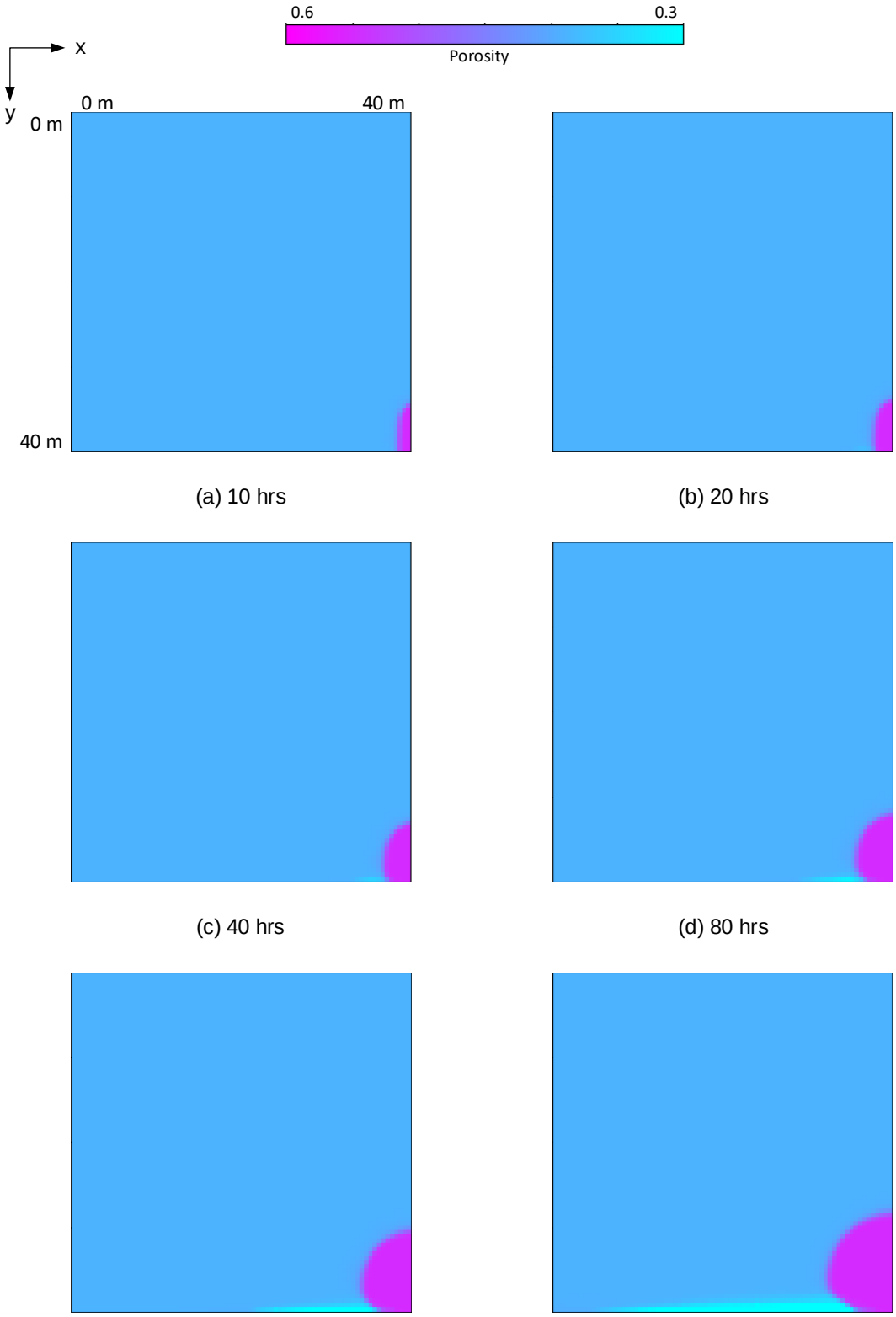

Figure 6.10. Porosity contour (P2 = 30 m)

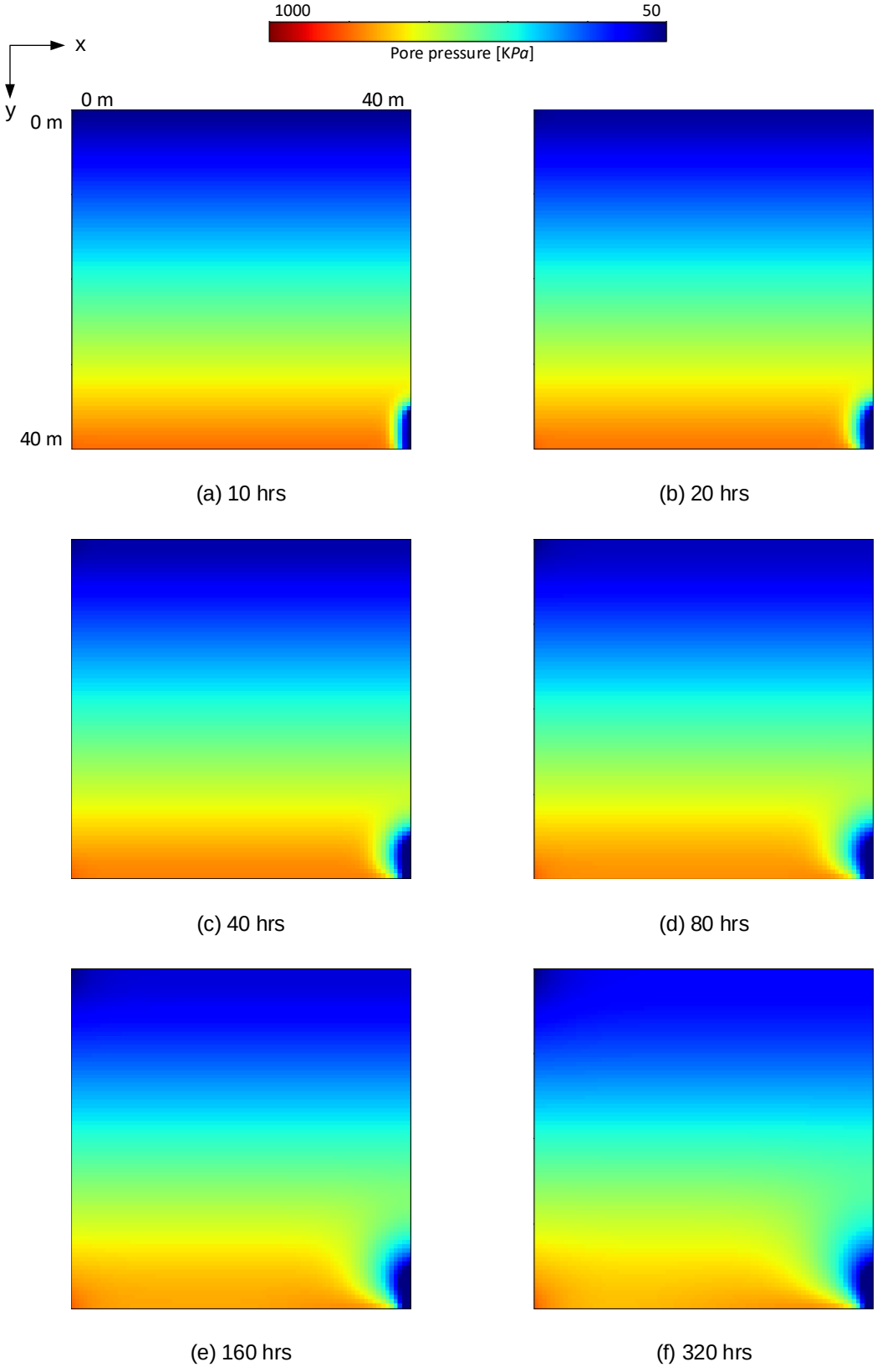

Figure 6.11. Pore pressure contour (P2 = 30 m)

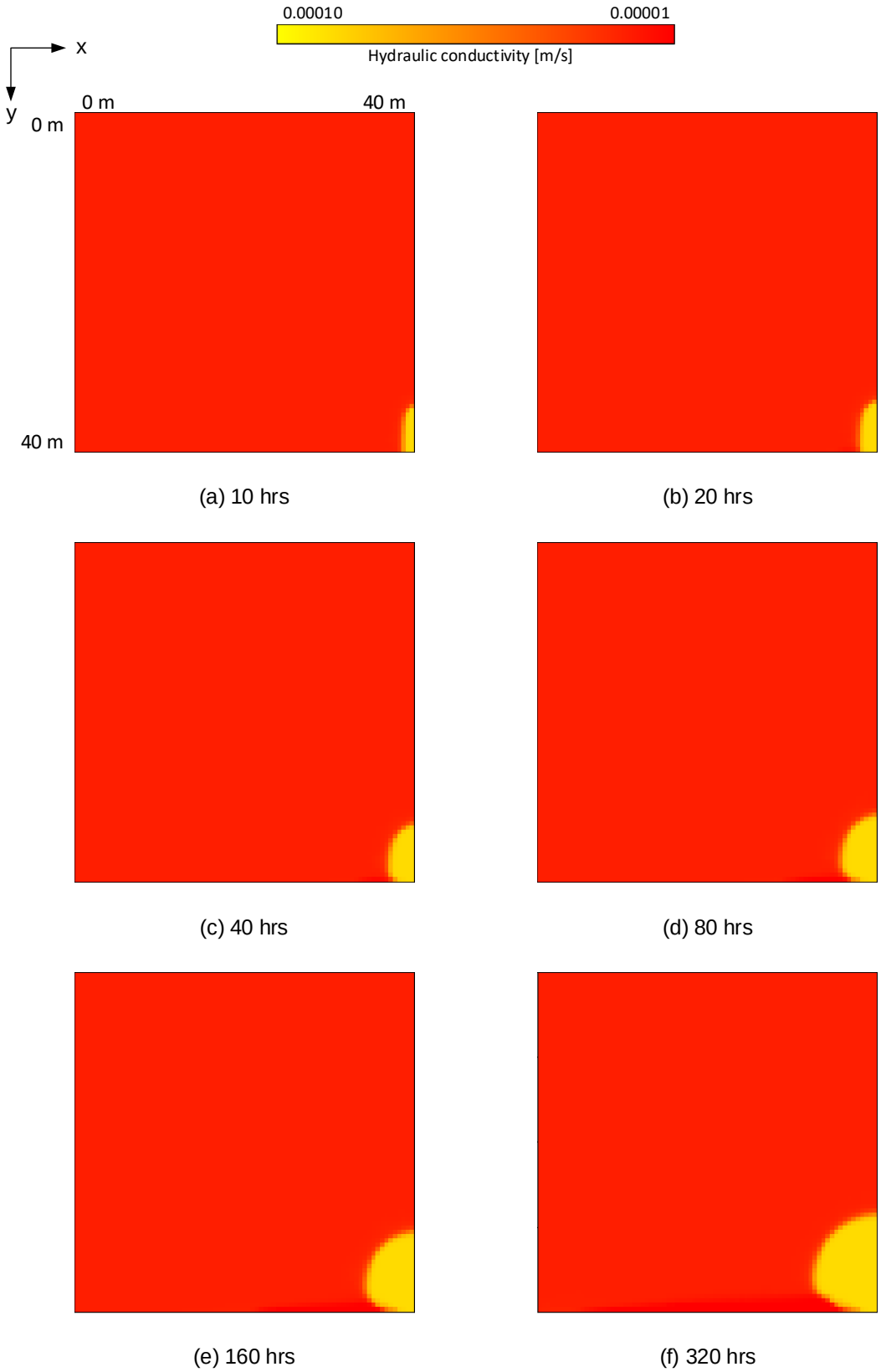

Figure 6.12. Hydraulic conductivity contour (P2 = 30 m)

Figure 6.13. Flow vector field (P2 = 30 m)

6.3.2 The simulation of experimental model

6.3.2.1 Analysis background

In this section, the simulation of experiment model of fluid flow over sheet pile wall will be conducted. Accordingly, the experiment on suffusion in vertical shaft structure even along sheet pile structure is rarely studies, however, there are some examples experimental set-up which was done for air bubble along sheet pile wall investigation. As it mentioned earlier, the seepage flow through sheet pile wall with two difference hydraulic head is similar with shaft construction associated with dewatering process. Therefore, in this section of simulation, the simple simulation of internal erosion or suffusion in sheet pile structure will be conducted and referring to the experiment condition from Kodaka & Asaoka (1994) as shown in **Figure 6.13**.

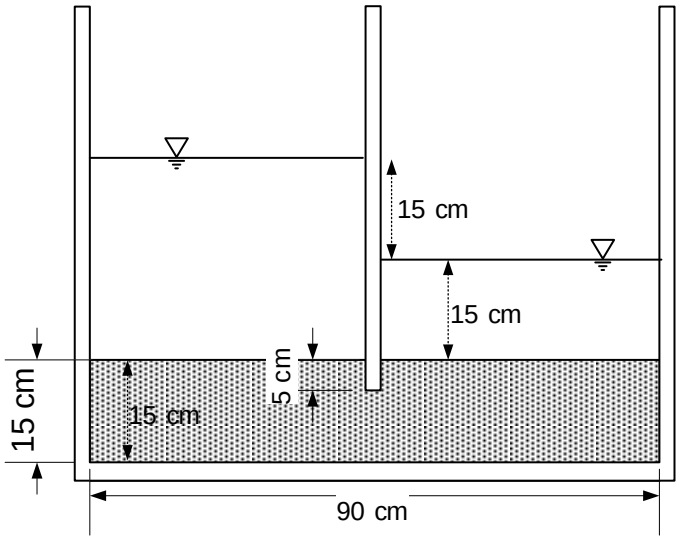

Figure 6.14. The schematic section of internal erosion simulation around sheet pile wall

6.3.2.2 Result and discussion

According to the simulation of seepage through sheet pile wall, the contour of each parameter was shown at 100 secs and 200 secs as shown in **Figure 6.15** and **Figure 6.16**. According to the result, the difference pressure heads which was initially set is resulting in the erosion at the bottom of sheet pile. However, the erosion is not only occurring at the bottom of sheet pile but also at the top downstream area. Moreover, the seepage flow

vector as in the **Figure 6.15** and **Figure 6.16** has confirm that the high seepage flow velocity is concentrated at the bottom of sheet pile or shaft wall. According to this behavior, the downstream side which could be implied as an inner shaft zone is also encountering with erosion.

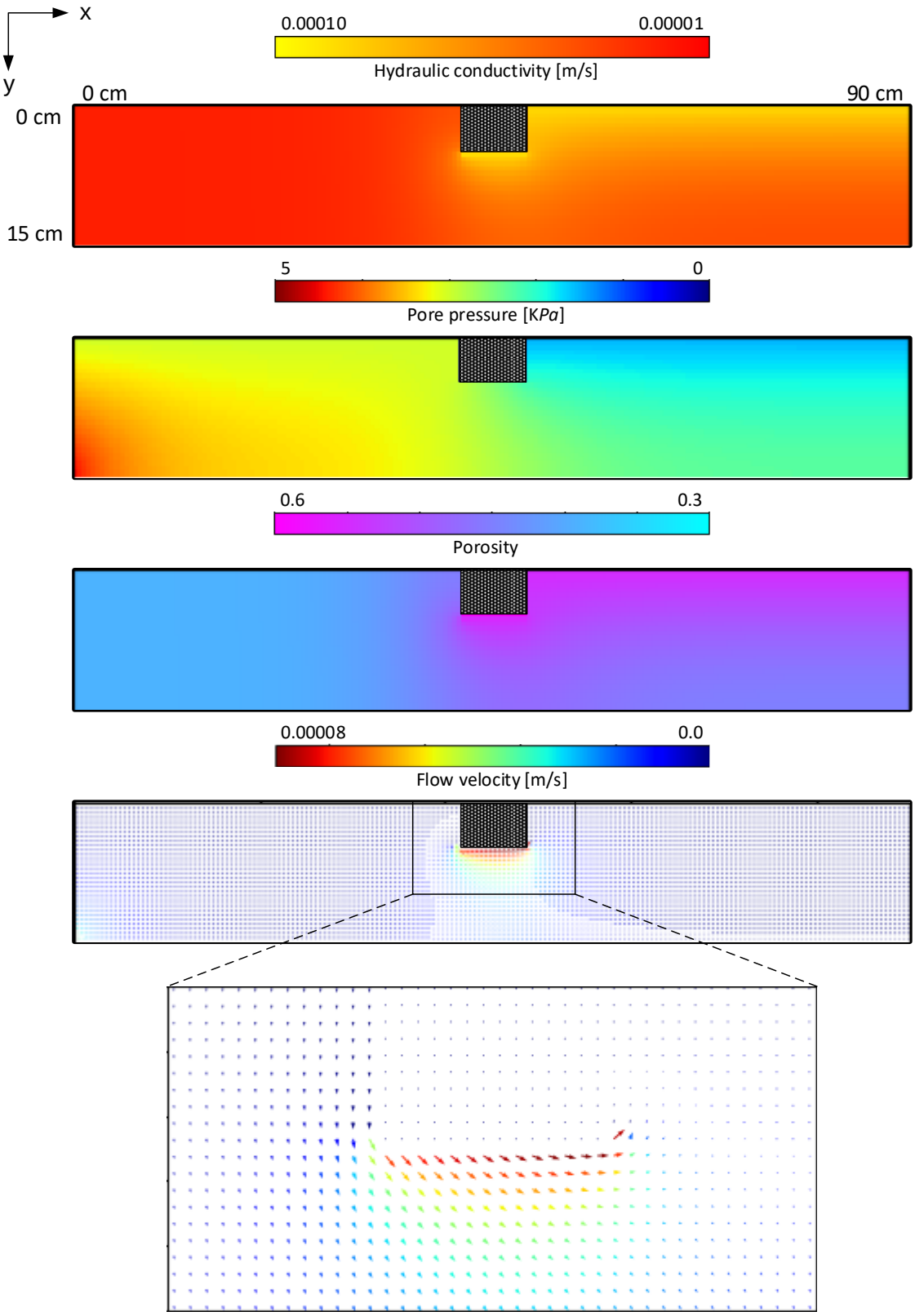

Figure 6.15. The result at 100 secs

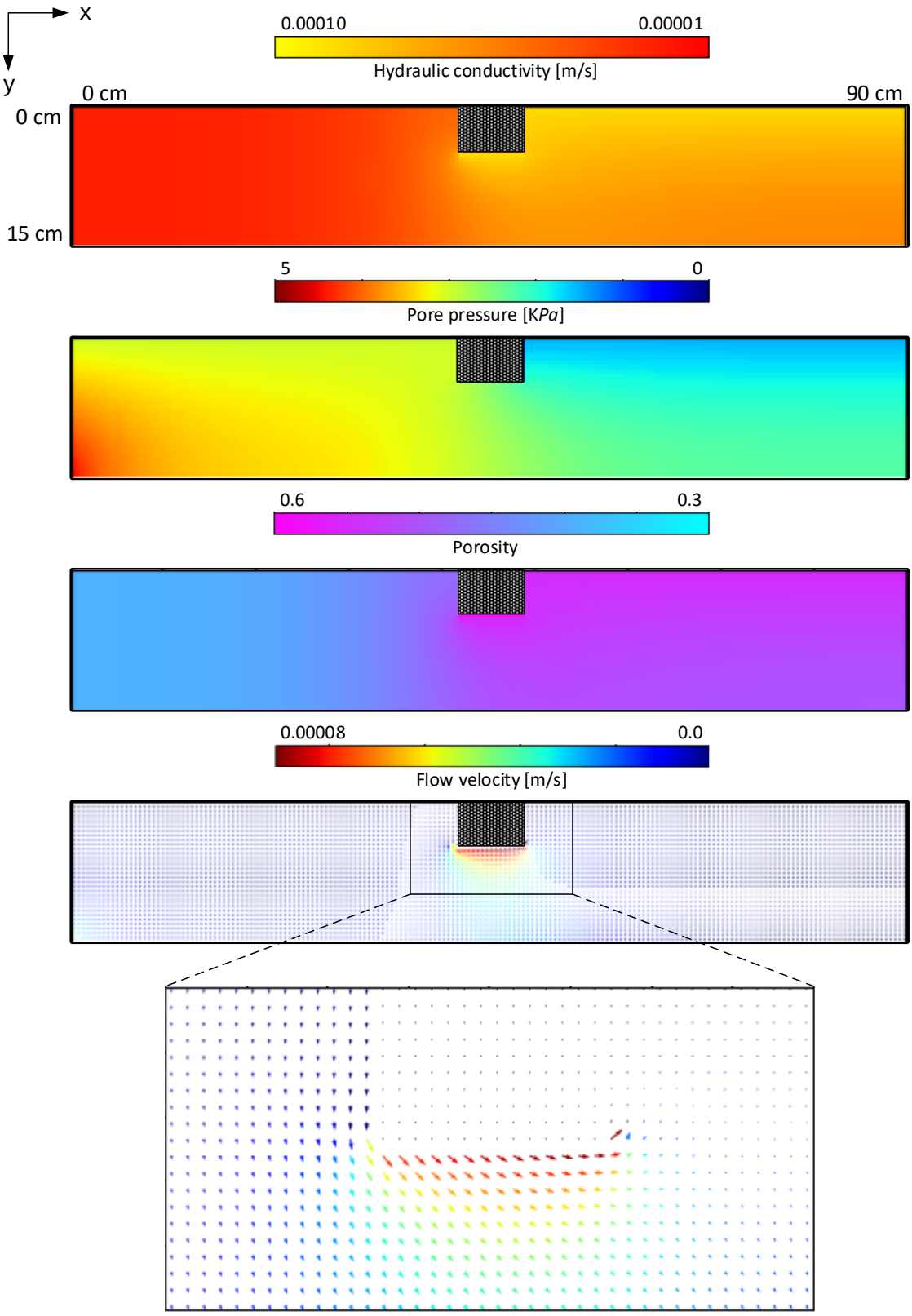

Figure 6.16. The result at 200 secs

6.3.3 The simulation of experimental model considering the dewatering characteristic

6.3.3.1 Analysis background

Considering the real construction of either sheet pile wall or vertical shaft structure in high groundwater area. The water level at excavation side must be reduced by dewatering method Hence, in this section, the simulation is improved from previous condition to consider the dewatering process. According to the dewatering process is always associated with the shaft construction, therefore, the dewatering location has been located at the downstream side. In addition, the size of dewatering point is differently defined as two different cases as shown in **Figure 6.17** in which the dewatering point is located the same level of the tip of sheet pile.

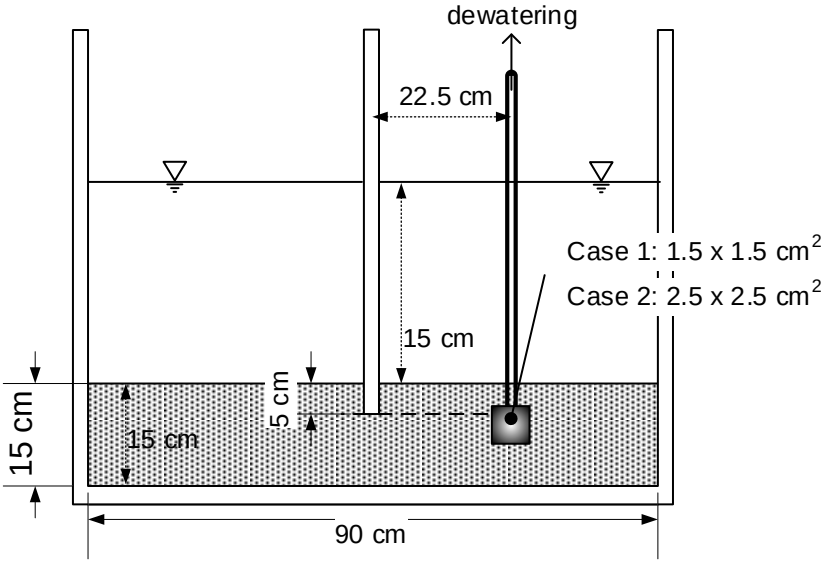

Figure 6.17. The schematic figure of small-scale simulation with dewatering process

6.3.3.1 Result and discussion

According to the simulation model, the dewatering size which is located at the downstream side has been defined as two different sizes. The simulation result which is firstly shown here is the simulation with 1.5x1.5 cm^2 in dewatering location. Subsequently, the dewatering size is expanded to 2.5x2.5 cm^2 to show the influence of different dewatering size which might be related with the size of the dewatering pipe. In addition,

the simulation results have been shown as at three different time which are 50, 100, and 200 seconds, to show the erosion development. Similarly, the hydraulic conductivity is basically changed due to the erosion process in correspondence with the Kozeny-Carman relation as shown in **Figure 6.18** and **Figure 6.22**. According to the simulation results, the hydraulic conductivity has been increasing due to the erosion at the dewatering area which can be obviously found in porosity contour as well as shown in **Figure 6.20** and **Figure 6.24**. The results from both hydraulic conductivity and porosity obviously confirm that the erosion is start at the dewatering point, in addition, the erosion at the pile tip is still found due to the concentration of quick flow beneath the sheet pile wall. Pore pressure contour is one of the results showing here in this section, the dewatering causes a rapid change of pore pressure at the area of dewatering pipe placed on as shown in **Figure 6.19** and **Figure 6.23**.

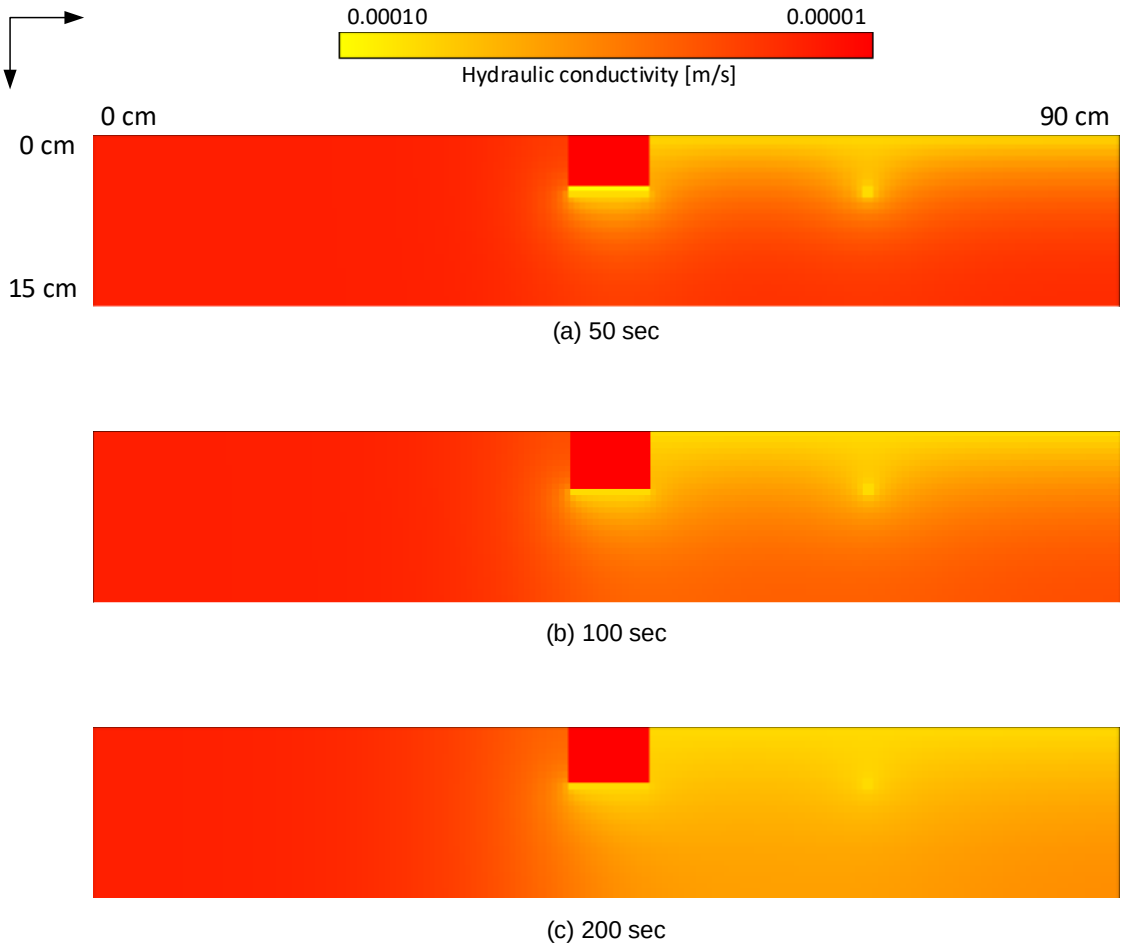

Figure 6.18. Hydraulic conductivity contour (case-1)

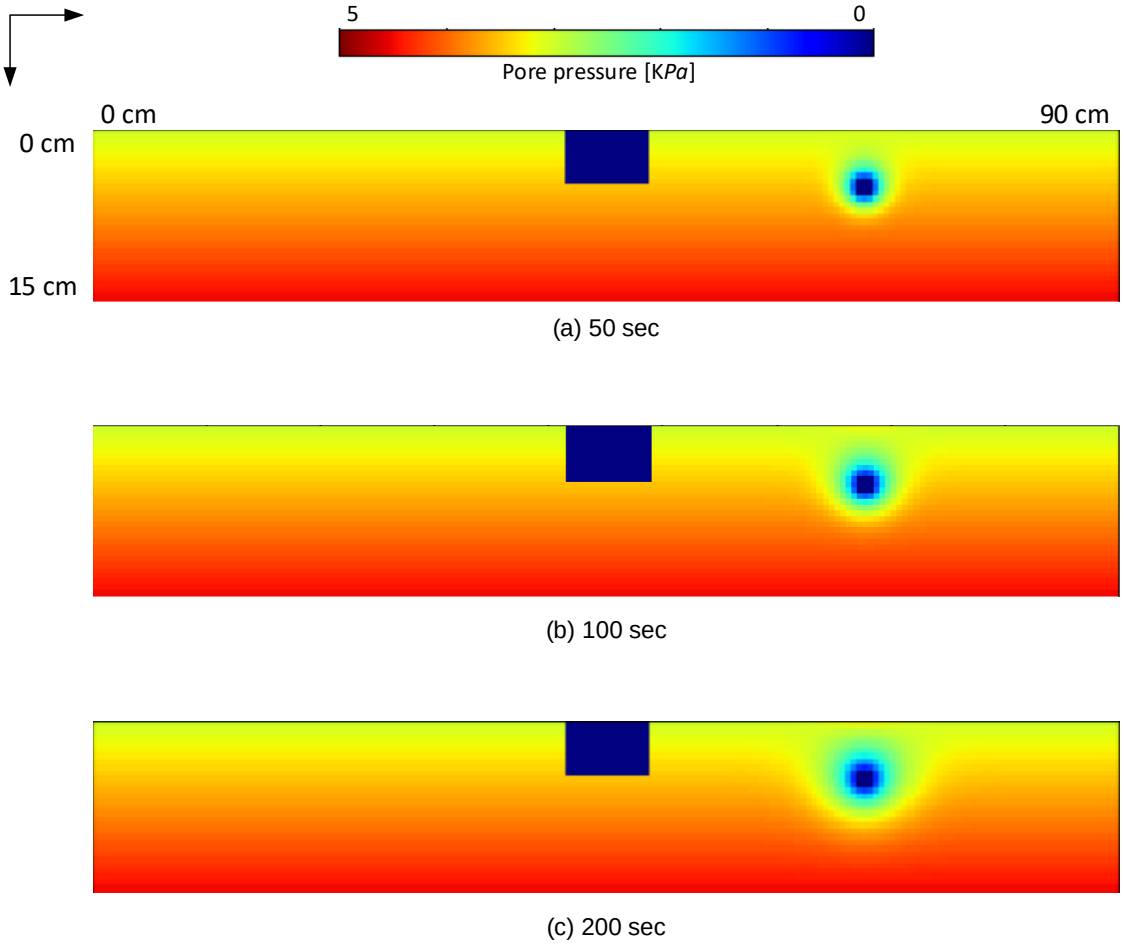

Figure 6.19. Pore pressure contour (case-1)

Furthermore, the comparison between two different case of dewatering size shows that the bigger size of dewatering could cause more faster in erosion in surrounding area. According to this comparison, it might be concluded that the size of the dewatering pipe is also influence on the erosion speed on both surrounding area and the zone nearby the sheet pile or shaft wall as well. The fluid flow field also show that even the seepage flow velocity surrounding the dewatering area was not much different between two different cases, but the area of particle flow flux (circumference of dewatering area) into the dewatering area is larger as shown in **Figure 6.21** and **Figure 6.25**.

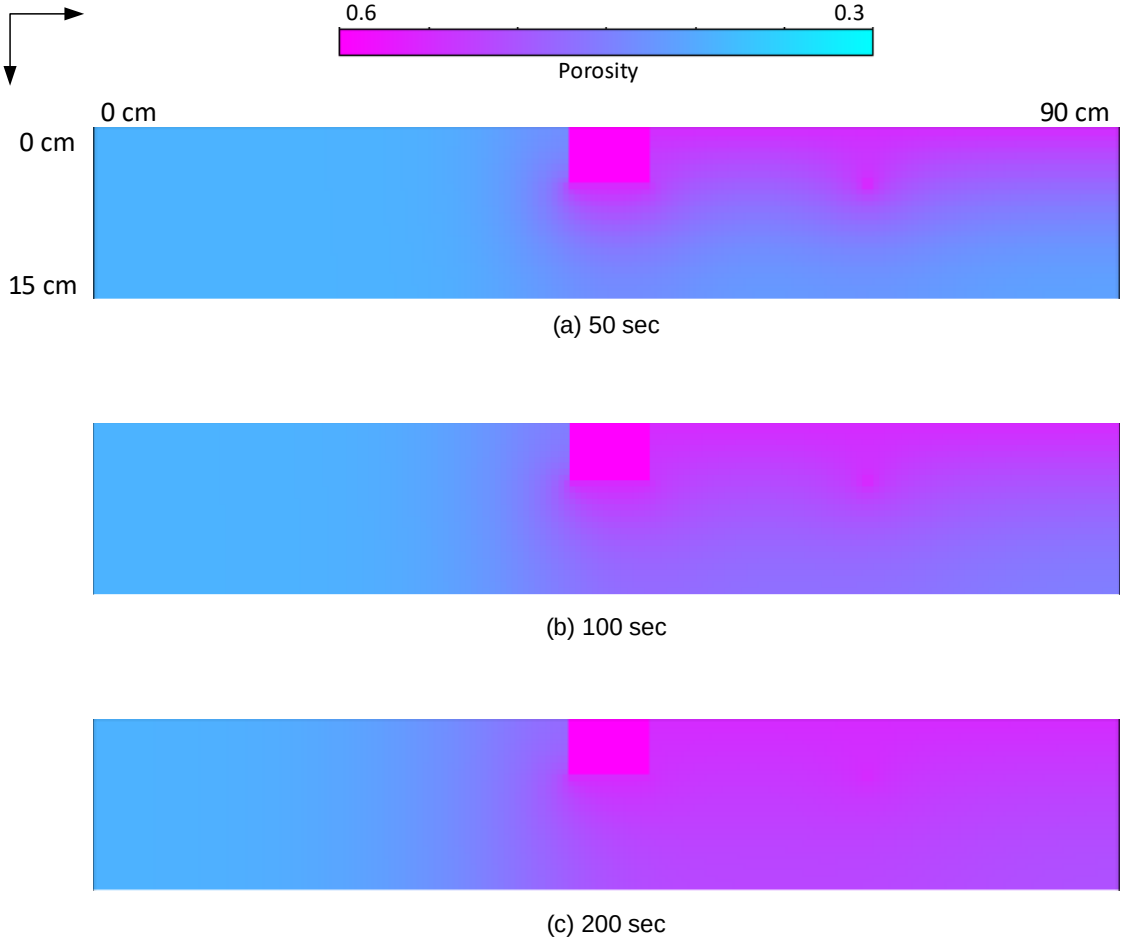

Figure 6.20. Porosity contour (case-1)

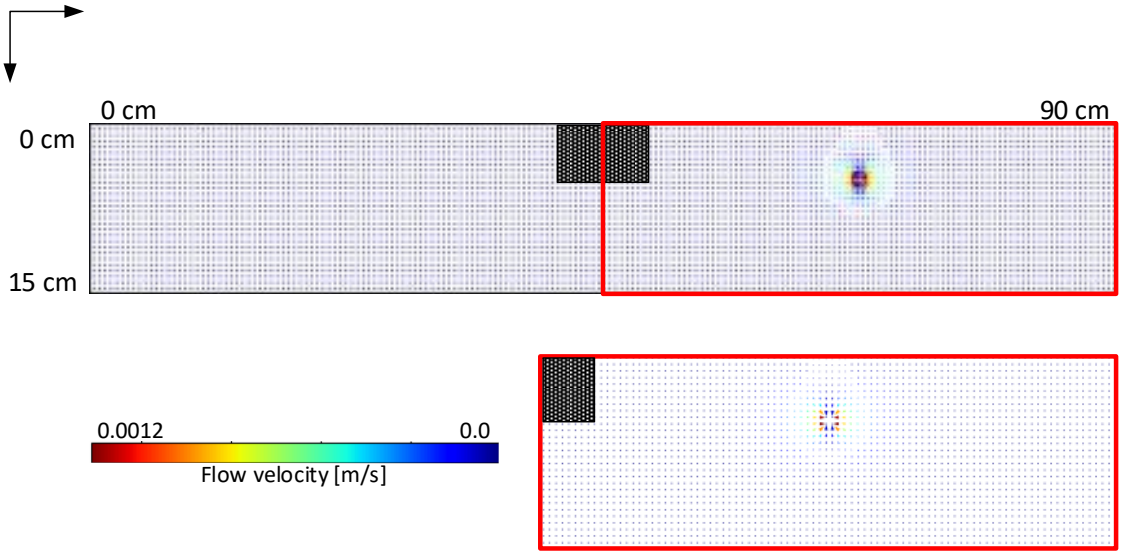

Figure 6.21. Flow vector file (case-1)

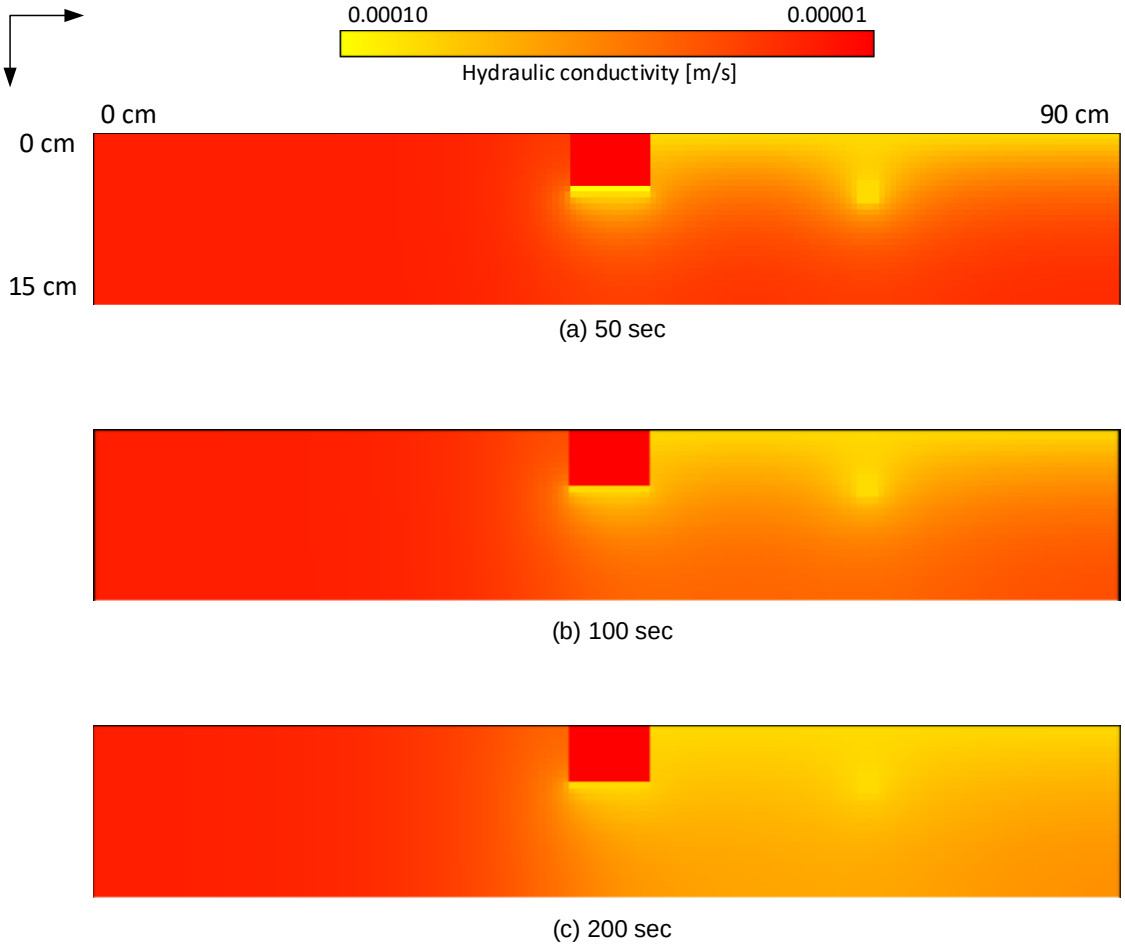

Figure 6.22. Hydraulic conductivity contour (case-2)

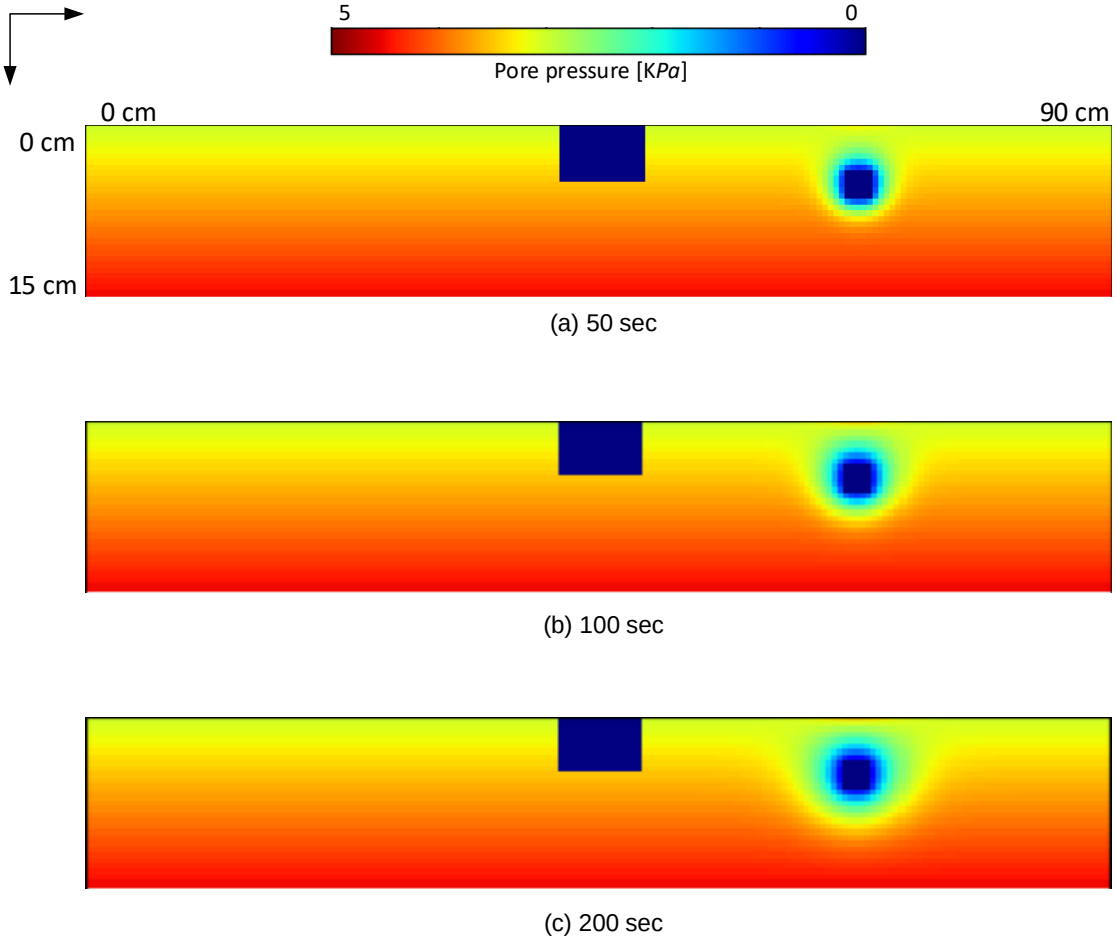

Figure 6.23. Pore pressure contour (case-2)

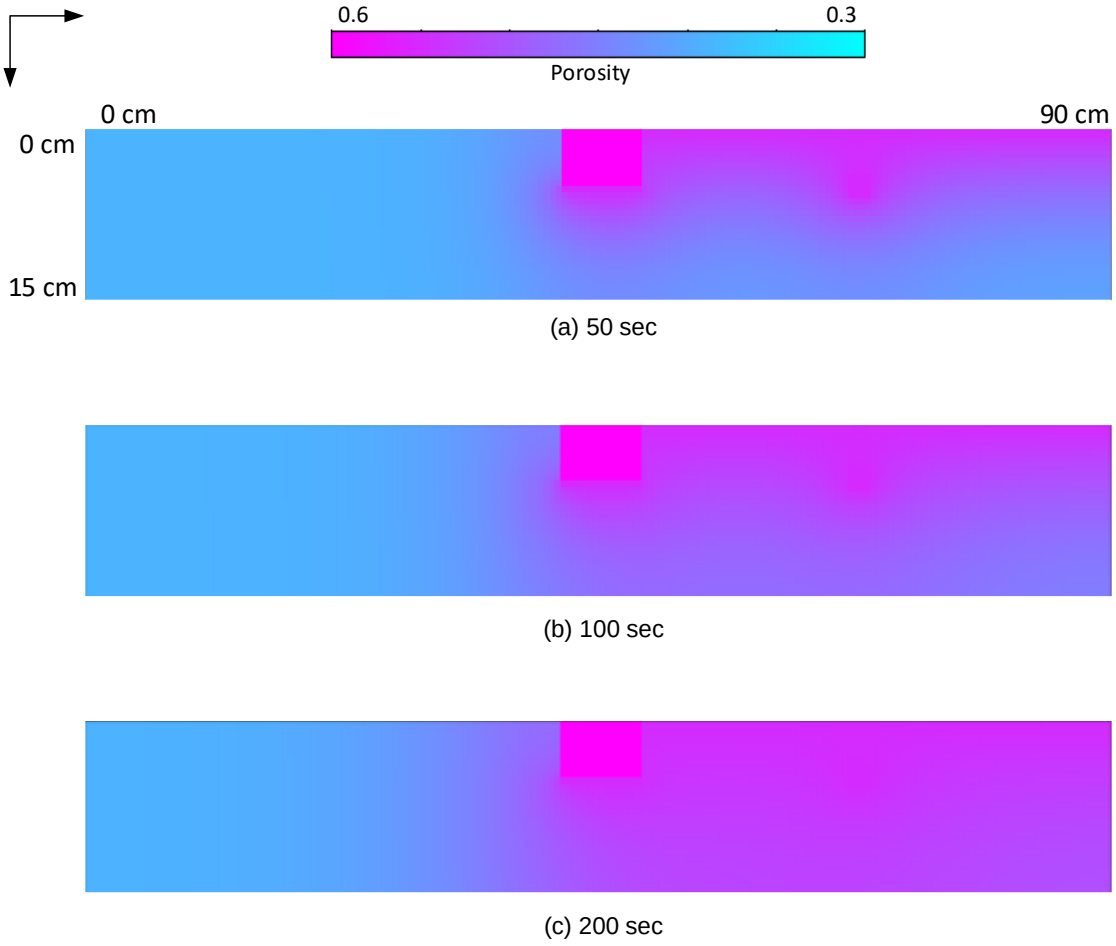

Figure 6.24. Porosity contour (case-2)

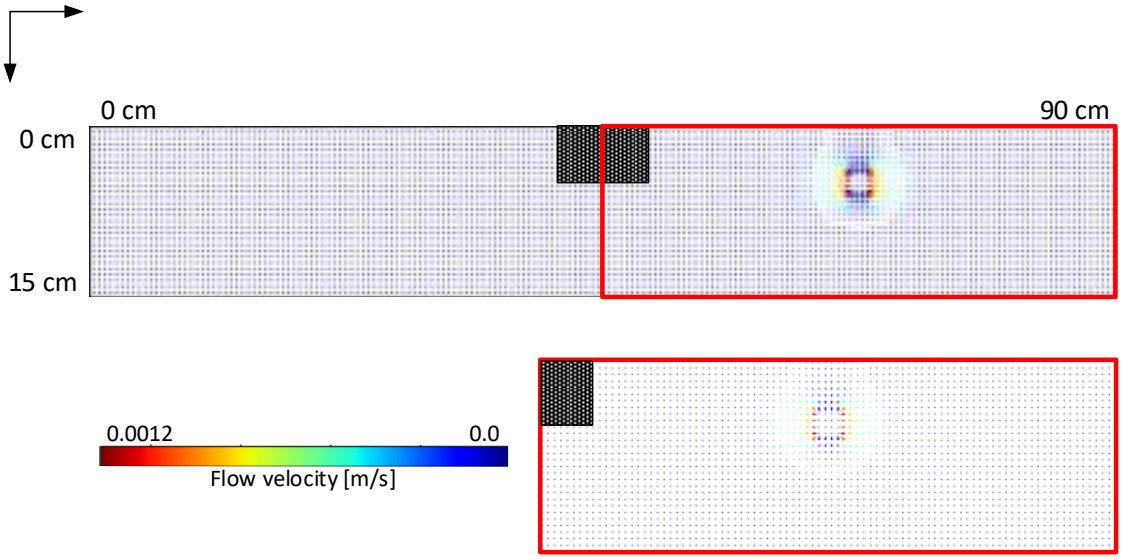

Figure 6.25. Flow vector filed (case-2)

6.4 Conclusion

The first part, the simulation of surrounding soil along the shaft wall was conducted for difference pore pressure at the downstream side. The progression of erosion is relative slow in corresponding with the geological condition, the soil properties which was taken from the previous chapter has a very low hydraulic conductivity. Conversely, the domain size is relatively large which is representing for the real construction site of vertical shaft. Therefore, the gradation of soil in real construction site in necessary to simulate the behavior of internal erosion with the high accuracy of time. However, the simulation could show the erodible zone behind the shaft wall.

The final part of calculation is about the erosion along sheet pile wall which sometime could refer to the vertical shaft as well in experiment scale. The erosion is obviously observed that the erosion is occurring at the bottom of sheet pile and the top of soil layer at the downstream side. However, the erosion in large area at the downstream side is mainly caused by the boundary condition of the top layer of soil in which fully eroded at the boundary. Particle fine loss due to the seepage flow would accumulate over the ground surface at downstream site in the actual filed or experiment. But the limitation of mesh-base method could not generate the additional element during the calculation, therefore, the deeper depth of calculation might be needed for further simulation to reduce the effect of top layer of boundary.

Chapter 7 Conclusions and future studies

The first section of this research tried to perform commercial software (FLAC3D) elucidating both mechanical behavior of surrounding soil along shaft wall and excavation stability of soil undergoing irregular seepage flow due to the dewatering system which is normally used in vertical shaft construction in high groundwater area. The soil-water coupling analysis operated by this commercial software could well describe the mechanical behavior of soil and fluid flow along shaft wall.

The earth pressure acting on the cylindrical shaft wall is one of the results depicted in the fundamental investigation which reflects their unfamiliarity behavior. The earth pressure along this simulation is slightly lesser than the result from analytical solution of active earth pressure proposed by Rankine. Therefore, the further study of earth pressure generation along the cylindrical shaft prove that the reason of unusualness is associated by arching effect.

Moreover, the stability of soil at excavation area is also studied in the term of relative mean effective stress to show the soil stability undergoing seepage flow. In addition, at the excavation area was observed and found an occurrence of heaving soil in which their height will increase while the excavation depth increased. However, the erosion behavior still could not be illustrated by this simulation in accordance with the limitation of commercial software with unavailable calculation scheme of erosion. Therefore, in the following chapter will be an investigation of a new erosion scheme based on suffusion mechanism.

As it mentioned above, the erosion scheme developed here is representing for suffusion mechanism which is basically related to gap-graded soil. According to the suffusion characteristic, this research has paid attention to the fine particle or erodible particle which normally travel through porous media. In addition, the particle transportation governed by advection equation together with the momentum balance equation are used to form the erosion calculation scheme.

In the primary simulation of erosion simulation, the aim of this analysis is about validation the current erosion scheme with available data of experiment conducted by previous research. The experimental data reported by Ke and Takahashi (2014) was selected in which the history of cumulative fine loss had been collected and shown during

suffusion experiment. The simulation of erosion is conducted as following the condition from the experiment as well as the soil properties, especially in soil gradation.

Several concepts of force acting on erodible particle were applied into the simulation to find the most suitable scheme. The consideration of all buoyant force, gravitational force, and drag force was the first try, however, the simulation based on this consideration seems to be generating an excessive force on particle. Subsequently, the simulation based on particle flow in granular media concept in which buoyant force is a function of gravitational force. Nevertheless, the body force or summation between buoyant force and gravitational force still generate an excessive force which induces a rapid erosion. Therefore, the simulation model was finalized by considering only drag force which could show more promising result.

According to the erosion calculation scheme, the tortuosity is considered for the actual length of flow path which could be represented by four different functions of porosity. Therefore, the simulation also shows the different cumulative fine loss due to separate function. The tortuosity which could the similar curve of cumulative fine loss is defined by: $T(\phi) = \phi^{-p}$. In addition, the parametric study of force ratio, β_D, and p-value, p, required in tortuosity function was conducted to show the proper value which are 0.4 and 2, respectively.

Nevertheless, only erosion calculation itself still could not consider the erosion nearby vertical shaft in accordance with lack of fluid flow calculation. Hence, the fluid flow simulation was created simultaneously to consider the fluid flow propagation which is governed by diffusion equation. According to the particle-fluid flow simulation, the half-staggered grid is used to associate the different location of nodal location of each erosion and fluid flow domain. In this section, the simulation still focused on the one-directional flow simulation to show the calculation from particle-fluid flow coupling simulation. At the beginning, the initial condition of fluid flow was differently assigned which will stand for different state of flow condition. According to the one-directional flow simulation, the different initiation of pore pressure is much influence on the erosion behavior. Therefore, the subsequence simulation which will be conducted, the consideration of initiation of pore pressure is should be considered as following either vertical shaft construction condition or experimental condition.

The soil-water coupling simulation has been examined in one-directional flow

simulation already, subsequently, the simulation of erosion nearby shaft wall should be conducted in accordance with the research targets. The erosion along shaft wall problem was simplified to the small area close to the bottom of shaft in which erosion phenomenon is expected to occur. In addition, the simulation of two-directional flow was divided into two sections which are simulation of erosion in real scale and experiment scale.

The simulation representing for real scale construction shows that an erosion starts to occur at the bottom of shaft wall and expands in both horizontal and vertical direction. However, the permeability used in the simulation to represent soil material is relatively low in accordance with the gradation of the soil. In the other hand, it can be said that the ratio between permeability and average length of flow is very low. Therefore, the calculation took more longer time than the experiment scale. In addition, the simulation of flow beneath sheet pile wall in experimental scale also confirm that the erosion is mainly located at the bottom of shaft or sheet pile wall.

Briefly, this research has tried to develop the model to simulate the suffusion together with fluid flow simulation. However, the simulation still does not consider the changes of mechanical behavior of soil due to erosion. Hence, one of the future works in this research could be adding a mechanical calculation scheme for suffusion.

Reference

- Arulanandan K, Krone RB, Loganathan P. Pore and Eroding Fluid Influences on Surface Erosion on Soil. *Journal of the Geotechnical Engineering Division*. 1975;101(1):51-66. doi:10.1061/ajgeb6.0000141
- Barnea E, Mizrahi J. A Generalized Approach to the Fluid Dynamics of Particulate Systems. *The Chemical Engineering Journal*. 1973;5(2):171-189. doi:10.1016/0300-9467(73)80008-5
- Bear J. *Dynamics of Fluids in Porous Media*. Dover; 1988.
- Bendahmane F, Marot D, Alexis A. Experimental Parametric Study of Suffusion and Backward Erosion. *Journal of Geotechnical and Geoenvironmental Engineering*. 2008;134(1):57-67. doi:10.1061/(asce)1090-0241(2008)134:1(57)
- Boiko VM, Pivovarov AA, Poplavski SV. Measurement of gas velocity in a high-gradient flow, based on velocity of tracer particles. *Combustion, Explosion, and Shock Waves*. 2013;49(5):548-554. doi:10.1134/s0010508213050067
- Bonelli S. *Erosion in Geomechanics Applied to Dams and Levees*. Wiley; 2013:2-83.
- Cao C, Shi C, Liu L, et al. Novel Excavation and Construction Method for a Deep Shaft Excavation in Ultrathick Aquifers. *Advances in Civil Engineering*. 2019;2019:1-15. doi:10.1155/2019/1827479
- Chadil M-A, Vincent S, Estivalèzes J-L. Accurate estimate of drag forces using particle-resolved direct numerical simulations. *Acta Mechanica*. 2018;230(2):569-595. doi:10.1007/s00707-018-2305-1
- Chaney R, Demars K, Reddi L, Lee I-M, Bonala M. Comparison of Internal and Surface Erosion Using Flow Pump Tests on a Sand-Kaolinite Mixture. *Geotechnical Testing Journal*. 2000;23(1):116. doi:10.1520/gtj11129j
- Chang DS, Zhang LM. Critical Hydraulic Gradients of Internal Erosion under Complex Stress States. *Journal of Geotechnical and Geoenvironmental Engineering*. 2013;139(9):1454-1467. doi:10.1061/(asce)gt.1943-5606.0000871
- Dellino P, Mele D, Bonasia R, Braia G, La Volpe L, Sulpizio R. The analysis of the influence of pumice shape on its terminal velocity. *Geophysical Research Letters*. 2005;32(21). doi:10.1029/2005gl023954

- Dioguardi F, Mele D, Dellino P. A New One-Equation Model of Fluid Drag for Irregularly Shaped Particles Valid Over a Wide Range of Reynolds Number. *Journal of Geophysical Research: Solid Earth*. 2018;123(1):144-156. doi:10.1002/2017jb014926
- Fanchi JR. *Shared Earth Modeling*. Butterworth-Heinemann; 2002.
- Flemmer RLC, Banks CL. On the drag coefficient of a sphere. *Powder Technology*. 1986;48(3):217-221. doi:10.1016/0032-5910(86)80044-4
- Foster M, Fell R, Spannagle M. The statistics of embankment dam failures and accidents. *Canadian Geotechnical Journal*. 2000;37(5):1000-1024. doi:10.1139/cgj-37-5-1000
- Fujisawa K, Murakami A, Nishimura S, Shuku T. Relation between Seepage Force and Velocity of Sand Particles during Sand Boiling. *Geotechnical Engineering Journal of the SEAGS & AGSSEA*. 2013;44(2):9-17.
- Fujisawa K, Murakami A, Nishimura S-I. Numerical Analysis of the Erosion and the Transport of Fine Particles within Soils Leading to the Piping Phenomenon. *Soils and Foundations*. 2010;50(4):471-482. doi:10.3208/sandf.50.471
- Gabora M, Brown P, Ohlin H, Carpenter K, French G. Dewatering of a Deep Shaft in a Complex Hydrogeologic Setting. In: *10th International Conference on Acid Rock Drainage & IMWA Annual Conference*. ; 2015.
- Gabriella M. *Internal Erosion in the Pervious Foundation of an Embankment Dam: A Case Study of the Lossen Dam*. ; 2016:3-5.
- Guillard F, Forterre Y, Pouliquen O. Scaling laws for segregation forces in den sheared granular flows. *Journal Fluid Mechanics*. 2016;807(R1):1-11.
- Haider A, Levenspiel O. Drag coefficient and terminal velocity of spherical and nonspherical particles. *Powder Technology*. 1989;58(1):63-70. doi:10.1016/0032-5910(89)80008-7
- Horikoshi K, Ke L, Takahashi A. Suffusion-induced change in spatial distribution of fine fraction in embankment subjected to steady and unsteady seepage flow. *Japanese Geotechnical Society Special Publication*. 2016;2(49):1708-1713. doi:10.3208/jgssp.jpn-073

- Indraratna B, Muttuvel T, Khabbaz H. Modelling the erosion rate of chemically stabilized soil incorporating tensile force – deformation characteristics. *Canadian Geotechnical Journal*. 2009;46(1):57-68. doi:10.1139/t08-103
- Itasca Consulting Group, Inc. (2019) FLAC3D. *Fast Lagrangian Analysis of Continua in Three-Dimensions, Ver. 7.0*. Minneapolis: Itasca.; 2019.
- Ke L, Takahashi A. Experimental investigations on suffusion characteristics and its mechanical consequences on saturated cohesionless soil. *Soils and Foundations*. 2014;54(4):713-730. doi:10.1016/j.sandf.2014.06.024
- Khilar KC, Fogler HS, Gray DH. Model for Piping-Plugging in Earthen Structures. *Journal of Geotechnical Engineering*. 1985;111(7):833-846. doi:10.1061/(asce)0733-9410(1985)111:7(833)
- Koenders MA, Williams AF. Flow equations of particle fluid mixtures. *Acta Mechanica*. 1992;92(1-4):91-116. doi:10.1007/bf01174169
- Kumar A, Khakhar DV, Tripathi A. Theoretical calculation of the buoyancy force on a particle in flowing granular mixtures. *Physical Review E*. 2019;100(4). doi:10.1103/physreve.100.042909
- Lane EW. Security from Under-Seepage-Masonry Dams on Earth Foundations. *Transactions of the American Society of Civil Engineers*. 1935;100(1):1235-1272. doi:10.1061/taceat.0004655
- Liang Y, Yeh T-CJ, Chen Q, Xu W, Dang X, Hao Y. Particle erosion in suffusion under isotropic and anisotropic stress states. *Soils and Foundations*. 2019;59(5):1371-1384. doi:10.1016/j.sandf.2019.06.009
- Liang Y, Yeh T-CJ, Wang Y-L, Liu M, Wang J, Hao Y. Numerical simulation of backward erosion piping in heterogeneous fields. *Water Resources Research*. 2017;53(4):3246-3261. doi:10.1002/2017wr020425
- Matyka M, Khalili A, Koza Z. Tortuosity-porosity relation in porous media flow. *Physical Review E*. 2008;78(2). doi:10.1103/physreve.78.026306
- Muramatsu M, Abe Y. Considerations in shaft excavation and peripheral ground deformation. *Geotechnical Aspects of Underground Construction in Soft Ground*. Published online 1996:173-178.

- Perry RH, Cecil Hamilton Chilton, John Howard Perry. *Chemical Engineers' Handbook. 5th Ed. Prepared by a Staff of Specialists, under the Editorial Direction of Robert H. Perry [And] Cecil H. Chilton.* New York Mcgraw-Hill; 1973.
- Richards KS, Reddy KR. Critical appraisal of piping phenomena in earth dams. *Bulletin of Engineering Geology and the Environment*. 2007;66(4):381-402. doi:10.1007/s10064-007-0095-0
- Robbins BA, Griffiths DV. Internal Erosion of Embankments: A Review and Appraisal. In: *Rocky Mountain Geo-Conference*. ASCE; 2018.
- Rusche H, Issa R. The Effect of Voidage on the Drag Force on Particles in Dispersed Two-Phase Flow. Published online 2000.
- Russell EM. Particle Transport in Flow through Porous media: Advection, Longitudinal dispersion, and Filtration. Published online 1992.
- Snorri Gudmundsson. *General Aviation Aircraft Design*. Elsevier - Health Sciences Division; 2014.
- Telkar SG, Pote NS. Soil Erosion: Types and Their Mechanism. *Biomolecule Reports- An International eNewsletter*. 2018;(ISSN:2456-8759).
- Tomlinson SS, Vaid YP. Seepage forces and confining pressure effects on piping erosion. *Canadian Geotechnical Journal*. 2000;37(1):1-13. doi:10.1139/t99-116
- Turton R, Levenspiel O. A short note on the drag correlation for spheres. *Powder Technology*. 1986;47(1):83-86. doi:10.1016/0032-5910(86)80012-2
- Van Beek VM, De Bruijin HTJ, Knoeff JG, Bezuijen A, Forster U. Levee Failure Due to piping: a full-scale Experiment. In: *Proceedings 5th International Conference on Scour and Erosion (ICSE-5)*. ; 2010.
- van der Vaart K, van Schrojenstein Lantman MP, Weinhart T, Luding S, Ancey C, Thornton AR. Segregation of large particles in dense granular flows suggests a granular Saffman effect. *Physical Review Fluids*. 2018;3(7). doi:10.1103/physrevfluids.3.074303
- Vardoulakis I, Stavropoulou M, Papanastasiou P. Hydro-mechanical aspects of the sand production problem. *Transport in Porous Media*. 1996;22(2):225-244. doi:10.1007/bf01143517

- Wadell H. The coefficient of resistance as a function of Reynolds number for solids of various shapes. *Journal of the Franklin Institute*. 1934;217(4):459-490. doi:10.1016/s0016-0032(34)90508-1
- Wan CF, Fell R. Investigation of Rate of Erosion of Soils in Embankment Dams. *Journal of Geotechnical and Geoenvironmental Engineering*. 2004;130(4):373-380. doi:10.1061/(asce)1090-0241(2004)130:4(373)
- Yang J, Yin Z-Y, Laouafa F, Hicher P-Y. Hydromechanical Modeling of Granular Soils considering Internal Erosion. *Canadian Geotechnical Journal*. 2020;57(2):157-172. doi:10.1139/cgj-2018-0653